UNIVERSITÀ DEGLI STUDI DI MILANO

Scuola di Dottorato in Scienze Biologiche e Molecolari

XXVII Ciclo

RNA DEPENDENT RNA POLYMERASE: A VALUABLE TARGET TO BLOCK VIRAL REPLICATION IN SINGLE-STRANDED (+)SENSE RNA VIRUSES.

Romina Croci

PhD Thesis

Scientific tutor: PROF. MARTINO BOLOGNESI

Scientific cotutor: Dr. ELOISE MASTRANGELO

Academic year: 2013-2014

SSD: BIO/10

Thesis performed at Department of Bioscience at University of Milan

Index

PART I

Abstract

The (+)strand RNA viruses include a very large group of viruses that cause epidemic diseases in humans, including dengue fever and gastroenteritis. The human (+)RNA viruses include Flaviviruses (FV) and Norovirus (NV). Both encode for proteins essential for viral replication, such as the RNA dependent RNA polymerase (RdRp). Since human cells lack RdRp, it appears as one of the most promising targets for antivirals development. I worked on the identification of new non-nucleotide inhibitors against FV and NV, using RdRp as the main target. In this context, suramin and NF023 have been identified in my lab as NV RdRp inhibitors that, however both are hampered in their application by pharmacokinetics problems. To overcome such problems, I analyzed the potential inhibitory role of Naf2, a fragment derived from these two molecules. Although Naf2 showed a low inhibitory activity, the crystal structures of NV RdRp/Naf2 complex revealed a new binding site. To further map this new site, I tested a Naf2 related molecule, PPNDS. The crystal structures of the RdRp/PPNDS complex revealed interesting features about the new binding site. I also focused on structurally related molecules synthesized following structure-driven information. NV RdRp crystal structures in complex with one of these compounds (Cpd6) were analyzed, providing new knowledge on the interactions between a small fragment and NV RdRps, establishing a platform for structure-guided drug optimization. In parallel to the NV work, I screened *in silico* a library of compounds against FV RdRp. One of the best compounds identified (HeE1-2Tyr) was able to inhibit the RdRp activity and several FVs in cell-based assays. Although the crystallographic analyses don't reveal clear enough electron density for the inhibitor, indirect evidence suggests that HeE1-2Tyr interferes with the RdRp priming loop that appears disordered.

1. State of the Art

1.1 General introduction about viruses

Viruses are subcellular infectious agents that are obligate intracellular parasites. They infect and take over a host cell in order to replicate.

The mature extracellular virus particle is called virion. The virion contains a DNA or RNA genome wrapped in a protein coat called capsid or nucleocapsid. Some viruses display a lipid envelope surrounding the nucleocapsid. The capsid and the envelope play many roles, including virus attachment to cells, entry into cells, release of the capsid contents into the cells, and packaging of newly formed viral particles. The capsid and envelope are also responsible for transfer of the viral genetic material from one cell to another.

Three broad classes of viruses can be recognized which may have independent evolutionary origins (Table 1):

1) the first class hosts a genome based on DNA, either single stranded or double stranded, and the genome is replicated by direct DNA→DNA copying. During infection, the viral DNA is transcribed by cellular and/or viral RNA polymerases to produce mRNAs for translation into viral proteins. Replication of the genomes of most eukaryotic DNA viruses and assembly of progeny viruses occur in the nucleus;

2) the second class of viruses contains an RNA genome, and the RNA is replicated by direct RNA→RNA copying. Some RNA viruses host a genome that is already the messenger RNA; these are defined as plus-stranded RNA viruses. Other RNA viruses have a genome that is anti-messenger sense, defined as minus strand RNA viruses. In the case of the

minus-strand RNA viruses and double-strand RNA viruses, the RNA synthesizing enzymes also synthesize mRNA, and are packaged in the virion, because their genomes cannot function as mRNA. Replication of the genome proceeds through RNA intermediates that are complementary to the genome in a process that follows the same rules as DNA replication;

3) the third class of viruses encodes the enzyme reverse transcriptase, and these viruses have an RNA→ DNA retro-transcription step in their life cycle. The genetic information encoded by these viruses thus alternates between being encoded in RNA and in DNA.

With the exception of the retroviruses, which are diploid (they contain two identical copies of the single-stranded genomic RNA), all the viruses are haploid (they contain only one copy of the genomic nucleic acid).

Viruses are classified into species on the basis of a close relationship. Virus species that exhibit close relationship are then grouped into a genus. Species within a genus usually share significant nucleotide sequence identity. Genera are grouped into families, which can be considered the fundamental unit of virus taxonomy. Classification into families is based on the type and size of the nucleic acid genome, the structure of the virion and the strategy of replication used by the virus.

	Nucleic acid	**Genome size (kbp)**	**Segments**	**Family**
CLASS 1	DS DNA	130-375	1	Poxviridae
		170-190	1	Asfariviridae
		170-400	1	Iridoviridae
		120-220	1	Herpesviridae
		90-230	1	Baculoviridae
		36-48	1	Adenoviridae
		5	1	Polyomaviridae
		6.8-8.4	1	Papillomaviridae
		Varia	1	Several families
	SS DNA	6-8	1	Parvoviridae
		Varia	1	Several families
CLASS 2	DS RNA	20-30	10-12	Reoviridae
		5.9	2	Birnaviridae
		4.6-7.0	1 o 2	Three families
	SS (+) RNA	28-33	1	Coronaviridae
		13-16	1	Arteriviridae
		10-13	1	Togaviridae
		10-12	1	**Flaviviridae**
		7-8.5	1	Picornaviridae
		7-8	1	Astroviridae
		8	1	**Caliciviridae**
		Varia	1	Many families
	SS (-) RNA	15-16	1	Paramyxoviridae
		13	1	Filoviridae
		13-16	1	Rhabdoviridae
		9	1	Bornaviridae
		13	8	Orthomyxoviridae
		12-23	3	Bunyaviridae
		11	2	Arenaviridae
CLASS 3	SS RNA RT	7-10	dimer	Retroviridae
	DS RNA RT	3	1	Hepadnaviridae
		8	1	Caulimoviridae

Table 1. Classification of the viruses based on the nucleic acid. The size, the structure of the virion and the main families are indicated.

1.2 The *Caliciviridae* Family

The Caliciviruses are non-enveloped viruses with icosahedral symmetry and diameter of about 30 nm. Caliciviruses are currently classified into 5 genera: Vesivirus, Lagovirus, Nebovirus, Sapovirus and Norovirus, two of which, the Norovirus and the Sapovirus, contain agents that cause human gastroenteritis. The Norovirus genus is subdivided into at least 5 genogroups (GI-GV). Genogroups GI, GII and GIV infect humans and cause acute gastroenteritis. Futhermore, Noroviruses have been isolated from numerous other species including pigs (GII), cattle and sheeps (GIII) and mice (GV) (Figure 1).

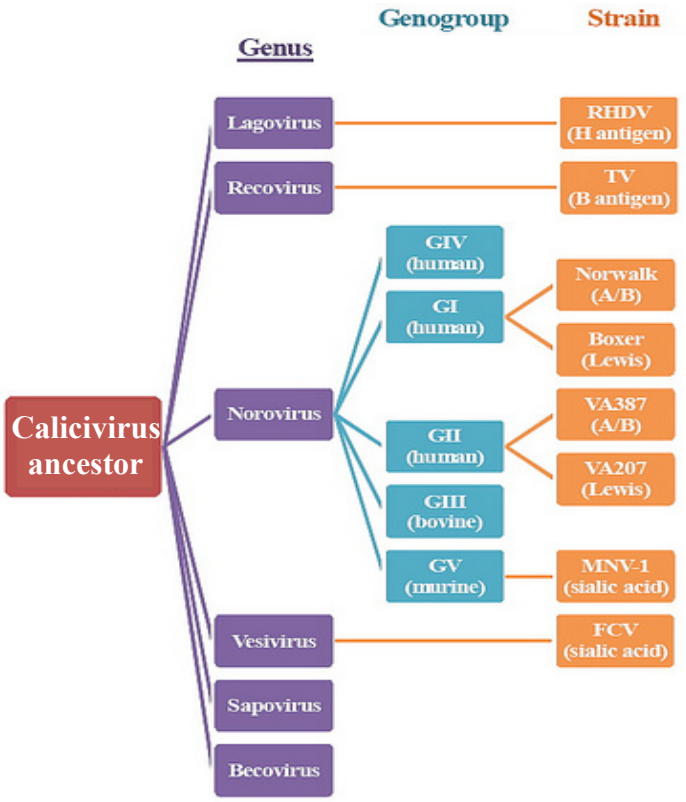

Fig 1. Subdivision of the Calicivirus family.

The human Caliciviruses have been difficult to study so far; as a consequence, our knowledge is still limited. What we know of the molecular biology of Caliciviruses comes from studies of the non-human viruses. The murine Norovirus (mNV) is closely related genetically to the human Norovirus (hNV), thus providing an excellent model that will accelerate research on the mechanisms by which the Norovirus genome is expressed, and on the functions of the encoded proteins.

The Norovirus genome is a compact single stranded positive sense RNA molecule of about 7.7 kb. The 5' end of the genomic RNA is covalently attached to a virus encoded protein known as VPg, while the 3' end is polyadenylated.

The Norovirus genome is organised into three conserved open reading frames (ORFs, Figure 2a), with the exception of mNV, which has a fourth alternative ORF (Figure 2b). The fourth ORF is unique to the mNV cluster in GV, and has not yet been identified in any other Norovirus. The only member of the *Caliciviridae* family known to have an equivalent fourth ORF is human Sapovirus [1]; [2].

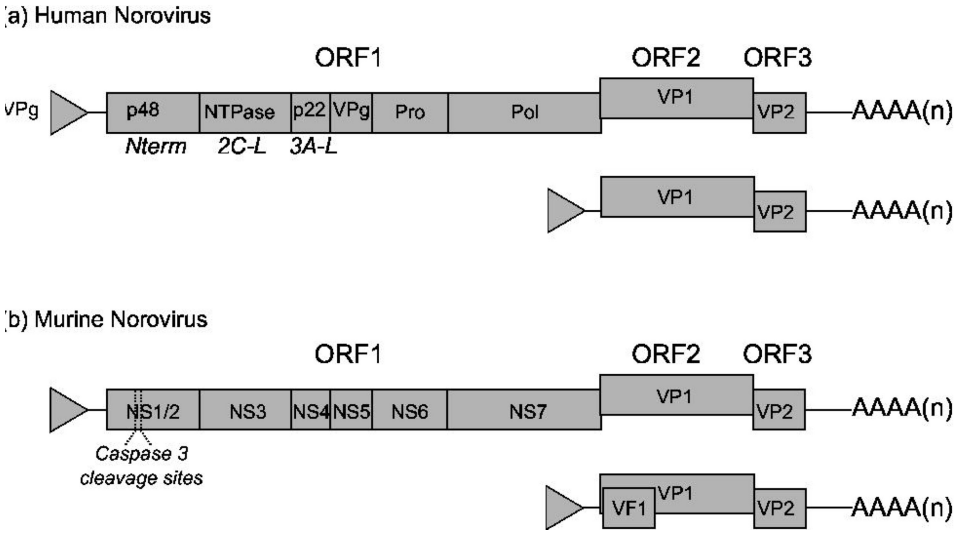

Fig 2. Organization of the hNV and mNV genomes. (a) The hNV genome is covalently attached to VPg (NS5) with a poly(A) tail, and is divided into three ORFs, common to all Noroviruses. ORF1 is translated as a polyprotein, which is cleaved by the viral protease NS6 to produce the NS proteins. ORF2 and ORF3 are translated from a subgenomic RNA. (b) mNV shares a similar genome organization, but has an additional alternative fourth ORF. ORF4 overlaps with ORF2 and is also translated primarily from the subgenomic RNA into the virulence factor 1 (VF1) protein.

For all Noroviruses, ORF1 is translated as a large polyprotein, which is co- and post-translationally cleaved by the virus-encoded protease (mNV NS6/ hNV Pro) to release at least six mature non-structural (NS) proteins including NS6/Pro [3]. The other NS proteins include the viral RNA dependent RNA polymerase (mNV NS7/hNV Pol), mNV NS5/hNV VPg, the mNV NS3/hNV NTPase, mNV NS1/2/hNV p48, and NS4/hNV p22, which have both been implicated in formation of the replication complex [4]; [5].

ORF2 and ORF3 are translated from a subgenomic RNA and encode the major and minor capsid proteins, VP1 and VP2 respectively. ORF4 of

mNV is translated from an alternative reading frame within ORF2 and encodes the recently identified protein virulence factor 1 (VF1), a mitochondrially localised novel innate immune regulator [2].

The nomenclature for the Norovirus proteins is summarised in Table 2.

Protein name		
mNV	**hNV**	**Functions**
NS1/2	p48	It may has a role in replication complex formation; contributes to persistence in mNV infections.
NS3	NTPase	RNA helicase; NTPase.
NS4	p22	It may has a role in replication complex formation.
NS5	VPg	Genome linked protein involved in translation and replication.
NS6	Pro	Protease
NS7	Pol	RNA dependent RNA polymerase
VP1	VP1	Major capsid protein
VP2	VP2	Minor capsid protein
VF1	-	Virulence factor

Table 2. Nomenclature for the hNV and mNV proteins and their functions.

Interaction of Noroviruses with the cell surface is known to involve carbohydrate structures, which in the case of hNV include the histo blood group antigens (HBGAs). Receptor binding and/or entry processes appear to be the limiting factors for hNV culture in immortalised cells, as viral RNA transfected into cells is able to undergo limited replication.

Once a Norovirus VPg-linked RNA genome is released into the cytoplasm of a cell, it behaves as an mRNA template for the 'pioneer round' of viral RNA translation (Figure 3). For this to occur, the viral RNA is recognised by cellular translation initiation factors and is translated into protein by the cellular translational apparatus [6]. Translation of all Calicivirus genomes occurs by a novel mechanism involving VPg that is not

found in many other animal RNA viruses [7]. VPg covalently attached to the 5' end of the genome mediates translation of viral RNA, acting as a cap-substitute and recruits host cell translation initiation factors. The extremities of Calicivirus genomes contain evolutionarily conserved RNA structures that are known to interact with host cell factors to promote viral replication and translation [8]; [9]. As many of the host factors form direct protein-protein interactions with each other, it is possible that numerous cellular RNA-binding proteins contribute to the circularisation of the viral genome during translation and/or replication. It is possible that these types of RNA-protein interactions play both positive and negative regulatory roles in the life cycle of Noroviruses. Translation of the ORF1 polyprotein is followed by co- and post-translational processing by the viral NS6 protease, and results in the release of the viral non-structural proteins ready for replication complex formation, and of their precursors, some of which are thought to be functionally active in replication [10]. Similarly to other positive strand RNA viruses, Norovirus replication occurs in close association with host-derived membrane complexes in the cytoplasm [11]; [12]. The NS proteins, as well as the major and minor capsid proteins, co-localise with NS7 and dsRNA at this location, forming the replication complex [4]; [13]. Genome replication occurs via a negative sense RNA intermediate, and is carried over by the viral RdRp. The Norovirus RdRps, generally referred to as NS7, contain active site residues conserved among other positive strand RNA virus RdRps, and are structurally and functionally conserved [14]. The replicative properties of the mNV RdRp (NS7) are comparable *in vitro* to those of the hNV RdRp, supporting the use of mNV for replication studies [15]. The process of initiation of negative sense RNA synthesis on the incoming parental viral RNA is not fully understood but the Norovirus RdRp

has two mechanisms of initiation that have been demonstrated both *in vitro* and in cells: *de novo,* and VPg-dependent [16]. Following the generation of a double-stranded RNA, the synthesis of positive sense genomic and subgenomic RNA occurs.

The processes behind viral assembly, encapsidation and the exit of noroviruses are largely unknown. The ability of VP1 to self-assemble into virus-like particle (VLPs) morphologically and antigenically indistinguishable from native virions suggests that it may be sufficient to drive capsid assembly during virus replication [17], although the involvement of cellular proteins cannot be excluded.

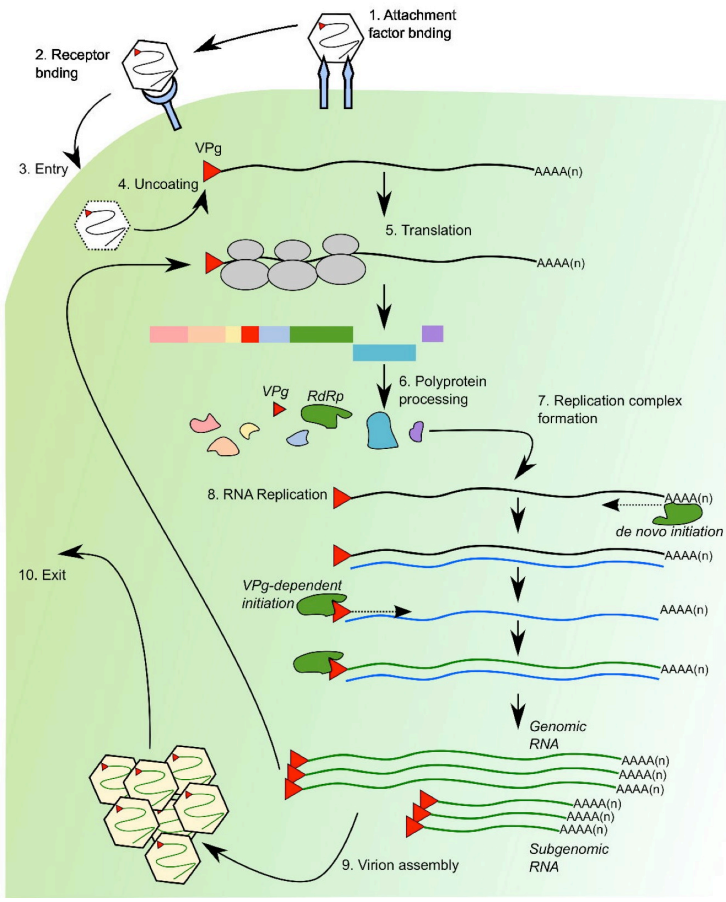

Fig 3. Outline of the Norovirus lifecycle. hNV and mNV are thought to attach to the cell surface (1) using various carbohydrate attachment factors. This is not sufficient to mediate entry, therefore binding to an unidentified protein receptor is thought to be required (2). Entry (3) and uncoating (4) proceed through yet undefined pathways. The incoming viral genome is translated (5), through interactions with VPg at the 5' end of the genome (red traingle) and the cellular translation machinery. The ORF1 polyprotein is co- and post-translationally cleaved (6) by the viral protease NS6. The replication complex (7) is formed by recruitment of cellular membranes to the perinuclear region of the cell (not shown), through interactions in part with NS1/2 and NS4. Genome replication (8) occurs via a negative strand intermediate, and genomic and subgenomic RNA are generated by the viral RdRp/NS7, using both *de novo* and VPg-dependent mechanisms of RNA synthesis. The replicated genomes are translated (within the replication complex) or packaged into the capsid, VP1, for virion assembly (9), which move through the exit (10).

1.3 Norovirus RdRp

The overall structure of NV RdRp can be described using an analogy to a right hand, as commonly referred to for a wide range of nucleic acid polymerases (Figure 4). The active site consists of $G^{342}D^{343}D^{344}$ residues belonging to the palm subdomain. The incoming NTP enters between finger and palm domains (close to the active site) and the dsRNA exits channel is near the palm and thumb domains.

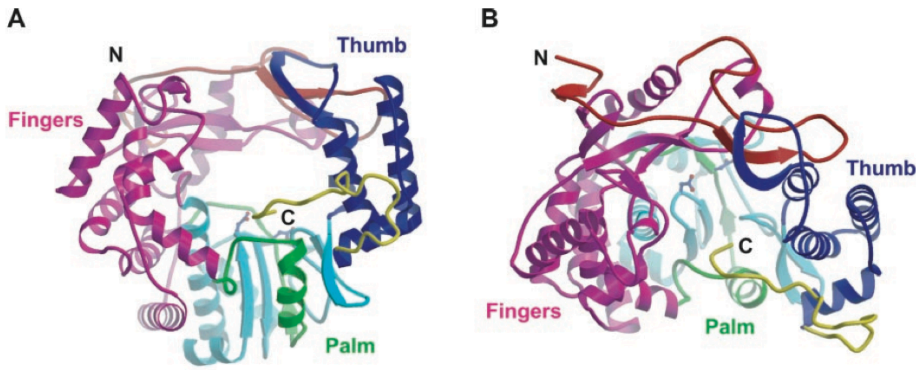

Fig 4. NV RdRp overall structure. Ribbon diagram showing front (A) and top (B) views of NV RdRp. The amino-terminal region is red, fingers subdomain magenta, palm subdomain green and cyan, thumb subdomain blue, and C-terminal region yellow. The N- and C-termini are marked.

In addition to the fingers, palm, and thumb subdomains common to all polymerases, NV RdRp has an additional N-terminal domain bridging the fingers and thumb subdomains, common to all Caliciviruses RdRps of known three-dimensional structure [18].

A particular feature is a region of hydrophobic residues built by Trp29, Pro421, Met430, and Ile431, fairly well conserved in Noroviruses, but poorly conserved in other Caliciviruses. Although the functional importance of the resulting NV RdRp dimers is not clear, the location of this hydrophobic patch near the top of the active site cleft suggests that protein-

protein interactions important for RNA binding or RNA synthesis may be mediated by this contact surface.

A particularly striking feature of the NV RdRp structures is the location of the C-terminal segment in the active site cleft near the two catalytic Asp residues (Asp343 and Asp 344). This segment interacts mainly with the wall of the active site cleft formed by the thumb domain, is well exposed to solvent, and likely is characterized by conformational flexibility (Figure 5).

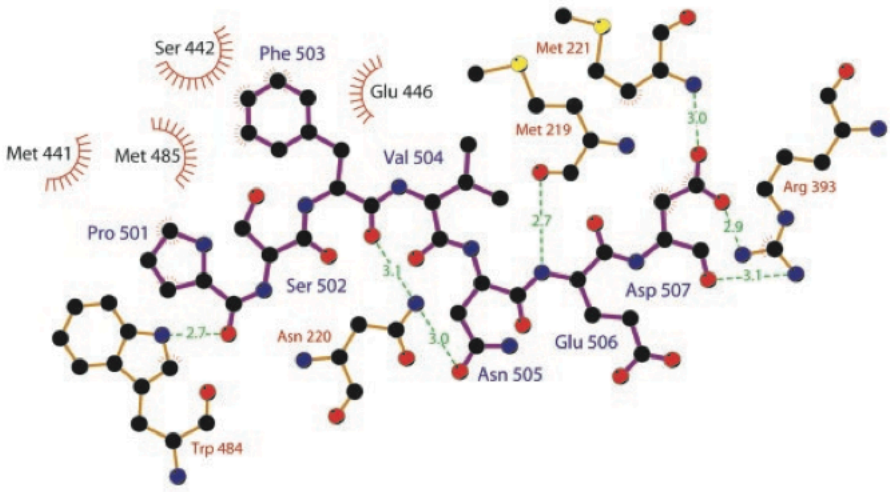

Fig 5. Carboxy-terminal segment of NV RdRp. LIGPLOT diagram of hydrogen bonding (dashed green lines) and van der Waals interactions between residues 501–507 and other residues in the polymerase.

The structural similarities shared among NV, HCV, and bacteriophage φ6 RdRps suggest that the C-terminal segment in NV RdRp may also play a role in initiating RNA replication.

The location of the C-terminal sequence in the NV RdRp active site appears to block the entry of an RNA primer-template duplex. The presence

of the C-terminal segment primarily interferes with the entry of the primer strand of an RNA duplex into the active site cleft, but it is well positioned to interact with short di- or tri-nucleotide primers, or possibly with hairpin structures forming near the active site.

An alignment of the C-terminal sequences from Norovirus RdRp reveals a high degree of sequence conservation in this region, indicating that a similar structure is found in both genogroups of Noroviruses. A lower degree of sequence similarity in this region of RdRps from other Calicivirus genera, as well as the lack of structural similarity between the last 25 residues of the NV and RHDV RdRps, suggests that the structure of the C-terminus differs in polymerases from these viruses. mNV and hNV RdRp sequence alignment showed a residue identity of 59.0 %. In a comparative analysis of 3D structural similarities between RdRps of different members of the *Caliciviridae* family, the apo structures of mNV and hNV RdRp proteins [14]; [19] were found to be well superimposed in the N- terminal extension and the fingers domain. Significant structural variation was instead found in the thumb and palm subdomains containing the C-terminal and the loop regions (residues 302–307, 374–381 and 471–480) (Figure 6). The loop I is close to the active site, the loop II is adiacent to the predicted rNTP-binding site [19] and loop III is near to the dimer interface and the helix backbone.

Structural comparison between mNV RdRp– and hNV RdRp–RNA complexes [20]; [21] revealed significant differences in the RNA-binding loop (residues 433–440), which suggests that RNA binding likely causes conformational changes in the mNV RdRp active site.

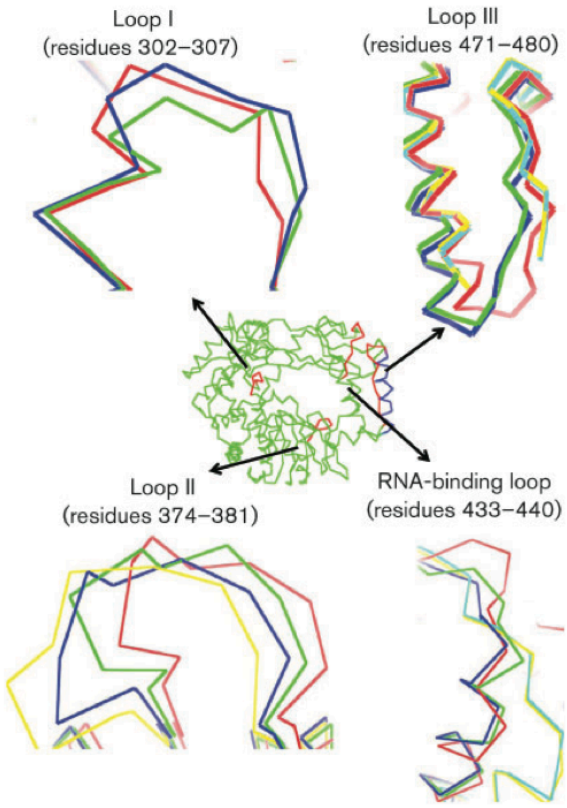

Fig 6. Variation between mNV and hNV RdRp structures. Variation in the loop regions corresponding to loops I (residues 302–307), II (374–381) and III (471–480) and the RNA-binding loop (residue 433–440) are marked on the overall structure model in the centre, and close-ups are shown. mNV RdRp is shown in red, while hNV RdRp is shown in blue (2B43; strain Hu/NLV/Dresden174/1997/GE), green (1SH0; apo protein), yellow (3BSO; hNV RdRp in complex with dsRNA) and cyan (3H5X; hNV RdRp in complex with dsRNA) [22].

RdRps, like other polynucleotide polymerases, follow a five-step reaction cycle involving (i) the binding of an NTP complementary to the base of the template to form an initial "open" complex, followed by (ii) a conformational change to the "closed" complex, (iii) nucleotidyl transfer and translocation, (iv) a second conformational change, and finally (v) the

release of pyrophosphate (Figure 7).

To provide a more detailed structural basis for understanding the nucleotidyl transfer reaction in viral RdRps, the crystal structures of hNV RdRp in complex with oligonucleotide (5'-UGCCCGGG-3'), two Mn^{2+} ions, and either the natural substrate CTP or the nucleotide inhibitor NCT have been determined [20].

These structures reveal for the first time details of ternary RdRp+RNA+NTP complexes trapped immediately prior to the nucleotidyl transfer reaction (the closed *complex iii* in Figure 7).

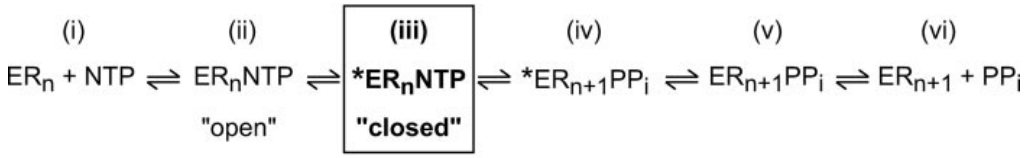

Fig 7. General kinetic scheme for nucleotide incorporation in RdRps and other polymerases. *E*, RdRp enzyme; *Rn*, RNA oligonucleotide containing *n* nucleotides; *Rn+1*, RNA oligonucleotide containing *n* + 1 nucleotides; *NTP*, nucleoside triphosphate; *PPi* pyrophosphate.

1.4 The *Flaviviridae* Family

The family *Flaviviridae* belongs to the second class of viruses and consists of three genera: Pestivirus (*i.e.* bovine viral diarreha virus, BVDV), Hepacivirus (hepatitis C virus, HCV) and Flavivirus (i.e. Dengue virus, West Nile virus, Yellow Fever virus).

Flaviviruses are enveloped viruses [23] with single-stranded positive-sense RNA genome of about 11 kb. Phylogenetic studies revealed that a common ancestor originated the presently known viruses, which schematically belong to three major evolutionary branches: tick-borne Flaviviruses (TBFVs), mosquito-borne Flaviviruses (MBFVs) and

Flaviviruses with no known vector (NKFVs, which are believed to be non-vectorised viruses infecting bats and rodents) (Figure 8).

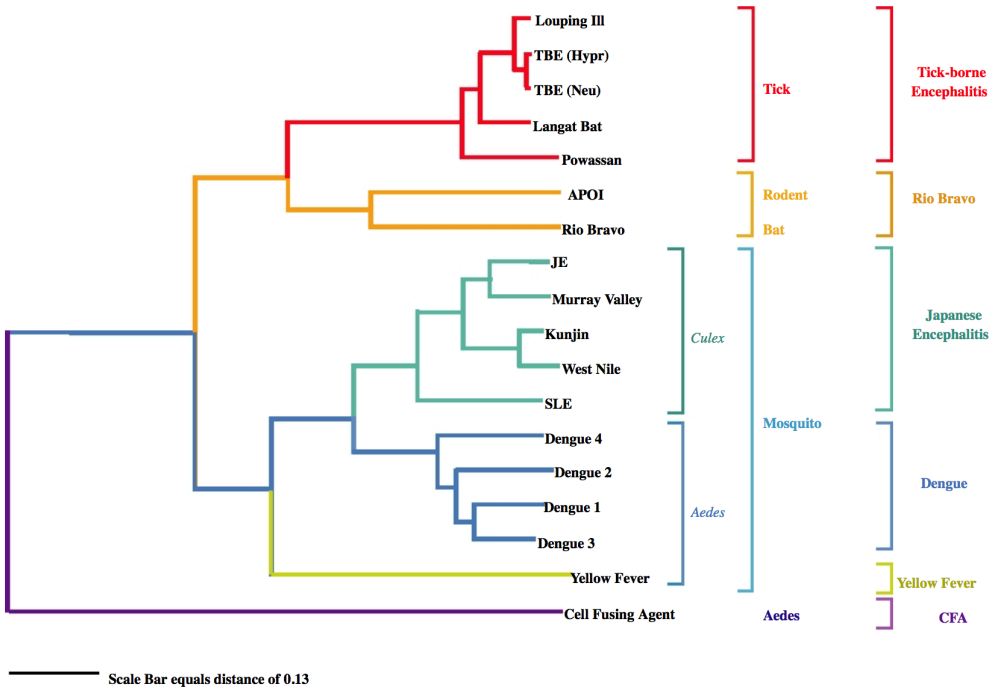

Fig 8. Phylogenetic tree of the Flaviviruses based on NS3 polyprotein region, built using the neighbor-joining method [24].

There are more than 80 different Flaviviruses [25] and most of them are important human pathogens, such as Yellow Fever virus (YFV), West Nile virus (WNV) and its Australian variant Kunjin virus (KUNV), Japanese encephalitis virus (JEV), Tick Born Encephalitis virus (TBEV), Saint Louis encephalitis virus (SLEV) and Dengue virus (DENV); the last one is continuing to spread and has emerged as a significant health threat throughout the world [26]. Flavivirus virions enter in the host cell by receptor mediated endocytosis. The viral mRNA has a cap I structure ($^{7Me}GpppA_{2'OMe}$C-RNA) lacking 3' poly(A) tail with an open reading frame (ORF) that is translated into a single polyprotein of about 3400 amino acids.

The viral polyprotein is processed by cleavage into 10 viral proteins, many of which are multifunctional and some membrane associated. Cleavage is effected by a combination of one or two viral encoded proteases and two or more cellular proteases. The viral proteins are classified into structural and non-structural (NS) proteins. The three structural proteins that form the virion framework are hosted at the 5' end of the RNA ORF. The remaining RNA codes for seven NS proteins involved in viral RNA replication and assembly. The structural proteins are identified as capsid (C; ≈13 kDa), precursor membrane protein (PrM; ≈18 kDa), and envelope (E; ≈54 kDa). The NS proteins are NS1 (≈39 kDa; [27]), NS2A (≈25 kDa; [28]), NS2B (≈14 kDa), NS3 (≈69 kDa), NS4A (≈16 kDa), NS4B (≈28 kDa; [29]), NS5 (≈104 kDa) [25]). The processing of the long polyprotein produced from the genome is complicated, and is presented in Figure 9 as an example of complex processing events that can occur in viral polyproteins associated with lipid bilayers.

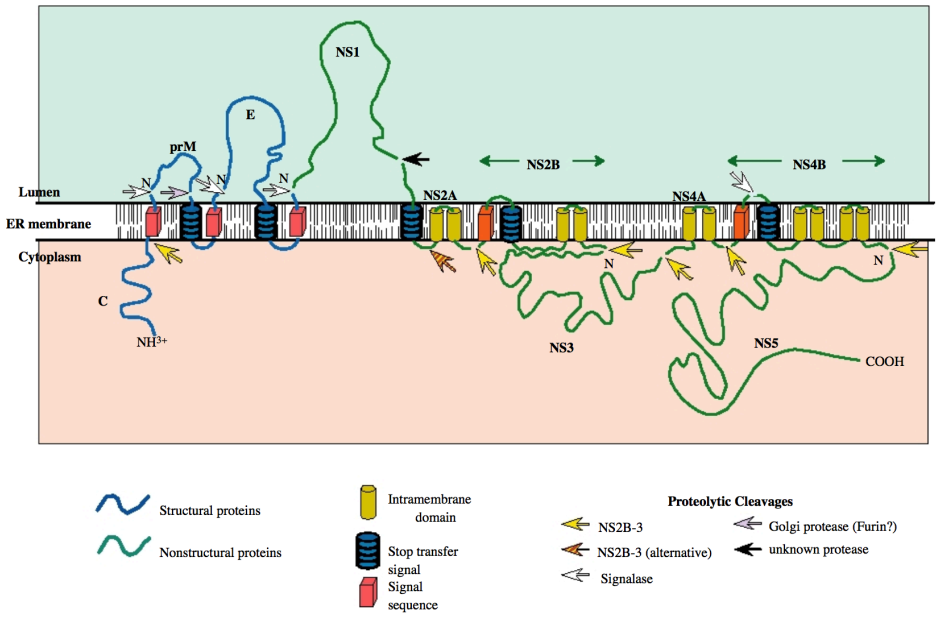

Fig 9. Processing of the Flavivirus polyprotein into the structural and non-structural proteins of the virus. The structural proteins (blue) at the N-terminus of the polyprotein are processed primarily by signalase, with one late cleavage in prM due to furin. The non-structural proteins (green) are mostly processed by the viral NS2B-NS3 protease. As indicated in the figure, the central 40 amino acids of NS2B interact with NS3, tying NS3 to the membrane; such interaction is essential for proteolytic function. The striped arrow shows the alternative site of cleavage within NS2A that may lead to an anchored form of NS1.

The nucleocapsid protein is 5′ terminal in the genome and is removed from the precursor polyprotein by the viral NS2B-NS3 protease. Two envelope proteins, prM (precursor to M) and E (envelope), follow.

NS proteins are cleaved in the following order: NS1, NS2A, NS2B, NS3, NS4A, NS4B and NS5. Their functions are summarised in Table 3:

Protein name	Functions
NS1	Required for RNA replication; other functions that are only poorly understood.
NS2A	Inhibits the production of interferon-α /β by infected cells; interacts with NS3 helicase domain.
NS2B	Required for the NS3 protease activity;
NS3	Serine protease domain (Pro) at its N-terminal; helicase domain at its C-terminal.
NS4A	It may has a role in assembly of the viral replicase on intracellular membranes.
NS4B	It may has a role in assembly of the viral replicase on intracellular membranes.
NS5	Methyltransferase domain at N-terminal; RdRp domain at C-terminal.

Table 3. Nomenclature for Flavivirus proteins and their functions.

Part of the NS proteins associate to form the viral replication complex and the new RNA synthesis co-localizes with NS1, NS2A, NS3, NS4A and NS5 ([30]; Figure 10).

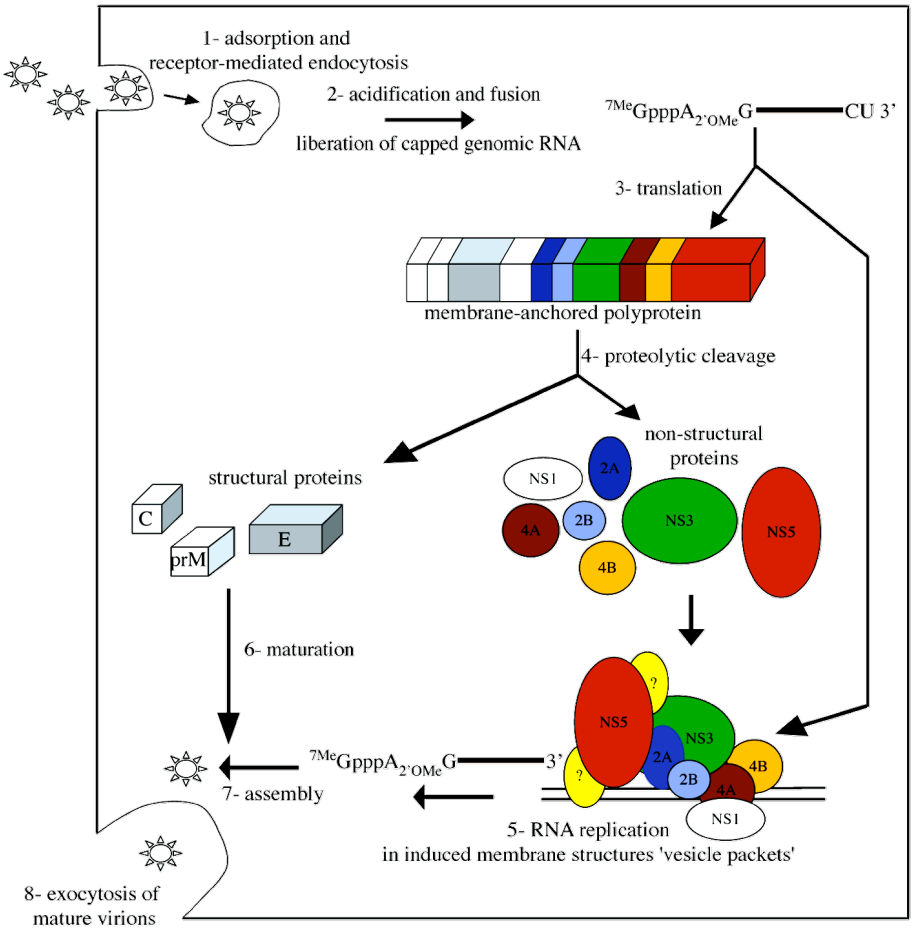

Fig 10. Replication cycle of Flaviviruses. After recognition of the capped genome by cellular ribosomes, its translation produces a polyprotein comprising three structural and seven non-structural proteins. The non-structural proteins associate to form the viral replication complex, which is active in induced membrane structures called " vesicle packets " in the cytoplasm, as shown in DENV-2 and KUNV infected cells [30].

After the formation of the replication complex, negative-sense RNA is produced and used as a template for the synthesis of new positive-sense viral RNA, to be assembled into the newly produced viral particles.

1.5 Flavivirus RdRp

With a molecular mass of about 100kDa, NS5 is the largest flaviviral protein; NS5 is also the most conserved protein across the genus. Early on, a motif of AdoMet-dependent MTases was identified within the N-terminal domain of NS5 [31], whereas RdRp motifs were identified in the NS5 C-terminal domain [18,32-34].

As soon as the first polymerase structure became available [35], sequence comparisons allowed identification of a number of conserved motifs involved in catalysis, notably those involved in positioning the incoming nucleotide and the catalytic divalent ions [35,36]. The HCV-NS5B crystal structure was the first complete RdRp structure solved [37-39]; it confirmed that the general architecture of polymerases is conserved in viral RdRps. They adopt a typical RdRp right-hand structure comprising three subdomains: fingers, palm and thumb (Figure 11).

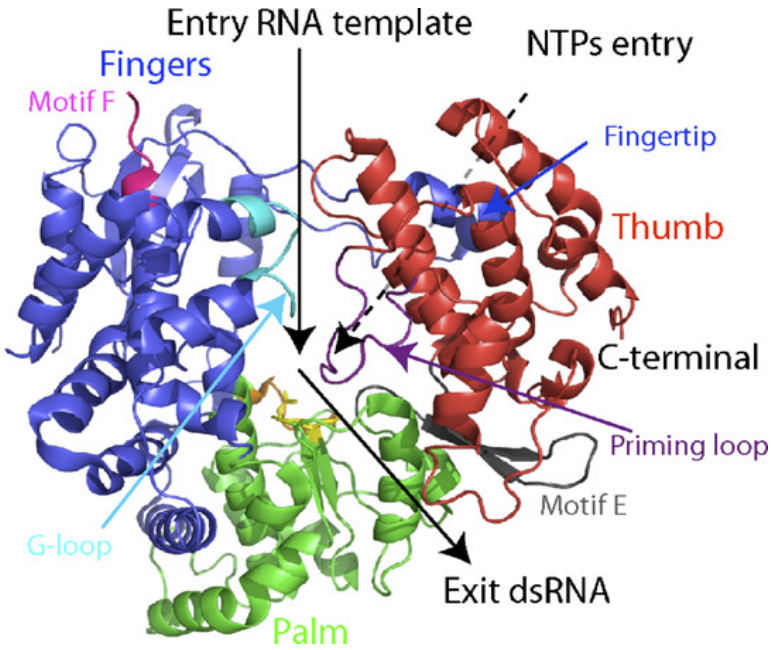

Fig 11. Overview of the Flavivirus RdRp structure based on WNV NS5Pol [40] as an example; a "Front" view is presented here in ribbon representation. Fingers, palm and thumb subdomains are colored in blue, green and red, respectively. The ssRNA template entry and the dsRNA exit are shown by black arrows. A dotted arrow points to the NTP entry tunnel at the back of the RdRp. Motifs A, C, E, F, the G-loop and the priming loop are colored in orange, yellow, grey, magenta, cyan and purple, respectively. The Asp residues of catalytic motifs A and C (Asp533, Asp663 and Asp664) are represented as stick models. The active site GDD belongs to palm domain. N-ter and C-ter indicate the termini of the RdRp domain.

Flavivirus NS5RdRp domains display a closed conformation, where fingers and thumb subdomains are connected. This is a characteristic of RdRps and in particular of primer-independent (*de novo*) RdRps [41]. A structural element, named priming loop, provides the initiation platform. It belongs to the thumb subdomain and points towards the active site in the palm. The active site is located at the intersection of two tunnels (entry and exit RNA tunnels). Other *de novo* RdRps solved in complex with ssRNA

template, NTPs and/or dsRNA product [42-44] suggest the following scenario shown in Figure 11. The first tunnel, located between the fingers and the thumb, should allow the ssRNA template to access the active site. The second tunnel, roughly perpendicular to the first, stretches across the entire protein. The incoming NTP should arrive from the back of the tunnel and, after the polymerization has started, the nascent dsRNA should go out through the front of this tunnel. However, as for other *de novo* RdRps, a conformational change is necessary to avoid a steric clash with the priming loop and allow neo-synthesized RNA to exit.

Special features of Flavivirus NS5RdRp structures are as follows [45]: (i) the fingers subdomain is captured in a pre-initiation conformation since motif F, normally comprising the NTP-binding sites, does not form the upper part of the NTP tunnel but is perpendicular to its normal position and partially disordered. Additionally, the fingers subdomain presents a loop, named G-loop, which protrudes towards the active site. The G-loop harbours RdRp motif G in primer-dependent RdRps [46,47]. This loop may play a regulatory role similar to the C-terminal in other RdRps [19,48,49]. In summary, a concerted conformational change of motif F and G-loop of the trapped pre-initiation conformation is expected before Flavivirus NS5RdRp initiate RNA synthesis. (ii) The priming loop is provided by the thumb subdomain, as observed for other *de novo* RdRps (bacteriophage phi6, HCV and BVDV RdRps) [37-39,42,50], but does not host any secondary structure. Two aromatic residues Trp795 or His798 for DENV NS5RdRp (Trp800 and His803 for KUNV RdRp), may act as initiation platform stacking with the priming nucleotide. (iii) Two Zn ions were found, one in the fingers and one in the thumb subdomain. The latter is localized at a supposed hinge position between the thumb and the palm subdomains. It

might play a role in the regulation of the conformational change between initiation and elongation state of Flavivirus NS5RdRps. (iv) Two NLSs (Nuclear Localization Signal) are present at the surface of the fingers subdomain. The NLS of DENV-2 NS5 has been shown to be functional, and the transport of NS5 to the nucleus vital for virus replication [51]. In contrast, KUNV NS5 does not localize in the nucleus. Subtle differences in NLS geometry and charge distribution may be responsible for distinct behavior towards nuclear import in closely related viruses, but this is not yet deducible from the structures. It is still unknown whether NS5 of DENV-3 localizes to the nucleus [45].

1.6 Antivirals targeting RdRp

The four DENV serotypes have considerably expanded their geographic distribution in recent years. With billions of people at risk, more than 50 million cases, and 12500 – 25000 deaths annually, DENV is considered an emerging pathogen in a growing number of countries [52].

In particular, the presence of four DENV serotypes has complicated the design of vaccines because incomplete protection against one serotype may influence the disease outcome once infection is established by a different serotype, through a process referred to as antibody-mediated disease enhancement [53]. WNV was detected for the first time in the Americas in 1999; the virus is now endemic on this continent [54]. During the last decade, more than 36000 human cases of West Nile were reported in the US, including more than 1500 fatalities (Centers for Disease Control, 2013. WNV Infection, vol. 2013. Available from: http://www.cdc.gov/ncidod/dvbid/westnile/index.htm).

The Noroviruses are one of the most common causes of acute

gastroenteritis worldwide, infecting both children and adults. In a recent report from CDC (Centre for Desease Control) on outbreaks occurring in the US from 1991 to 2002, NV infections were recognized as the most common cause of viral gastroenteritis in all ages in the US, accounting for about 33% of all outbreaks [55]. Transmission of NV occurs via the fecal-oral route, but virus can be transmitted via aerosols, as observed during explosive vomiting [56]; [57]; [58]. The environmental resistance of NV combined with their high infectivity (with an infectious dose of 10–100 viral particles), facilitates their efficient transmission. Human susceptibility to infection by Noroviruses is also dependent on the blood group of the individual (A, B, O). The histo-blood group antigens (HBGA) are one of the recognized binding receptors for noroviruses [59]; [60]; [61]; [62]; [63].

There is thus an urgent need for antiviral drugs to treat life-threatening infections with Flaviviruses and Noroviruses.

Because human cells lack RdRps, this enzyme appears to be one of the most promising targets for antivirals against viruses that utilize polymerases for replication. Therefore, it is not surprising that out of the 30 compounds that are currently marketed in the US for treatment of viral infections, 15 are RdRp inhibitors, especially nucleoside analogs. However, based on past experience with the development of drugs that are now in clinical use, the RdRp may prove to be the target with the best chance of success. The enzyme forms part of a multimeric complex that plays a crucial role in viral genome replication, but because it is encoded by the viral genome, and has no cellar counterpart, there are no toxicity issues [45].

Viral polymerases have been clinically validated as the target of both nucleoside (NI) and non-nucleoside inhibitors (NNI). Nucleoside analogues are generally converted to nucleotide analogues by host cell kinases. NIs

target the active site of the polymerase. They can either compete with natural NTP substrates or/and act as 'chain terminators' [64], or cause a mutational 'error catastrophe' by being incorporated into the elongating nascent RNA molecule [65]; [66]. NIs have been discovered through a rational search of substrate analogues, and they often possess a broad-spectrum antiviral activity. They also provide the greatest barrier to resistance [67]. Few molecules have been reported so far as effective RdRp NIs. Before a nucleoside can terminate a viral RNA chain, it must penetrate into the cell, be converted to its triphosphate derivative, be recognized by the viral polymerase, and incorporated into the viral RNA chain. Therefore, nucleosides have complex and unpredictable SAR (Structure Activity Relationship) [68].

The second category of compounds, NNIs, bind mainly to allosteric surface cavities of the target polymerase. They may induce a conformational change that causes the polymerase inactivation, or trap it in a given conformation avoiding an essential conformational transition between initiation and elongation. Allosteric inhibition has been shown to be a highly effective strategy [69] that can be improved by rational structure-based design [70].

Inhibitors of protein–protein or protein–RNA interactions involving viral polymerases are less explored as antiviral drugs. Effective antiviral molecules that seem to inhibit interactions of the viral polymerase within the replicative complex have been reported, *e.g.* for herpes virus [71] and pestiviruses [72]; [73]. As a whole, the search for antivirals against RdRps and RNA replication can be considered to be in its initial phase and RdRp crystal structures will help advancing the whole process.

Our knowledge on Flavivirus RdRp structures allows us to perform a

molecular surface shape analysis, with the aim to identify cavities that could potentially correspond to allosteric inhibitor binding sites. An analysis of the surface of the DENV and WNV RdRps identified two conserved cavities (named cavity A and B) on the surface of the enzyme that could potentially be targeted by small-molecule inhibitors [45]. These cavities are both located within the thumb domain that includes the priming loop (Figure 12).

Cavity A is the largest with a volume of 169 $Å^3$. Residues building the cavity are listed in Figure 12C. In particular, Tyr867 forms the upper part of the cavity and could promote a stacking interaction with a ligand containing an aromatic ring. Residues 810–814 (main chain atoms), which constitute the end of the priming loop, form the lower part of the cavity. Binding of a compound in that cavity could thus potentially damage the conformational change of the priming loop required for the transition to elongation. Cavity B is located on top of the thumb and has a volume of 77 $Å^3$. Main residues lining this cavity are listed in Figure 12C. Three additional cavities are present only in WNV RdRp, located in the thumb (cavity C and D), and in the fingers subdomain (cavity E). The size and the shape of the predicted cavities are compatible with the binding of small-molecule inhibitors in potential allosteric sites, they could thus represent "druggable pockets". Especially cavity A and B, predicted for both DENV-3 and WNV RdRp, might be exploited as a starting point for structure-based drug design; a first possible approach being virtual screening.

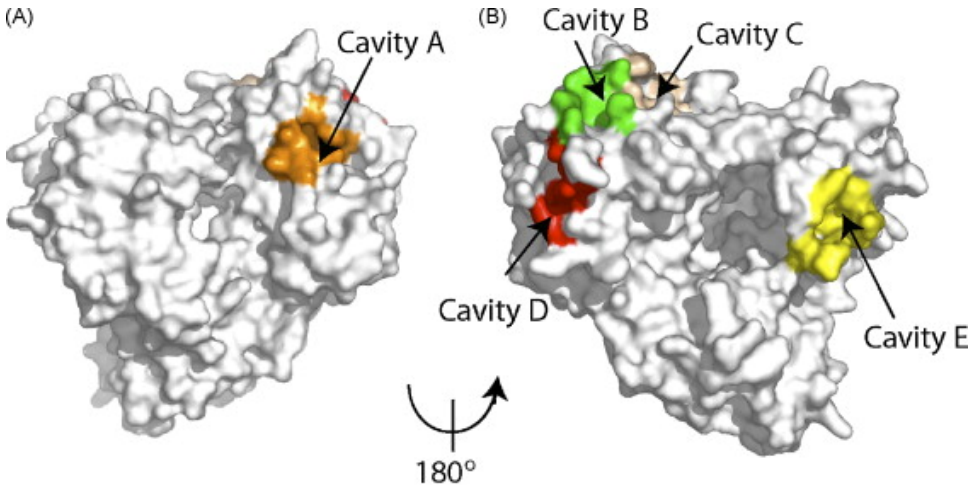

(C)

CavityA	K756, Q760, S763, N777, C780, V785, T806, E807, D808, M809, L810, Y882
CavityB	L326, L327, K329, T858, W859, N862, I863, A866

Fig 12. Locations of the cavities and putative allosteric sites on WNV RdRp. WNV RdRp cavities found by two programs, Pass and CastP, are represented in color on the surface and are named by letters. Cavities A and B were also found on DENV-3 RdRp. (A) "Front" view showing cavity A. (B) "Back" view showing cavities B, C and D. (C) DENV-3 residues building the putative allosteric sites A and B are reported.

Such type of shape/surface analysis hasn't been performed for Norovirus polymerases and just NI inhibitors are known against NV RdRps. Recently, two NNIs have been descovered: suramin and NF023 [74]. The crystal structures of mNV RdRp bound to each of the two inhibitors showed a common inhibitor binding site, close to the protein active site. In particular, the cleft occupied by the inhibitors is lined with several conserved positively charged amino acids, likely building the access route for the

incoming NTP that will be linked to the nascent RNA chain. Both NF023 and suramin may interfere with (i) entrance of new NTPs into the protein active site, by hindering the access channel and reducing the protein affinity for NTPs, due to the negatively charged sulfonates; (ii) the correct positioning of NTPs required for the formation of each new phosphodiester bond, and (iii) the exit route of the newly formed oligonucleotide chain, due to electrostatic repulsion.

2. Aims of my Thesis Project

RNA virus infections kill millions of humans annually, largely due to the lack of suitable vaccines and drugs to control them. The work carried out during my PhD has been developed in the context of the European project **SILVER (Small-molecule Inhibitor Leads Versus Emerging and neglected RNA viruses)**. The SILVER project is based on a consortium arising from the coordination of European and Asiatic leading molecular virologists, structural biologists, medicinal chemists and bioinformaticians. The ultimate aim of SILVER is to generate a state-of-the-art drug design programme to face new and emerging diseases caused by RNA viruses.

SILVER started in 2010 and since the beginning it required the collaboration of many groups, connecting chemistry, biochemistry, molecular biology, *in vitro* cell-based assay, *in vivo* animal-based assay, structural biology and computational studies (Figure 13).

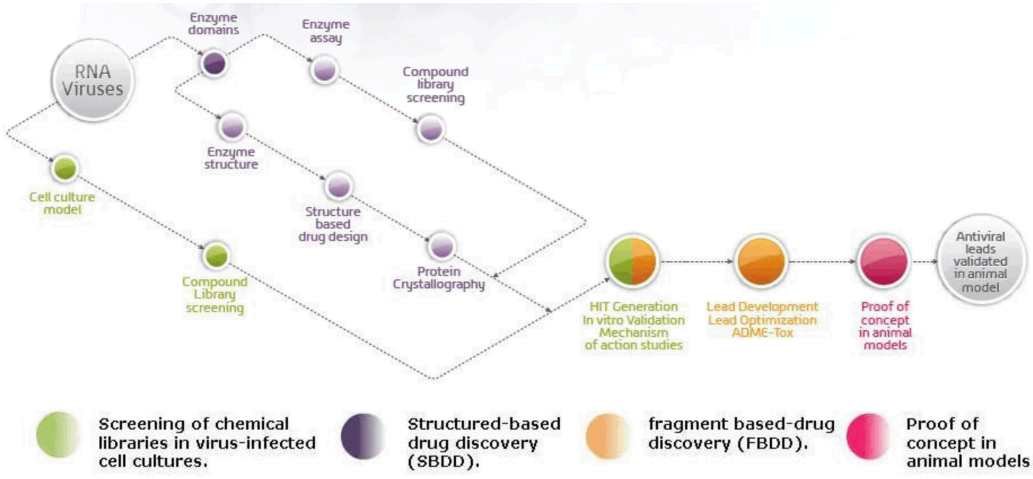

Fig 13. The SILVER project connects different research lines in the field of drug design and discovery against RNA viruses. The structural contribute is crucial for the project, providing

the basic information for the design and optimization of all the compounds synthesized, and for the analysis of protein/inhibitor complexes.

The SILVER project focuses its activities on selected medically important RNA viruses for which the development of drugs is considered essential (Dengue, entero- and paramyxoviruses), whereas other relatively neglected and emerging RNA viruses are explored to identify the most promising viral protein targets and antiviral compounds.

My PhD work focused on the study of the proteins involved in viral replication, in particular I worked on the identification of new NNIs against Flaviviruses (Dengue and West Nile) and Noroviruses (Human and Murine), using RdRp as main target.

My project targets challenging biological questions: 1) what kind of features the RdRp NNIs must hold, 2) how can we improve the RdRp interaction with already known inhibitors, 3) how can we improve cell permeability of already known inhibitors, 4) which are the inhibitory kinetic mechanisms of the identified compounds.

These goals have been tackled using different experimental approaches: *in silico* docking searches, X-ray structural biology, and *in vitro* polymerase assays (Figure 14).

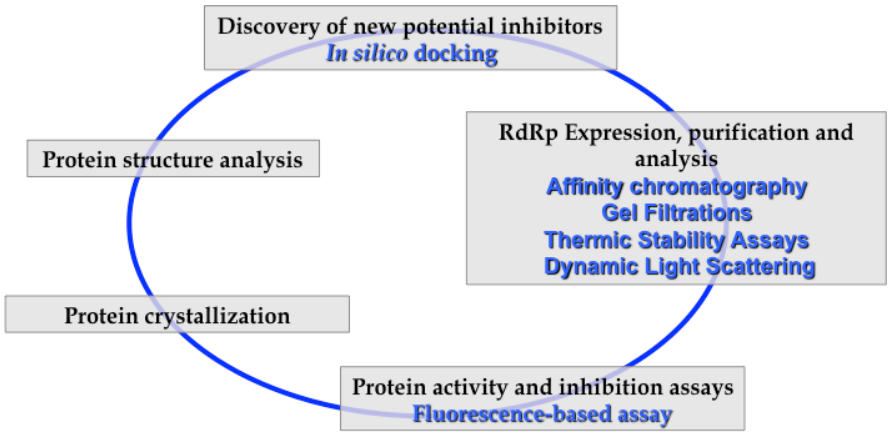

Fig 14. The PhD project has been developed in different steps. First of all the discovery of new potential inhibitors using *in silico* docking tecnique. To test the potential inhibitors, the targeted enzyme has to be expressed, purified and characterized. The protein activity is tested using a fluorimetric assay. When the potential inhibitors are active, their kinetics is studied. The last step is crystallization of RdRp-inhibitor complexes, and their 3D-structure analyses.

3. Main Results

3.1 Structural and functional analysis of Norovirus RdRp inhibitors Naf2 and PPNDS

The NNIs known to date as NV RdRp inhibitors are suramin and NF023 [74]. The two molecules display low IC_{50} values (suramin/mNV 70±3nM, suramin/hNV 24.6±0.8nM; NF023/mNV 200±2nM, NF023/hNV 71.5±0.9nM) but unfortunately, the molecular size and the high number of charged groups hamper cell permeability, with the result that the compounds are not active in cell-based assays.

Starting from these inhibitors, in order to reduce both the molecular weights and the number of the charged groups, I first investigated a fragment of the two molecules that, according to the crystal structures, mapped to the less flexible region of the suramin/NF023 binding site, within the enzyme active site. I focused on naphthalene-1,5- disulphonic acid (Naf2), which is the naphtalene head of suramin, and/or NF023 (Figure 15).

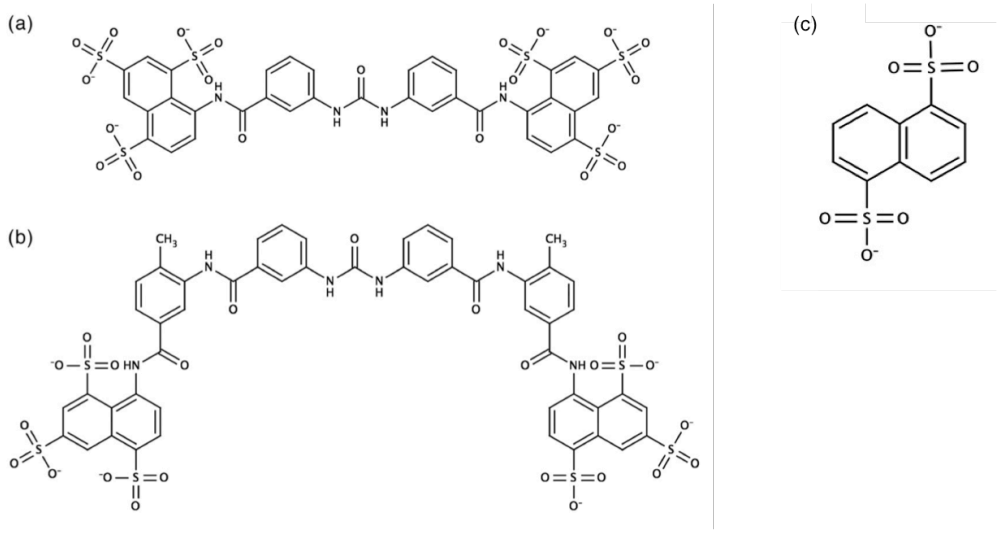

Fig 15. (a) Chemical structure of NF023, (b) chemical structure of suramin, and (c) chemical structure of Naf2

I performed the polymerase inhibition assays on both murine and human NV RdRp. The two proteins were expressed and purified as described in [75] in Prof. Rohayem's lab. The enzymatic activity test is based on an *in vitro* RNA synthesis fluorimetric assay (see Material and Methods in *Tarantino et al., Naphthalene-sulfonate inhibitors of human norovirus RNA-dependent RNA-polymerase, (2014) Antiviral Research 102: 23–28*- Part II). Naf2 displayed low inhibitory activity against the enzymes (IC_{50} values: Naf2/mNV 14147±1543nM, Naf2/hNV 15500±800nM); moreover, analysing the dose-response curves, it is clear that the number of bound inhibitor molecules is higher than 1.

The crystal structures of both NV RdRps, in the presence of Naf2, confirm the presence of an additional Naf2 molecule, located in the thumb domain, i.e. an additional binding site (site B), besides the one characterized for NF023/suramin (site A) (Figure 16).

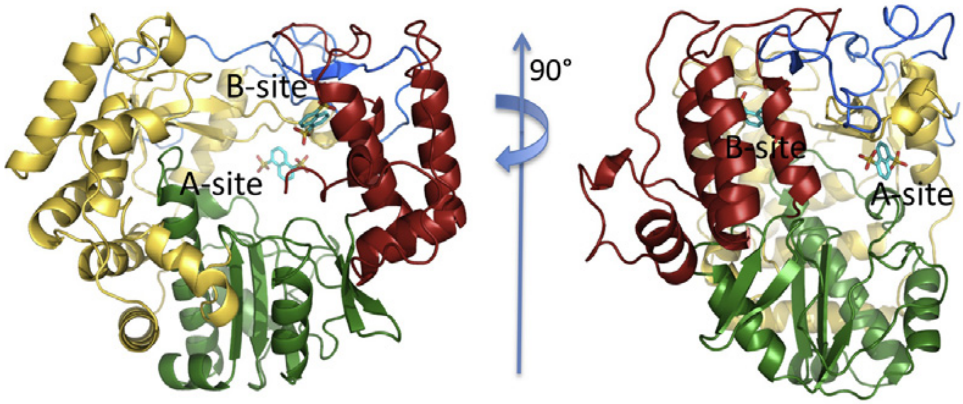

Fig 16. Crystal structure of hNV-RdRp bound to two Naf2 molecules, in the A-site and in the B-site. The overall structure of hNV-RdRp is shown as a cartoon: N-terminal domain (blue), thumb (red), fingers (yellow) and palm (green). The picture on the right is rotated by 90 degrees around the vertical axis.

In the B site, the negative charges of Naf2 sulfonates are balanced by arginine residues and the naphthalene ring is sandwiched between two glutammine residues. This site is close to the dsRNA exit channel.

To better characterize the new potential inhibitory site, we selected a structurally related molecule: Pyridoxal-5'-phosphate-6-(2'-naphthylazo-6'-nitro-4',8'-disulfonate) tetrasodium salt (PPNDS, Figure 17) which from a previous docking search was suggested to fall in a region close to the newly recognized binding site (site B).

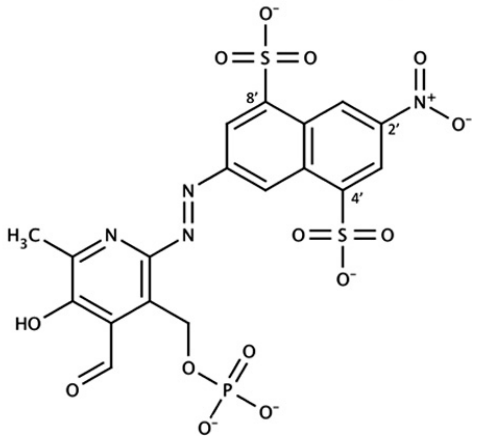

Fig 17. Chemical structure of PPNDS.

I performed the RdRp inhibition assays using PPNDS (see Material and Methods in *Tarantino et al., Naphthalene-sulfonate inhibitors of human norovirus RNA-dependent RNA-polymerase, (2014) Antiviral Research 102: 23–28; Croci et al., PPNDS inhibits murine Norovirus RNA-dependent RNA-polymerase mimicking two RNA stacking bases, (2014) FEBS Letters 588: 1720–1725*- Part II), which displayed low micromolar inhibitory activity *versus* both human and murine Norovirus RdRps (IC_{50} PPNDS/mNV 800±30nM, PPNDS/hNV 1000±90nM). I also analysed the kinetic mechanism of hNV RdRp inhibition by PPNDS with respect to the

substrate poly(C)/oligo(G)$_{12,}$ increasing the amount of the substrate and of the inhibitor. The Lineweaver-Burk plots, derived from the inhibition curves analysis, highlighted a non-competitive inhibition mechanism with respect to the substrate, with a *Ki* value of 0.52±0.05μM, indicating that the inhibitor is able to bind the free enzyme as well as the enzyme-substrate complex.

I performed also a thermofluorimetric assay in order to verify whether the selected compounds might induce some form of destabilization or denaturation of the enzyme. In general this is reflected by a variation of the protein melting temperature (T_m). hNV RdRp in the presence or absence of Naf2 displays the same T_m (respectively 36.9±0.5 ºC and 37.5±0.4ºC). In contrast, in hNV RdRp/PPNDS complex, the T_m increases slightly relative to hNV RdRp T_m (respectively 37.0±0.5ºC and 41.0±2.0ºC), implying some protein stabilization induced by the presence of the inhibitor.

The crystal structures of both human and murine NV RdRp/PPNDS were obtained only after soaking the protein with inhibitor in presence of dsRNA and GTP. This suggests that inhibitor binding to the protein requires local structural changes related to events in the catalytic cycle. NV RdRp/PPNDS complex crystal structures showed that the inhibitor bound to the secondary site blocking the exit of the newly synthesized RNA, confirming the relevance of this site for the inhibition of the enzyme. However, several differences between human and murine Norovirus RdRp/PPNDS structures were observed.

In the PPNDS/hNV RdRp complex structure, only a single molecule of inhibitor bound to site B was observed (Figure 18). The overall structure of the whole enzyme bound to PPNDS appears slightly more compact if compared to that of the inhibitor-free protein. Such overall effect is related to a small displacement of both the finger and the thumb domains toward the

active site, as a closing hand, and this is likely due to the interaction of the protein with dsRNA. In fact, the crystal structure shows residual electron density hosted between the fingers and thumb domains compatible with two or three RNA nucleotides, which have been only partially modeled in the refined structure, due to electron density ambiguities.

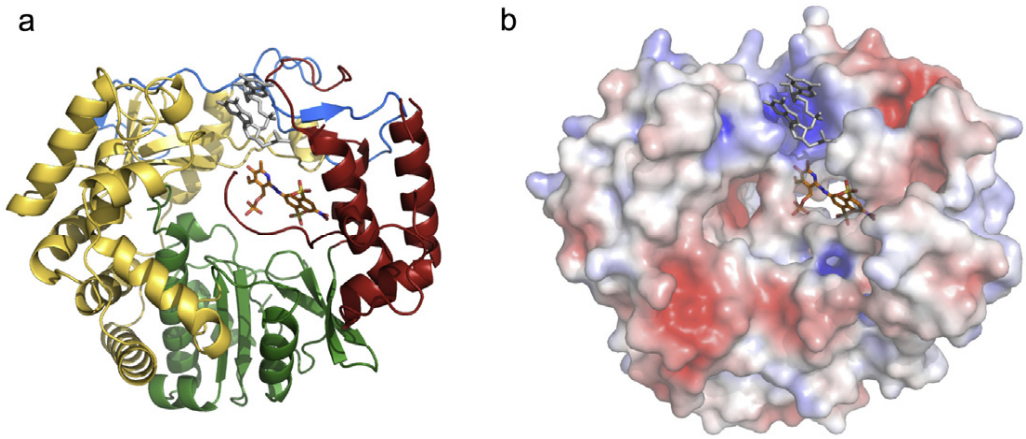

Fig 18. (a) Crystal structure of hNV RdRp bound to PPNDS in cartoon. PPNDS (orange carbon atoms) and a fragment of ssRNA, partially modeled into observed electron density (gray) are shown as sticks. (b) Same as (a) with protein surface colored by electrostatic potential.

In contrast, in the PPNDS/mNV RdRp complex structure two molecules of the inhibitor were found into the new site, blocking dsRNA formation. In particular the two molecules bound to mNV RdRp display an evident antiparallel stacking orientation, roughly aligned along the main alpha helices of the thumb domain (Figure 19a). They adopt an orientation rotated by about 60º relative to that observed for the single PPNDS molecule in hNV RdRp complex (Figure 19b,c).

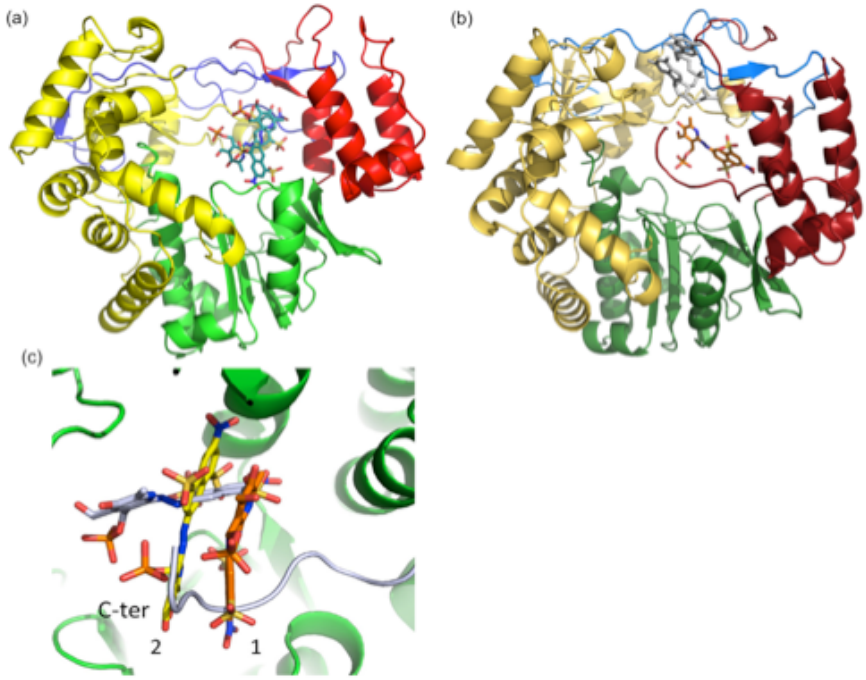

Fig 19. (a) mNV RdRp/PPNDS structure. The two molecules of the inhibitor are in antiparallel stacking interaction each other, (b) hNV RdRp/PPNDS structure. The single PPNDS molecule is rotated by about 60º relative to that in mNV RdRp, (c) superposition of the PPNDS molecules 1 and 2 bound to mNV RdRp (in orange and yellow) and PPNDS molecule bound to hNV RdRp (in grey).

3.2 Structural and functional analysis of suramin synthesis intermediates

In addition to the analysis of structurally related molecules, to reduce the molecular dimensions and the charged groups present in suramin, I planned chemical modifications of the molecule. The crystal structure of mNV RdRp in complex with suramin showed that only two of the three sulphonate groups of the suramin naphthalene rings establish ionic interactions with basic residues of the enzyme. On the basis of such structural information, in collaboration with Prof. Hwu's group, from

National Central University of Jhongli (Taiwan), we modified suramin removing one sulphonate group and isolating several intermediates of the chemical synthesis process (Figure 20).

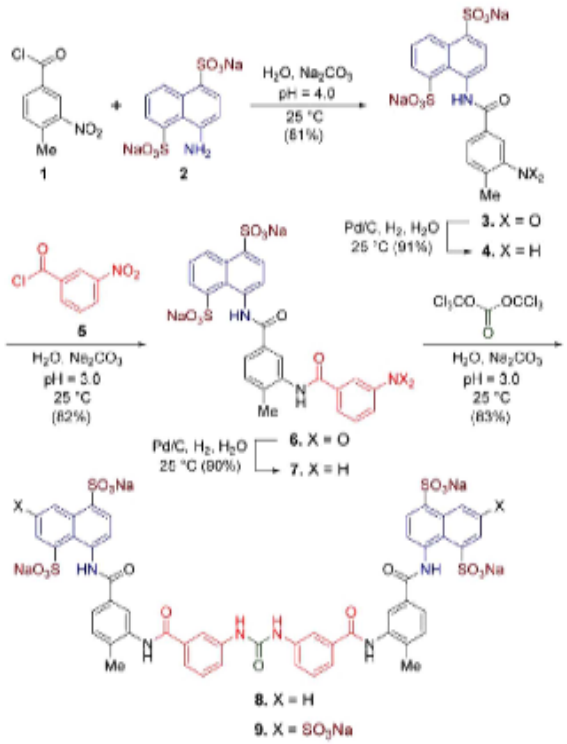

Fig 20. Suramin derivative 8 synthesis. Total synthesis of Suramin derivative 8 from commercially available starting materials. The Suramin molecule (9) is also shown for comparison.

I characterized compound 8 (Cpd8) together with lower molecular weight synthetic reaction intermediates using a fluorescence-based assay (see Materials and Methods in *Croci et al., Structural Bases of Norovirus RNA Dependent RNA Polymerase Inhibition by Novel Suramin-Related Compounds, (2014) PLoS ONE 9(3): e91765*- Part II).

The synthetic intermediates are less potent inhibitors than suramin, in particular against hNV RdRp (Table 4).

	IC_{50} (nM)	
Compound	**mNV RdRp**	**hNV RdRp**
3	700±10	1780±70
4	160±7	1100±200
6	115±15	1000±90
7	160±6	1100±50
8	60±4	28±2
Suramin (9)	70±3	27±3

Table 4. IC_{50} values of Suramin derivatives and Suramin (9) against mNV and hNV RdRps.

Cpd8 showed the same IC_{50} values of suramin. Since the structures of the two molecules are very similar, we assumed that Cpd8 binds the proteins in the same manner.

In order to analyze in details the interaction of the lower molecular weight intermediates hosting one sulphonate head with RdRps, I crystallized the enzyme with the compound showing the best inhibition, 4-[4-Methyl-3-(3-nitrobenzamido)benzamido]naphthalene-1,5-disulfonic Acid Disodium Salt (Cp6). Cp6 shows a logP higher than the other intermediates (logP -1.64) (see *Croci et al., Structural Bases of Norovirus RNA Dependent RNA Polymerase Inhibition by Novel Suramin-Related Compounds, (2014) PLoS ONE 9(3): e91765*- Part II). LogP is the logarithm of the ratio of concentrations of a compound in two immiscible phases at equilibrium. This coefficient is a measure of the difference in solubility of the compound in these two phases, and is prognostic to cell permeability.

In the high resolution crystallographic analysis of Cpd6 in complex with hNV RdRp (hNV/Cpd6: 2.02Å resolution), the naphthalene sulphonate head of Cpd6, the linked amido group and the phenyl methyl group were found in a location different from the suramin binding site (site A), but in the same binding site of PPNDS (site B). Density for the remaining part of the

compound was not visible due to conformational disorder. The unmodelled tail of Cpd6 would be hosted in the polar central region of the enzyme which accommodates dsRNA during elongation. This region is wide enough to allow conformational flexibility of the second half of the inhibitor, in agreement with the lack of an interpretable electron density signal (Figure 21). In mNV RdRp/Cpd6 crystal structure (resolution 2.30Å), the naphthalene disulphonate head binds to the same location identified for hNV RdRp and the entire compound is modelled in the electron density. The compound is rotated of about 20° in comparison to that in hNV RdRp structure.

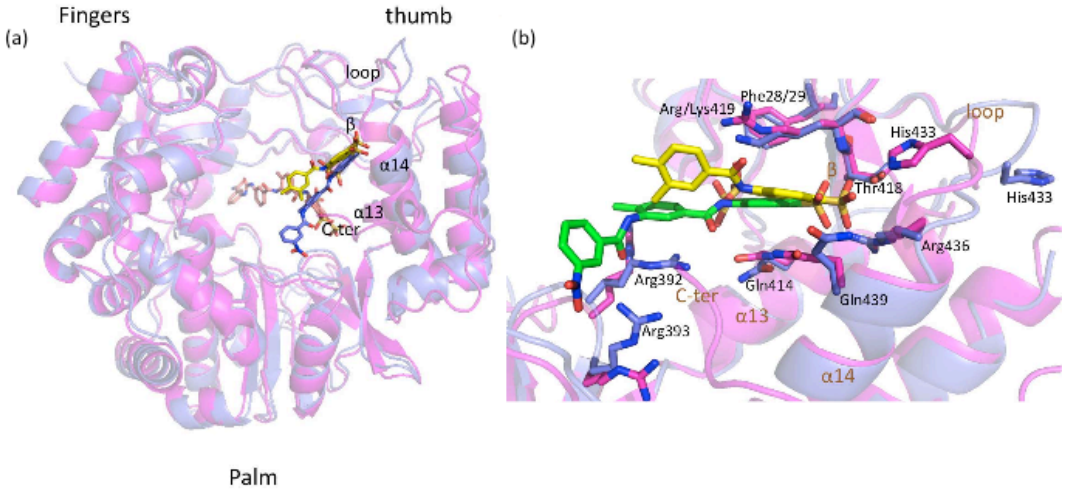

Fig 21. (a) Superposition of the crystal structures of hNV RdRp in cartoon (magenta) bound to Cpd6 (carbon atoms in yellow) in sticks, onto mNV RdRp in cartoon (blue), bound to Cpd6 (carbon atoms in green) in sticks. (b) Detail of the superposition of hNV and mNV RdRps. The interacting amino acids are shown as sticks.

3.3 Structure and biochemical characterization of a Flavivirus RdRp inhibitor

Since the work showed in this paragraph is still ongoing, the results are not published yet. For reasons of confidentidity no chemical structures can be shown.

In a search for new potential NNIs Flaviviral inhibitors, I chose to explore a wide region around the active site of Dengue RdRp as the targeted inhibitor binding site. A virtual screening procedure was firstly set up with the aim of testing a library of compounds. The crystal structure of DENV3 RdRp (pdb id: 2J7U [40]) was employed as a model for the protein, selecting the entry RNA template site as the centre of the docking search. This region (~15.2 nm^3; Figure 22) was explored using a library of 203 compounds (UNIPG library) (Figure 23) as described in *Flavivirus RdRp Materials and Methods* paragraph - Part III.

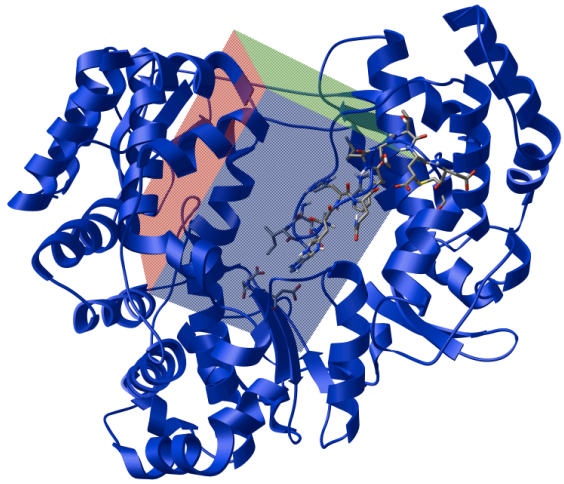

Fig 22. *In silico* docking of UNIPG library into DENV-3 active site. The box highlights the region explored (15.2nm^3). This region includes the active site residues GDD belonging to palm domain and the priming loop belonging to thumb. GDD and priming loop are shown in sticks.

Molecules belonging to UNIPG library were designed by Dr. Manfroni's lab as potential inhibitors against the *Flaviviridae* family. The docking search produced a list of compounds with predicted binding free energy values (ΔG) ranging between - 5.65 kcal/mol and -10.05 kcal/mol. Among the top compounds ranked by the docking search, we selected HeE1-2SO2 (ΔG = -10.05 kcal/mol) and HeE1-2Tyr (ΔG = -9.52, kcal/mol) to be used for *in vitro* testing of inhibitory activity *versus* West Nile and Dengue virus RdRps.

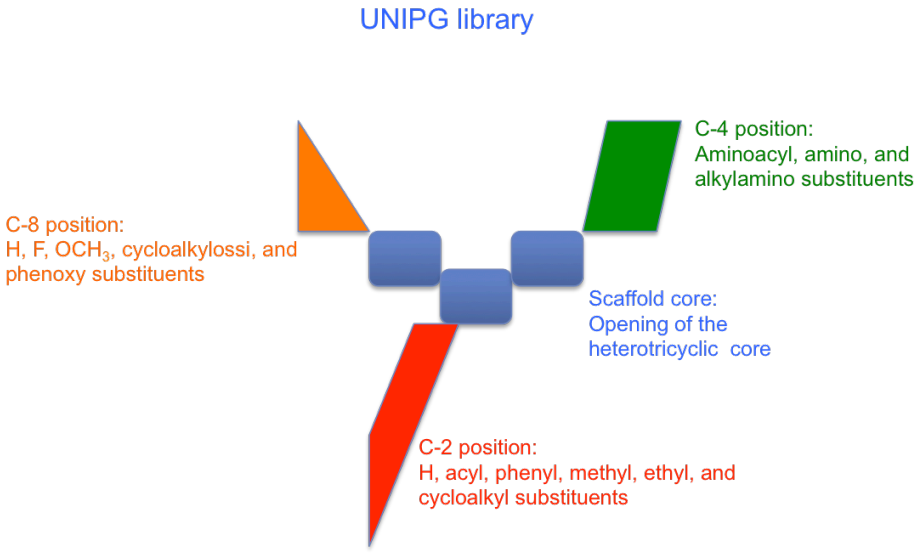

Fig 23. UNIPG library is composed of heterotricyclic compounds with a scaffold core and three different substituents.

In vitro RNA synthesis assays were performed using a fluorescence-based assay (*Flavivirus RdRp Materials and Methods* paragraph - Part III). The results have been analyzed with GraFit5 and IC_{50} values have been calculated. Under these experimental conditions, HeE1-2SO2 and HeE1-2Tyr resulted to inhibit RdRp activity with IC_{50} values in the micromolar

range; in particular HeE1-2SO2 /DENV-3 RdRp 2.8±0.5μM and HeE1-2SO2 /WNV RdRp 2.5±1.3μM, whereas HeE1-2Tyr /DENV3 RdRp 3.5±0.2μM and HeE1-2Tyr /WNV RdRp 3.4±0.4μM.

I also analyzed the kinetic mechanism of RdRps inhibition by HeE1-2Tyr, for both DENV3 RdRp and WNV RdRp. The Lineweaver–Burk plots derived from inhibition curves for both RdRps (Figure 24) highlighted a non-competitive inhibition mechanism relative to poly(rC) as substrate, with a DENV RdRp/ HeE1-2Tyr *Ki* value of 0.64 ± 0.08 μM and WNV RdRp/ HeE1-2Tyr *Ki* value of 1.59 ± 0.50 μM.

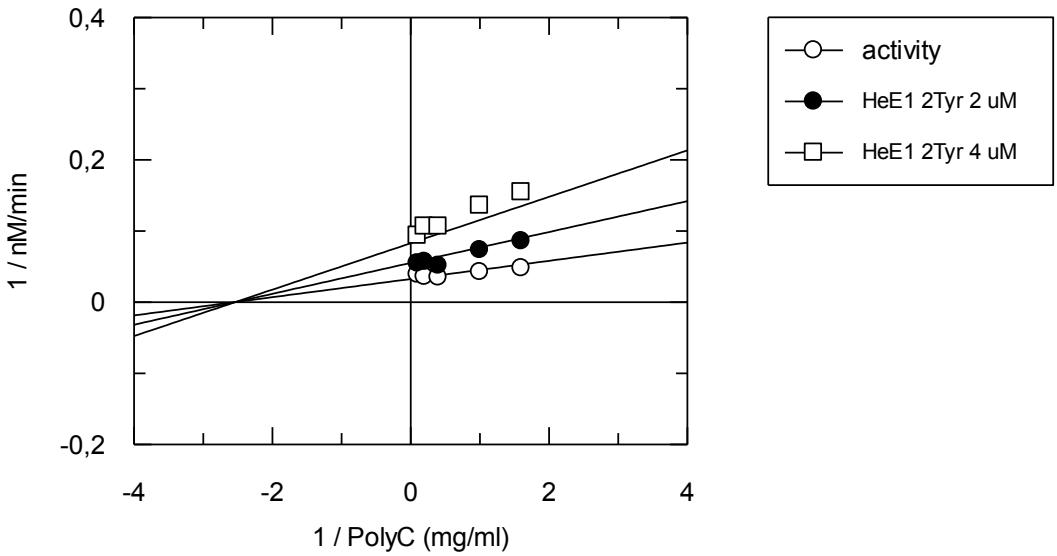

Fig 24. Lineweaver–Burk double reciprocal plot for the non-competitive inhibition mechanism of DENV3 RdRp activity by HeE1-2Tyr, relative to Poly(rC) as substrate.

The specificity of the HeE1-2Tyr inhibition was verified by excluding any off-target effects on the overall native protein fold, such as ligand-induced destabilization/aggregation/denaturation. To this aim, thermal denaturation analysis using Sypro-orange as the fluorescent probe

were performed. The WNV and DENV RdRps T_m resulted to be essentially the same in the absence (WNV RdRp Tm=46.3±0.4 °C; DENV RdRp Tm=39.6±0.1 °C) or in the presence (WNV RdRp Tm=47.3±0.3 °C; DENV RdRp Tm=39.6±0.1 °C) of HeE1-2Tyr.

All the thermofluorimetric results proved that the RdRps inhibition is not due to inhibitor-linked adverse effects on enzyme.

HeE1-2Tyr and HeE1-2SO2, together with other 13 analogues present in the UNIPG library, were tested for their antiviral activity in cell assays (HeK 293/Vero E6). Six of the selected compounds showed high cytotoxicity to uninfected cells, and thus were abandoned; eight compounds did not show any activity, probably due to low cell permeability, while HeE1-2Tyr proved to be a very promising hit.

Upon treatment of infected Vero E6 cells, HeE1-2Tyr was able to inhibit an Ugandan strain of WNV as well as Dengue viruses (Table 4). The cytotoxicity of HeE1-2Tyr *versus* Vero E6 cells was 75μM, allowing a reasonably good selectivity index for a starting hit compound. In human HeK 293 cells, the cytotoxicity of HeE1-2Tyr was slightly higher (CC_{50} ≈ 40μM) and the compound was found to inhibit a clinical strain of YFV with an IC_{50} ~2.6μM (Table 5) (These data were obtained in Prof. Querat's lab, University of Aix, Marseille).

Virus	**HeE1-2Tyr IC_{50} (μM)**
YFV (Bolivian clinical strain)	2.6
WNV	2.6
DENV-1	8.8
DENV-2	8.8
DENV-3	10.7
DENV-4	5.6
JE	>10

Cells	CC_{50} (μM)
Vero E6	75
HeK 293	40

Table 5. IC_{50} and CC_{50} values of HeE1-2Tyr against several Flaviviruses.

I was able to grow WNV RdRp crystals, as described in *Flavivirus RdRp Materials and Methods* paragraph - Part III, and soaked them with HeE1-2Tyr and HeE1-2SO2 (15mM and 5mM final concentrations, respectively). The crystals soaked with HeE1-2SO2 (belonging to the space group I222, with only one molecule per asymmetric unit) diffracted at maximum resolution of 2.7Å, while the crystal soaked with HeE1-2Tyr diffracted at a very low resolution (4.2Å). We solved the structures by molecular replacement (the search model was pdb 2HFZ) and refined to a final crystallographic R-factor/R-free values of 22.58/26.74% for WNV RdRp/HeE1-2SO2.

Although the electron density of the inhibitor is not clear enough, I could deduce that HeE1-2SO2 interferes with the location of the RdRp priming loop that appears to be disordered in the crystal structure of the complex (Figure 25). The priming loop is composed of residues 796-809 in WNV RdRp; in our refined structure WNV RdRp residues Trp800, Ser801, Ile802 and His803 are not visible probably because they adopt various conformations upon interaction with HeE1-2SO2.

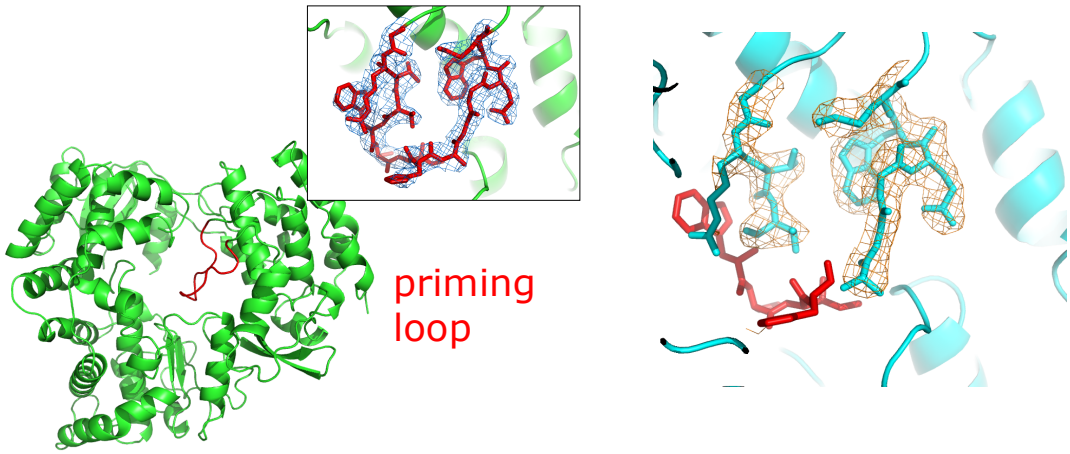

Fig 25. (a) Inhibitor-free WNV RdRp (2.7Å) (green) in which all the residues belonging to priming loop are visible (red). (b) WNV RdRp/HeE1-2SO2 (2.64Å) complex in light blue. Some priming loop residues do not show electron density in the presence of the inhibitor.

My hypothesis is enhanced by the crystal structure of WNV RdRp/ HeE1-2Tyr. Also in this structure three residues (Thr799, Trp800 and Gly805) lack proper electron density. Such evidence is in agreement with the *in silico* docking searches for the binding site of the two compounds, which are predicted to interact with residues of the priming loop and with one active site residue (Asp664), between the thumb and the palm domains. Since Trp800 and His803 side chains may help orienting the base of the priming nucleotide via a stacking interaction during the catalytic cycle, their conformational perturbation could explain the loss of activity caused by HeE1-2SO2/HeE1-2Tyr.

4. Conclusions and Future Prospects

In the three years of my PhD project, I have been involved in the identification of new non-nucleotide-like inhibitors against Noroviruses (murine and human NV) and Flaviviruses (West Nile virus), using RNA dependent RNA polymerase (RdRp) as the main target.

Noroviruses are the major cause of epidemic viral gastroenteritis, worldwide, responsible for about 200.000 deaths/year, however no vaccines nor antivirals are available. To this purpose, starting from a previous work [74] in which the structures of mNV RdRp in complex with suramin and NF023 were solved, I first analyzed the potential role of the naphtalene-head of the inhibitors (Naf2). Suramin and NF023 binding site (site A) is located along the access pathway of NTPs to the enzyme active center. Accordingly, this site is lined with positively charged residues whose conformational flexibility helps promoting the diffusion of NTPs toward the catalytic site. Such structural features are unlikely to make this inhibitor binding site an ideal target region for structure based drug optimization. Although enzymatic assays showed that the selected fragment retains marginal inhibitory activity, the NV RdRp/Naf2 complexes revealed an unexpected binding site (besides the already characterized site A) for Naf2, located in the RdRp thumb domain (site B). Interestingly, the site B is located in a position that is roughly structurally equivalent to the benzothiadiazine inhibitor binding site in the Hepatitis C Virus RdRp [76]; [77]; [78]. Naf2 binding to two distinct sites is also suggested by the inhibition mechanism analysis, which shows a Hill coefficient higher than 1. In order to further characterize the site B, we selected PPNDS, a naphthalene sulfonate-based compound. PPNDS is able to inhibit the NV RdRp activity with an IC_{50} close to that observed for suramin or NF023. The crystal structure of the

hNV RdRp/PPNDS complex shows that the compound is anchored to the protein mostly through its naphthalene moiety. The improved inhibitory efficacy, relative to Naf2, is likely dependent on PPNDS pyridoxal moiety that extends toward the enzyme active site. The relevant inhibitory difference between Naf2 and PPNDS in hNV RdRp are probably due to the fact that PPNDS can fix the C-terminal end of the enzyme inside the active site, blocking access of both the ssRNA template and the NTPs.

In mNV RdRp/PPNDS complex crystal structure, instead, two PPNDS molecules bind the enzyme at site B. The two inhibitor molecules display an antiparallel stacking interaction and adopt an orientation rotated by about 60° relative to that observed for the single PPNDS molecule bound to hNV RdRp. Such significant changes are likely related to the insertion of the C-terminal segment of the hNV RdRp (aa. 490-506) inside the enzyme active-site region. In mNV RdRp the C-terminal segment is disordered after Gly488, thus leaving more room in the active site region for the incoming inhibitory molecules.

It must be stressed that the two PPNDS molecules fall in a location close to the region that would be taken by the newly formed ssRNA chain, as inferred by superposition with the structure of hNV RdRp bound to dsRNA (Figure 26). In particular PPNDS-1 and PPNDS-2, after superimposition, fall on nucleotides n-2 and n-1 respectively (n is the nucleotide that will be linked to the incoming NTP). The structural results on mNV RdRp show that PPNDS can display properties allowing it to mimic the stacking interaction of two linked bases in RNA.

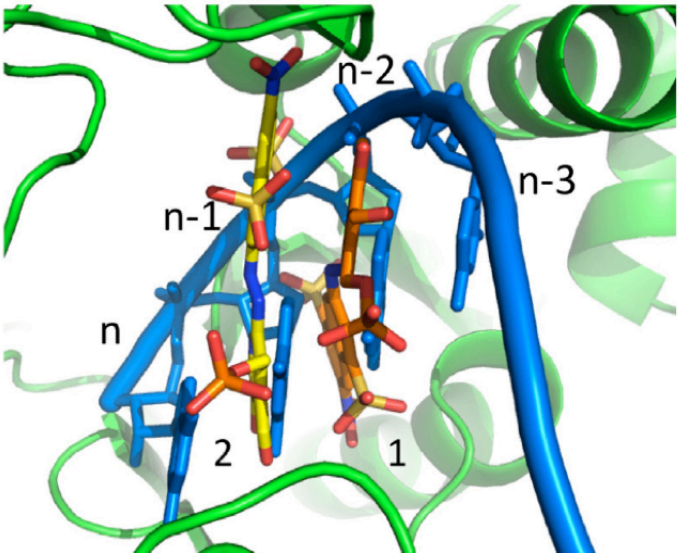

Fig 26. Detail of superposition of mNV RdRp in complex with PPNDS molecules (in yellow and orange) on hNV RdRp bound to dsRNA (in blue; n=nucleotide; pdb ID 3BSN).

Such a RNA-like property of the inhibitor might be improved by covalently linking the phosphate moieties of the two PPNDS molecules that are found in close contact in the X-ray structure.

Concerning the issue of cell permeability for suramin and NF023, a strategy adopted was to synthesize suramin derivatives with a lower number of charged groups. The solubility of chemical entities in water plays an important role in their development as a lead for new drugs, and it is related to the structure–activity relationship. The apparent partition coefficient (P) is a useful parameter for understanding the behavior of drug molecules. Often it is used to predict the distribution of a drug compound in a biological system, the log P value being related to absorption, excretion, and penetration [79]. The measurement of the apparent partition coefficient

provides a simple *in vitro* method to predict the behavior of a compound in the body and to select the most promising drug candidates from a large pool of ionizable compounds. Among the compounds considered, Cpd6 showed a better hydrophobicity than suramin (log P –1.64 *versus* –3.42, respectively).

Our analysis on the NV RdRp/Cpd6 complex 3D structure shows that the sulphonate groups on the naphthalene sulphonic head interact with the RNA binding loop (residues 433–440). The crystal structures of hNV RdRp/RNA complexes (3BSO and 3H5X) [20]; [21] revealed significantly different locations in the RNA-binding loop relative to the free RdRp, showing specific RNA-induced conformational changes of this loop [22]. Binding of Cpd6 might freeze the loop of hNV RdRp in the conformation found in the free enzyme, hindering efficient RNA binding.

In the hNV RdRp/Cpd6 complex, the inhibitor electron density fades rapidly after the amido group linked to the naphthalene di-sulphonate moiety. Thus, the lower inhibitory potency of Cpd6 *vs.* hNV RdRp may be linked to failure of establishing enzyme/inhibitor stabilizing interactions along the whole inhibitory molecule, which appears to remain flexible for about 50% of its scaffold.

On the contrary, in the mNV RdRp/Cpd6 structure, the inhibitor could be completely modeled because of the different disposition of the naphthalene head due to loss of interaction with residue His433. The additional interactions of Cpd6 with residues Arg392 and Arg393 are in agreement with the higher potency of Cpd6 *versus* mNV RdRp relative to hNV RdRp.

The newly discovered NV RdRp inhibitor binding site, mapped by Cpd6 and by PPNDS, together with the different conformational behaviors displayed by Cpd6 bound to NV RdRps, appear as two novel structural bases

to be exploited for the design and development of more potent and selective hNV RdRp inhibitors.

In parallel to the Norovirus work, I focused on Flaviviruses that are emerging pathogens of increasingly public health concern in the world. For most Flaviviruses such as Dengue virus and West Nile virus neither vaccine nor antiviral treatment is available [45]. Flavivirus RdRp is essential for viral replication also because its priming loop constitutes a platform stabilizing the RNA synthesis initiation complex [40]. Conformational changes of this loop, not yet characterized by structural studies, are presumably required to shift to an RNA synthesis elongation mode. Residues in the priming loop (residues 796-809 in WNV RdRp, and 782-809 in DENV RdRp) are used to orient the base of the priming nucleotide via a stacking interaction. In WNV RdRp, Trp800 and His803 may perform this function [40].

Such information brought us to design small-molecules (NNIs) that could bind Flavivirus RdRps in the entry RNA template channel. We have designed different molecules and selected, through *in silico* docking, potential inhibitor compounds. *In vitro* enzymatic assays confirmed our *in silico* predictions, showing HeE1-2SO2 and HeE1-2Tyr as good inhibitors. The properties of these molecules have been shown also in *in vivo* cell based assays. The study of the RdRp/HeE1-2Tyr and RdRp/HeE1-2SO2 3D structures complexes helped us to better understand and explain the mechanism of inhibition of the molecules. In fact, the structures show that both compounds (although with poor electron density) interfere with the location of the RdRp priming loop (in agreement with the *in silico* predictions), which is disordered in the crystal structures. The fact that in

Flavivirus RdRps, and in particular in DENV RdRp, the priming loop has a clear density, suggests that it is well structured in the absence of RNA [70], supporting our hypothesis that HeE1-2SO2/HeE1-2Tyr inhibitory features could depend on the interference between the compounds and the priming loop. In this way the protein loses its capability to orient the nucleotide.

This study answers some of the biological questions posed by discovering NNIs that interact with the targeted protein in a strategic binding site (close to RNA exit channel) and host charged groups and rigid moieties. The improvement of the inhibitory properties presented by these molecules will require a reduction of the number of charged groups and of the molecular size.

In conclusion, the results achieved during my PhD project highlight the potential of structure-based rational drug design also for antiviral research; they will also be instrumental for the identification of new drug candidates able to interfere with essential steps of RdRp activity.

5. References

1. Clarke IN, Lambden PR (2000) Organization and expression of calicivirus genes. J Infect Dis 181 Suppl 2: S309-316.
2. McFadden N, Bailey D, Carrara G, Benson A, Chaudhry Y, et al. (2011) Norovirus regulation of the innate immune response and apoptosis occurs via the product of the alternative open reading frame 4. PLoS Pathog 7: e1002413.
3. Sosnovtsev SV, Belliot G, Chang KO, Prikhodko VG, Thackray LB, et al. (2006) Cleavage map and proteolytic processing of the murine norovirus nonstructural polyprotein in infected cells. J Virol 80: 7816-7831.
4. Hyde JL, Mackenzie JM (2010) Subcellular localization of the MNV-1 ORF1 proteins and their potential roles in the formation of the MNV-1 replication complex. Virology 406: 138-148.
5. Hyde JL, Sosnovtsev SV, Green KY, Wobus C, Virgin HW, et al. (2009) Mouse norovirus replication is associated with virus-induced vesicle clusters originating from membranes derived from the secretory pathway. J Virol 83: 9709-9719.
6. Firth AE, Brierley I (2012) Non-canonical translation in RNA viruses. J Gen Virol 93: 1385-1409.
7. Herbert TP, Brierley I, Brown TD (1997) Identification of a protein linked to the genomic and subgenomic mRNAs of feline calicivirus and its role in translation. J Gen Virol 78 (Pt 5): 1033-1040.
8. Simmonds P, Karakasiliotis I, Bailey D, Chaudhry Y, Evans DJ, et al. (2008) Bioinformatic and functional analysis of RNA secondary structure elements among different genera of human and animal caliciviruses. Nucleic Acids Res 36: 2530-2546.

9. Vashist S, Urena L, Chaudhry Y, Goodfellow I (2012) Identification of RNA-protein interaction networks involved in the norovirus life cycle. J Virol 86: 11977-11990.

10. Belliot G, Sosnovtsev SV, Chang KO, Babu V, Uche U, et al. (2005) Norovirus proteinase-polymerase and polymerase are both active forms of RNA-dependent RNA polymerase. J Virol 79: 2393-2403.

11. Belov GA, van Kuppeveld FJ (2012) (+)RNA viruses rewire cellular pathways to build replication organelles. Curr Opin Virol 2: 740-747.

12. Wobus CE, Karst SM, Thackray LB, Chang KO, Sosnovtsev SV, et al. (2004) Replication of Norovirus in cell culture reveals a tropism for dendritic cells and macrophages. PLoS Biol 2: e432.

13. Thorne L, Bailey D, Goodfellow I (2012) High-resolution functional profiling of the norovirus genome. J Virol 86: 11441-11456.

14. Hogbom M, Jager K, Robel I, Unge T, Rohayem J (2009) The active form of the norovirus RNA-dependent RNA polymerase is a homodimer with cooperative activity. J Gen Virol 90: 281-291.

15. Bull RA, Hyde J, Mackenzie JM, Hansman GS, Oka T, et al. (2011) Comparison of the replication properties of murine and human calicivirus RNA-dependent RNA polymerases. Virus Genes 42: 16-27.

16. Rohayem J, Robel I, Jager K, Scheffler U, Rudolph W (2006) Protein-primed and de novo initiation of RNA synthesis by norovirus 3Dpol. J Virol 80: 7060-7069.

17. Bertolotti-Ciarlet A, White LJ, Chen R, Prasad BV, Estes MK (2002) Structural requirements for the assembly of Norwalk virus-like particles. J Virol 76: 4044-4055.

18. Bruenn JA (2003) A structural and primary sequence comparison of the viral RNA-dependent RNA polymerases. Nucleic Acids Res 31: 1821-1829.

19. Ng KK, Pendas-Franco N, Rojo J, Boga JA, Machin A, et al. (2004) Crystal structure of norwalk virus polymerase reveals the carboxyl terminus in the active site cleft. J Biol Chem 279: 16638-16645.

20. Zamyatkin DF, Parra F, Alonso JM, Harki DA, Peterson BR, et al. (2008) Structural insights into mechanisms of catalysis and inhibition in Norwalk virus polymerase. J Biol Chem 283: 7705-7712.

21. Zamyatkin DF, Parra F, Machin A, Grochulski P, Ng KK (2009) Binding of 2'-amino-2'-deoxycytidine-5'-triphosphate to norovirus polymerase induces rearrangement of the active site. J Mol Biol 390: 10-16.

22. Lee JH, Alam I, Han KR, Cho S, Shin S, et al. (2011) Crystal structures of murine norovirus-1 RNA-dependent RNA polymerase. J Gen Virol 92: 1607-1616.

23. Kuhn RJ, Zhang W, Rossmann MG, Pletnev SV, Corver J, et al. (2002) Structure of dengue virus: Implications for flavivirus organization, maturation, and fusion. Cell 108: 717-725.

24. Billoir F, de Chesse R, Tolou H, de Micco P, Gould EA, et al. (2000) Phylogeny of the genus flavivirus using complete coding sequences of arthropod-borne viruses and viruses with no known vector. J Gen Virol 81 Pt 9: 2339.

25. Lindenbach BD, Rice CM (2003) Molecular biology of flaviviruses. Adv Virus Res 59: 23-61.

26. Morens DM, Fauci AS (2008) Dengue and hemorrhagic fever: a potential threat to public health in the United States. JAMA 299: 214-216.

27. Wilson JR, de Sessions PF, Leon MA, Scholle F (2008) West Nile virus nonstructural protein 1 inhibits TLR3 signal transduction. J Virol 82: 8262-8271.

28. Leung JY, Pijlman GP, Kondratieva N, Hyde J, Mackenzie JM, et al. (2008) Role of nonstructural protein NS2A in flavivirus assembly. J Virol 82: 4731-4741.

29. Umareddy I, Chao A, Sampath A, Gu F, Vasudevan SG (2006) Dengue virus NS4B interacts with NS3 and dissociates it from single-stranded RNA. J Gen Virol 87: 2605-2614.

30. Miorin L, Maiuri P, Hoenninger VM, Mandl CW, Marcello A (2008) Spatial and temporal organization of tick-borne encephalitis flavivirus replicated RNA in living cells. Virology 379: 64-77.

31. Koonin EV (1993) Computer-assisted identification of a putative methyltransferase domain in NS5 protein of flaviviruses and lambda 2 protein of reovirus. J Gen Virol 74 (Pt 4): 733-740.

32. Rice CM, Lenches EM, Eddy SR, Shin SJ, Sheets RL, et al. (1985) Nucleotide sequence of yellow fever virus: implications for flavivirus gene expression and evolution. Science 229: 726-733.

33. Poch O, Sauvaget I, Delarue M, Tordo N (1989) Identification of four conserved motifs among the RNA-dependent polymerase encoding elements. EMBO J 8: 3867-3874.

34. Koonin EV (1991) The phylogeny of RNA-dependent RNA polymerases of positive-strand RNA viruses. J Gen Virol 72 (Pt 9): 2197-2206.

35. Ollis DL, Kline C, Steitz TA (1985) Domain of E. coli DNA polymerase I showing sequence homology to T7 DNA polymerase. Nature 313: 818-819.

36. Delarue M, Poch O, Tordo N, Moras D, Argos P (1990) An attempt to unify the structure of polymerases. Protein Eng 3: 461-467.

37. Ago H, Adachi T, Yoshida A, Yamamoto M, Habuka N, et al. (1999) Crystal structure of the RNA-dependent RNA polymerase of hepatitis C virus. Structure 7: 1417-1426.

38. Bressanelli S, Tomei L, Roussel A, Incitti I, Vitale RL, et al. (1999) Crystal structure of the RNA-dependent RNA polymerase of hepatitis C virus. Proc Natl Acad Sci U S A 96: 13034-13039.

39. Lesburg CA, Cable MB, Ferrari E, Hong Z, Mannarino AF, et al. (1999) Crystal structure of the RNA-dependent RNA polymerase from hepatitis C virus reveals a fully encircled active site. Nat Struct Biol 6: 937-943.

40. Malet H, Egloff MP, Selisko B, Butcher RE, Wright PJ, et al. (2007) Crystal structure of the RNA polymerase domain of the West Nile virus non-structural protein 5. J Biol Chem 282: 10678-10689.

41. Ferrer-Orta C, Arias A, Escarmis C, Verdaguer N (2006) A comparison of viral RNA-dependent RNA polymerases. Curr Opin Struct Biol 16: 27-34.

42. Butcher SJ, Grimes JM, Makeyev EV, Bamford DH, Stuart DI (2001) A mechanism for initiating RNA-dependent RNA polymerization. Nature 410: 235-240.

43. Tao Y, Farsetta DL, Nibert ML, Harrison SC (2002) RNA synthesis in a cage--structural studies of reovirus polymerase lambda3. Cell 111: 733-745.

44. O'Farrell D, Trowbridge R, Rowlands D, Jager J (2003) Substrate complexes of hepatitis C virus RNA polymerase (HC-J4): structural evidence for nucleotide import and de-novo initiation. J Mol Biol 326: 1025-1035.

45. Malet H, Masse N, Selisko B, Romette JL, Alvarez K, et al. (2008) The flavivirus polymerase as a target for drug discovery. Antiviral Res 80: 23-35.

46. Gorbalenya AE, Pringle FM, Zeddam JL, Luke BT, Cameron CE, et al. (2002) The palm subdomain-based active site is internally permuted in viral RNA-dependent RNA polymerases of an ancient lineage. J Mol Biol 324: 47-62.

47. Ferrer-Orta C, Arias A, Perez-Luque R, Escarmis C, Domingo E, et al. (2004) Structure of foot-and-mouth disease virus RNA-dependent RNA polymerase and its complex with a template-primer RNA. J Biol Chem 279: 47212-47221.

48. Adachi T, Ago H, Habuka N, Okuda K, Komatsu M, et al. (2002) The essential role of C-terminal residues in regulating the activity of hepatitis C virus RNA-dependent RNA polymerase. Biochim Biophys Acta 1601: 38-48.

49. Leveque VJ, Johnson RB, Parsons S, Ren J, Xie C, et al. (2003) Identification of a C-terminal regulatory motif in hepatitis C virus RNA-dependent RNA polymerase: structural and biochemical analysis. J Virol 77: 9020-9028.

50. Choi KH, Groarke JM, Young DC, Kuhn RJ, Smith JL, et al. (2004) The structure of the RNA-dependent RNA polymerase from bovine viral diarrhea virus establishes the role of GTP in de novo initiation. Proc Natl Acad Sci U S A 101: 4425-4430.

51. Pryor MJ, Rawlinson SM, Butcher RE, Barton CL, Waterhouse TA, et al. (2007) Nuclear localization of dengue virus nonstructural protein 5 through its importin alpha/beta-recognized nuclear localization sequences is integral to viral infection. Traffic 8: 795-807.

52. Vasilakis N, Weaver SC (2008) The history and evolution of human dengue emergence. Adv Virus Res 72: 1-76.

53. Guzman MG, Kouri G (2008) Dengue haemorrhagic fever integral hypothesis: confirming observations, 1987-2007. Trans R Soc Trop Med Hyg 102: 522-523.

54. Ellis BR, Barrett AD (2008) The enigma of yellow fever in East Africa. Rev Med Virol 18: 331-346.

55. Widdowson MA, Monroe SS, Glass RI (2005) Are noroviruses emerging? Emerg Infect Dis 11: 735-737.

56. Koopmans M (2005) Food-borne norovirus outbreaks: a nuisance or more than that? Wien Klin Wochenschr 117: 789-791.

57. Koopmans M, Duizer E (2004) Foodborne viruses: an emerging problem. Int J Food Microbiol 90: 23-41.

58. Koopmans MP (2002) [Outbreaks of viral gastroenteritis, in particular due to the Norwalk virus: an underestimated problem]. Ned Tijdschr Geneeskd 146: 2401-2404.

59. Hennessy EP, Green AD, Connor MP, Darby R, MacDonald P (2003) Norwalk virus infection and disease is associated with ABO histo-blood group type. J Infect Dis 188: 176-177.

60. Hutson AM, Atmar RL, Graham DY, Estes MK (2002) Norwalk virus infection and disease is associated with ABO histo-blood group type. J Infect Dis 185: 1335-1337.

61. Lindesmith L, Moe C, Marionneau S, Ruvoen N, Jiang X, et al. (2003) Human susceptibility and resistance to Norwalk virus infection. Nat Med 9: 548-553.

62. Marionneau S, Ruvoen N, Le Moullac-Vaidye B, Clement M, Cailleau-Thomas A, et al. (2002) Norwalk virus binds to histo-blood group antigens present on gastroduodenal epithelial cells of secretor individuals. Gastroenterology 122: 1967-1977.

63. Rockx BH, Vennema H, Hoebe CJ, Duizer E, Koopmans MP (2005) Association of histo-blood group antigens and susceptibility to norovirus infections. J Infect Dis 191: 749-754.

64. De Francesco R, Carfi A (2007) Advances in the development of new therapeutic agents targeting the NS3-4A serine protease or the NS5B RNA-dependent RNA polymerase of the hepatitis C virus. Adv Drug Deliv Rev 59: 1242-1262.

65. Crotty S, Cameron CE, Andino R (2001) RNA virus error catastrophe: direct molecular test by using ribavirin. Proc Natl Acad Sci U S A 98: 6895-6900.

66. Pfeiffer JK, Kirkegaard K (2003) A single mutation in poliovirus RNA-dependent RNA polymerase confers resistance to mutagenic nucleotide analogs via increased fidelity. Proc Natl Acad Sci U S A 100: 7289-7294.

67. Yin Z, Chen YL, Schul W, Wang QY, Gu F, et al. (2009) An adenosine nucleoside inhibitor of dengue virus. Proc Natl Acad Sci U S A 106: 20435-20439.

68. Noble CG, Chen YL, Dong H, Gu F, Lim SP, et al. (2010) Strategies for development of Dengue virus inhibitors. Antiviral Res 85: 450-462.

69. De Clercq E (2005) Antiviral drug discovery and development: where chemistry meets with biomedicine. Antiviral Res 67: 56-75.

70. Noble CG, Shi PY (2012) Structural biology of dengue virus enzymes: towards rational design of therapeutics. Antiviral Res 96: 115-126.

71. Pilger BD, Cui C, Coen DM (2004) Identification of a small molecule that inhibits herpes simplex virus DNA Polymerase subunit interactions and viral replication. Chem Biol 11: 647-654.

72. Paeshuyse J, Leyssen P, Mabery E, Boddeker N, Vrancken R, et al. (2006) A novel, highly selective inhibitor of pestivirus replication that targets the viral RNA-dependent RNA polymerase. J Virol 80: 149-160.

73. Paeshuyse J, Chezal JM, Froeyen M, Leyssen P, Dutartre H, et al. (2007) The imidazopyrrolopyridine analogue AG110 is a novel, highly selective inhibitor of pestiviruses that targets the viral RNA-dependent RNA polymerase at a hot spot for inhibition of viral replication. J Virol 81: 11046-11053.

74. Mastrangelo E, Pezzullo M, Tarantino D, Petazzi R, Germani F, et al. (2012) Structure-based inhibition of Norovirus RNA-dependent RNA polymerases. J Mol Biol 419: 198-210.

75. Fullerton SW, Blaschke M, Coutard B, Gebhardt J, Gorbalenya A, et al. (2007) Structural and functional characterization of sapovirus RNA-dependent RNA polymerase. J Virol 81: 1858-1871.

76. Koch U, Narjes F (2006) Allosteric inhibition of the hepatitis C virus NS5B RNA dependent RNA polymerase. Infect Disord Drug Targets 6: 31-41.

77. Pfefferkorn JA, Greene ML, Nugent RA, Gross RJ, Mitchell MA, et al. (2005) Inhibitors of HCV NS5B polymerase. Part 1: Evaluation of

the southern region of (2Z)-2-(benzoylamino)-3-(5-phenyl-2-furyl)acrylic acid. Bioorg Med Chem Lett 15: 2481-2486.

78. Pfefferkorn JA, Nugent R, Gross RJ, Greene M, Mitchell MA, et al. (2005) Inhibitors of HCV NS5B polymerase. Part 2: Evaluation of the northern region of (2Z)-2-benzoylamino-3-(4-phenoxy-phenyl)-acrylic acid. Bioorg Med Chem Lett 15: 2812-2818.
79. Pinnen F, Cacciatore I, Cornacchia C, Sozio P, Iannitelli A, et al. (2007) Synthesis and study of L-dopa-glutathione codrugs as new anti-parkinson agents with free radical scavenging properties. Journal of Medicinal Chemistry 50: 2506-2515.
80. Bassissi F, Lespine A, Alvinerie M (2006) Assessment of a liposomal formulation of ivermectin in rabbit after a single subcutaneous administration. Parasitol Res 98: 244-249.
81. Allen TM, Newman MS, Woodle MC, Mayhew E, Uster PS (1995) Pharmacokinetics and anti-tumor activity of vincristine encapsulated in sterically stabilized liposomes. Int J Cancer 62: 199-204.
82. Kim S (1993) Liposomes as carriers of cancer chemotherapy. Current status and future prospects. Drugs 46: 618-638.
83. Bakker-Woudenberg IA, Lokerse AF, ten Kate MT, Melissen PM, van Vianen W, et al. (1993) Liposomes as carriers of antimicrobial agents or immunomodulatory agents in the treatment of infections. Eur J Clin Microbiol Infect Dis 12 Suppl 1: S61-67.
84. de Melo AL, Silva-Barcellos NM, Demicheli C, Frezard F (2003) Enhanced schistosomicidal efficacy of tartar emetic encapsulated in pegylated liposomes. Int J Pharm 255: 227-230.
85. Dvoroznakova E, Hrckova G, Boroskova Z, Velebny S, Dubinsky P (2004) Effect of treatment with free and liposomized albendazole on

selected immunological parameters and cyst growth in mice infected with Echinococcus multilocularis. Parasitol Int 53: 315-325.

86. Hrckova G, Velebny S, Corba J (1998) Effects of free and liposomized praziquantel on the surface morphology and motility of Mesocestoides vogae tetrathyridia (syn. M. corti; Cestoda: Cyclophyllidea) in vitro. Parasitol Res 84: 230-238.
87. Mourao SC, Costa PI, Salgado HR, Gremiao MP (2005) Improvement of antischistosomal activity of praziquantel by incorporation into phosphatidylcholine-containing liposomes. Int J Pharm 295: 157-162.
88. Rocha-Pereira J, Jochmans D, Dallmeier K, Leyssen P, Cunha R, et al. (2012) Inhibition of norovirus replication by the nucleoside analogue 2'-C-methylcytidine. Biochem Biophys Res Commun 427: 796-800.
89. Leslie, A. G.; Powell, H. R. (2007) Evolving methods for macromolecular crystallography; Springer 41–51.
90. Evans P (2006) Scaling and assessment of data quality. Acta Crystallogr D Biol Crystallogr 62: 72-82.
91. Vagin A, Teplyakov A (2010) Molecular replacement with MOLREP. Acta Crystallogr D Biol Crystallogr 66: 22-25.
92. Steiner RA, Lebedev AA, Murshudov GN (2003) Fisher's information in maximum-likelihood macromolecular crystallographic refinement. Acta Crystallogr D Biol Crystallogr 59: 2114-2124.
93. Smart OS, Womack TO, Flensburg C, Keller P, Paciorek W, et al. (2012) Exploiting structure similarity in refinement: automated NCS and target-structure restraints in BUSTER. Acta Crystallogr D Biol Crystallogr 68: 368-380.

94. Emsley P, Lohkamp B, Scott WG, Cowtan K (2010) Features and development of Coot. Acta Crystallogr D Biol Crystallogr 66: 486-501.

6. Acknowledgement

This work was funded by the FP7 HEALTH-2010 Collaborative Project SILVER (No. 260644). All the crystals were tested at ESRF in Grenoble (France) and ELETTRA in Trieste (Italy).

Thanks to Prof. Martino Bolognesi, Dr. Eloise Mastrangelo and Dr. Mario Milani for welcoming me into their group and giving me the opportunity to learn and get interested in research.

Thanks to Dr. Jacques Rohayem (CEO and Founder of Riboxx, Dresda, Germany) for the expression and purification of NV RdRps. Thanks to Dr. Marco Benati and Dr. Vittorio Pandini for the cell growth in fermentator and the usage of cell disruptor. Thanks to Prof. Reuben Hwu (National Central University, Jhongli, Taiwan) and Dr. Giuseppe Manfroni (University of Perugia, Perugia, Italy) for compound chemical modifications and synthesis. Thanks to Dr. Gill Querat (University of Marseille, Marseille, France) for *in vitro* cell-based assay. Thanks to Prof. Johan Neyts and Dr. Dirk Jochmans (KU Leuven, Leuven, Belgium) for the ospitality in their laboratories.

Thanks to Sara and Alessandra, whitout their advice I'd never have started this experience. A particular thank to Delia for her friendship and her help when I get discorauged, without her I would not have made it! Thanks to all other members of the lab for their help and carefree moments.

Thanks to Unimi friends Francesca, Graziano, Daniele and all my PhD collegues for their friendship and support. Thanks to my historic friends Laura, Bea & Ettore, Alice, Camilla, Ivon, Letizia, Elisa and Matteo G. to be always there, whatever happens. Thanks to Matteo for supporting and encouraging me in difficulties and for having enjoyed the happy moments.

Thanks to my parents ... they know why.

PART II

Antiviral Research 102 (2014) 23–28

Contents lists available at ScienceDirect

Antiviral Research

journal homepage: www.elsevier.com/locate/antiviral

Naphthalene-sulfonate inhibitors of human norovirus RNA-dependent RNA-polymerase

Delia Tarantino [a], Margherita Pezzullo [a,b], Eloise Mastrangelo [a,b], Romina Croci [a], Jacques Rohayem [c,d], Ivonne Robel [d], Martino Bolognesi [a], Mario Milani [a,b,*]

[a] Department of Biosciences and CIMAINA, University of Milano, Via Celoria 26, I-20133 Milano, Italy
[b] CNR-IBF, Istituto di Biofisica, Via Celoria 26, I-20133 Milano, Italy
[c] Institute of Virology, Dresden University of Technology, Fiedlerstrasse 42, 01307 Dresden, Germany
[d] Riboxx GmbH, Pharmapark Radebeul, Meissner Strasse 191, 01445 Radebeul, Germany

ARTICLE INFO

Article history:
Received 24 July 2013
Revised 31 October 2013
Accepted 28 November 2013
Available online 4 December 2013

Keywords:
Norovirus
Caliciviridae
RNA-dependent RNA polymerase
Antiviral discovery
X-ray crystallography
Naphthalene-sulfonate

ABSTRACT

Noroviruses are members of the *Caliciviridae* family of positive sense RNA viruses. In humans Noroviruses cause rapid onset diarrhea and vomiting. Currently Norovirus infection is responsible for 21 million gastroenteritis yearly cases in the USA. Nevertheless, despite the obvious public health and socio-economic relevance, no effective vaccines/antivirals are yet available to treat Norovirus infection.

Since the activity of RNA-dependent RNA polymerase (RdRp) plays a key role in genome replication and in the synthesis/amplification of subgenomic RNA, the enzyme is considered a promising target for antiviral drug development. In this context, following the identification of suramin and NF023 as Norovirus RdRp inhibitors, we analyzed the potential inhibitory role of naphthalene di-sulfonate (NAF2), a fragment derived from these two molecules. Although NAF2, tested in enzymatic polymerase inhibition assays, displayed low activity against RdRp (IC_{50} = 14 μM), the crystal structure of human Norovirus RdRp revealed a thumb domain NAF2 binding site that differs from that characterized for NF023/suramin. To further map the new potential inhibitory site, we focused on the structurally related molecule pyridoxal-5′-phosphate-6-(2′-naphthylazo-6′-nitro-4′,8′-disulfonate) tetrasodium salt (PPNDS). PPNDS displayed below-micromolar inhibitory activity *versus* human Norovirus RdRp (IC_{50} = 0.45 μM), similarly to suramin and NF023. Inspection of the crystal structure of the RdRp/PPNDS complex showed that the inhibitor bound to the NAF2 thumb domain site, highlighting the relevance of such new binding site for exploiting Norovirus RdRp inhibitors.

1. Introduction

Noroviruses (NVs) are members of the *Caliciviridae* family of positive sense RNA viruses (Fauquet and Fargette, 2005; Green, 2007; Green et al., 2000; Mayo, 2002). Norovirus-linked gastroenteritis is estimated to affect ~21 million people annually in the United States, being responsible for up to 200,000 deaths per year in developing countries (Patel et al., 2008). The disease is usually acute and self-limiting, but in immunocompromised adults it can become chronic and persist for weeks–years (Bok and Green, 2012).

The NV genome (7.7 kb) contains three open reading frames (ORF1-3) of single stranded RNA. ORF1 is translated into a large polyprotein precursor, cleaved into six non-structural proteins (NS1–2, NS3, NS4, NS5, NS6 and NS7) by the viral protease (NS6); ORF2 and ORF3 encode for the capsid proteins VP1 and VP2, respectively (Clarke and Lambden, 2000). The structural and non-structural viral proteins that orchestrate the viral replicative machinery are potentially vulnerable targets for "attack" by proper ligands interfering with their functionality (Rohayem et al., 2010). The virus-specific nature of such targets, and their indispensable functions, provide the potential for limiting negative side effects of antiviral drugs on the physiologic host-cell processes.

In this context, we formerly identified suramin and the analogous compound NF023 as human and murine NV NS7 RNA-dependent RNA-polymerase (hNV- and mNV-RdRp, respectively) inhibitors (Mastrangelo et al., 2012). Our crystallographic analyses

Abbreviations: hNV, human Norovirus; mNV, murine Norovirus; RdRp, RNA-dependent RNA-polymerase; PDB, protein data bank; NAF2, naphthalene-1,5-disulfonic acid; PPNDS, pyridoxal-5′-phosphate-6-(2′-naphthylazo-6′-nitro-4′,8′-disulfonate) tetrasodium salt.

* Corresponding author at: CNR-IBF, Department of Biosciences, University of Milano Via Celoria 26, 20133 Milano, Italy. Tel.: +39 02 50314898; fax: +39 02 50314895.
E-mail address: mario.milani@unimi.it (M. Milani).

0166-3542/$ - see front matter © 2013 Elsevier B.V. All rights reserved.
http://dx.doi.org/10.1016/j.antiviral.2013.11.016

showed that the two inhibitors bind in an extended conformation to a common site, close to the enzyme catalytic center. Suramin and derivatives display poor membrane permeability (Beindl et al., 1996; Charlton et al., 1996; Klinger et al., 2001) due to the negative charges of their sulfonate groups, and would require chemical optimization to improve their drug-likeness. On the other hand, the suramin/NF023 binding site is located along the access pathway of incoming nucleoside triphosphates (NTPs) and is lined, in its central region, with lysine and arginine residues endowed with highly mobile side chains. Such conformational flexibility of the targeted binding site adds substantial complexity to the structure-based inhibitor optimization process. On such bases, we set out to investigate a fragment of the two mentioned inhibitors that, according to our crystal structures, mapped to the less flexible region (i.e. inner in the enzyme active site) of the suramin/NF023 binding site, likely representing their most inhibitory-active portion. We thus focused on naphthalene-1,5-disulphonic acid (NAF2; Fig. 1a) as a fragment of both suramin and NF023 'inhibitory heads', applying a sort of reverse fragment screening approach.

NAF2 was initially tested in enzymatic assays for inhibition of hNV-RdRp, showing modest activity (IC_{50} = 14 μM). Unexpectedly, however, the crystal structure of the hNV-RdRp/NAF2 complex showed that, besides the site previously characterized in the suramin/NF023 complexes, the compound bound also to a new thumb domain site, located in a cleft along the newly synthesized RNA exit path. Accordingly, the two NAF2 binding sites identified were named A-site ('old' site, common with suramin/NF023) and B-site ('new' site). In order to further characterize the B-site in view of its exploitation for inhibitor design, we then selected the NAF2 analog pyridoxal-5′-phosphate-6-(2′-naphthylazo-6′-nitro-4′,8′-disulfonate) tetrasodium salt (PPNDS, Fig. 1b), which our previous docking searches showed to potentially map to a region close to the B-site (Mastrangelo et al., 2012). PPNDS proved able to inhibit hNV-RdRp activity with an IC_{50} value in the sub-micromolar range (IC_{50} = 0.45 μM). Moreover, the crystal structure of the hNV-RdRp/PPNDS complex showed that the inhibitor indeed bound to the B-site previously mapped by NAF2. Our findings highlight a new RdRp inhibitory sub-site, and suggest that structure-based optimization of PPNDS may provide analogs with enhanced drug-likeness, shedding new light on the path towards anti-Norovirus drugs.

2. Materials and methods

2.1. Chemicals

For the RdRp inhibition assays poly(C) and the NAF2 compound were purchased from Sigma–Aldrich, while PPNDS was from Santa Cruz Biotechnology. The compounds were dissolved at 100 mM in H_2O and stored at −20 °C.

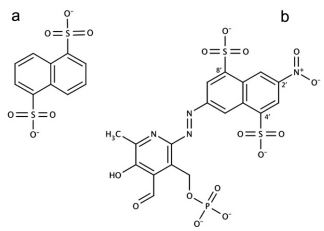

Fig. 1. Chemical structure of NAF2 (a) and PPNDS (b).

2.2. Expression and purification of the hNV-RdRp

hNV-RdRp was expressed in *Escherichia coli* and purified as previously described (Fullerton et al., 2007). The protein was dialyzed against buffer A (25 mM Tris/HCl, pH 7.4, 1 mM DTT, 100 mM NaCl, 1 mM EDTA) and concentrated to 9 mg/ml. Protein concentration was determined with the BCA Protein assay kit (Pierce) based on the Biuret reaction.

2.3. hNV-RdRp inhibition assays

In vitro RNA synthesis assays were performed as described (Mastrangelo et al., 2012). In brief the reaction mixture contained 20 mM Tris/HCl (pH 7.5), 1 mM DTT, 25 mM NaCl, 5 mM $MgCl_2$, 0.3 mM $MnCl_2$, 2 U RiboLock Ribonuclease inhibitor, PicoGreen Quantitation Reagent, and as substrates poly(C) template annealed with oligo$(G)_{12}$ primer (62.5 nM final concentration), and 100 μM GTP. Before starting the reaction, 1 μl of the protein was incubated for 5 min in the presence of 1 μl of water or 1 μl of one inhibitor solution at the required concentration. The reaction was started by the addition of the reaction mixture to the incubated protein (final protein concentration 255 nM; inhibitor concentration from 0 to 20 μM for NAF2, and from 0 to 10 μM for PPNDS) up to a total volume of 200 μl. The reactions were followed for 10 min at 30 °C recording (every 30 s) the fluorescence signals of the samples (in a Varian Cary Eclipse Fluorescence Spectrophotometer) arising from the interaction of the PicoGreen dye with the growing dsRNA. Protein activity was evaluated subtracting the slope of the linearly growing fluorescence from that of the same reaction mix win the absence of the enzyme. The results of three independent experiments were averaged. A plot of activity *versus* inhibitor concentration was used to estimate the IC_{50} values for each inhibitor (Table 1; Fig. S1) using the program GraFit (Erithacus software) or QtiPlot, using the four parameter equation:

$$A = m + (M - m)\frac{1}{1 + \left(\frac{[I]}{IC_{50}}\right)^{n}}$$

where A = activity, M = maximum activity, m = minimum activity, $[I]$=inhibitor concentration, n = Hill coefficient (Prinz, 2010).

Independently, kinetic experiments were performed in order to determine the PPNDS hNV RdRp inhibition mechanism relative to the poly(C)/oligo$(G)_{12}$ substrate. Briefly, to explore the inhibition mode, we performed standard enzymatic reactions for which the poly(C)/oligo$(G)_{12}$ concentration was varied (from 3.9 to 125 nM), at 100 μM GTP constant concentration, applying increasing amounts of the inhibitor (from 0 to 1 μM). The assays were performed using a TECAN Infinite 200 PRO microplate reader; the results were analyzed through Lineweaver–Burk plots ($1/V$ *versus* $1/[S]$) at varying PPNDS concentrations.

2.4. Biophysical characterization of the hNV-RdRp/inhibitor interaction

Thermofluorimetric (Thermal shift) assays for the evaluation of the hNV-RdRp melting temperature (T_m) in the absence/presence of the inhibitors were conducted in a MiniOpticon Real Time PCR Detection System (Bio-Rad), using the fluorescent dye Sypro Orange. 4 μl aliquots of hNV-RdRp solution (final protein concentra-

Table 1
IC_{50} values of the different compounds against hNV-RdRp.

Cpd	hNV-RdRp IC_{50} (μM)
Suramin	0.24 ± 0.08
NAF2	14.0 ± 1.0
PPNDS	0.45 ± 0.09

tion 34.7 μM) were diluted in 18 μl of its buffer, and mixed with 3.5 μl of Sypro orange (Sigma) diluted 60×, and PPNDS (5 or 50 μM), or 700 μM NAF2. In control samples the inhibitor solutions were replaced by water. The sample plates were heated from 20 to 90 °C, with a heating rate of 0.2 °C/min. Fluorescence intensities were measured within excitation/emission ranges of 470–505 nm and 540–700 nm, respectively.

2.5. Crystallization of the hNV-RdRp in presence of NAF2 and PPNDS

Sitting drop crystallization experiments for hNV-RdRp (11 mg/ml stock enzyme concentration) were assembled using an Oryx-8 crystallization robot (Douglas Instruments, East Garston, UK), from a 50%, 67%, 80% mixture of the protein with the reservoir solution (final drop volume 0.3 μl). Crystals grew in about 4 weeks, at 20 °C, in 1.2 M Na citrate, 100 mM Na cacodylate, pH 6.2, NaCl 125 mM. Before X-ray data collection, crystals were soaked in a cryoprotectant solution (1.4 M Na citrate, 100 mM Na cacodylate pH 6.2, and 25% glycerol) containing 30 mM NAF2, for 24 h, or containing 5 mM of PPNDS, 62.5 nM dsRNA (poly(C)/oligo$(G)_{12}$) and 100 μM GTP, for 36 h. The soaked crystals were then flash-cooled in liquid nitrogen. The hNV-RdRp/NAF2 crystals diffracted to a maximum resolution of 2.04 Å at the Elettra Synchrotron source (Trieste, Italy), beam line XRD1. The hNV-RdRp/PPNDS crystals diffracted to a maximum resolution of 2.6 Å at the ESRF Synchrotron facility (Grenoble, France), beam line ID29.

hNV-RdRp/NAF2 X-ray diffraction data were indexed using MOSFLM (Read et al., 2007), and intensities were merged using SCALA (Evans, 2006). hNV-RdRp/PPNDS X-ray diffraction data were indexed and scaled using XDS (Kabsch, 2010). The hNV-RdRp crystals grown in the presence both of NAF2 or PPNDS display closely similar unit cells and belong to the orthorhombic space group *I222*; data collection statistics are reported in Table 2.

Table 2
X-ray data-collection and refinement statistics for hNV-RdRp/NAF2 and for hNV-RdRp/PPNDS.

Protein	hNV-RdRp/NAF2	hNV-RdRp/PPNDS
Soaked compound	NAF2, 30 mM	PPNDS, 5 mM
Ligand site(s) present	A-site, B-site	B-site
Beam line & wavelength (Å)	ELETTRA XRD1 1.000	ESRF ID29 1.072
Space group	I222	I222
Unit-cell parameters (Å)	a = 86.6; b = 111.8; c = 121.4	a = 85.8; b = 116.1; c = 122.1
Molecules in a.u.	1	1
Resolution (Å)	45.4–2.04	38.4–2.6
Mosaicity (°)	0.6	0.4
Measured reflections	138,897 (20,166)[a]	87,361 (6,478)[c]
Unique reflections	37,405 (5,330)	19,046 (1,383)
Completeness (%)	98.7 (97.7)	99.6 (99.7)
Redundancy	3.7 (3.8)	4.6 (4.7)
R_{merge}[a] (%)	10.3 (41.7)	10.4 (73.8)
Average I/σ (I)	9.1 (2.7)	12.1 (1.9)
R_{factor}[b]/R free[c] (%)	17.0/22.3	22.0/28.5
r.m.s. Bonds (Å)	0.010	0.008
r.m.s. Angles (°)	1.37	1.18
Average protein B fac. (Å^2)	22.4	57.5
Average ligand B fac. (Å^2)	B-site = 20.9 A-site = 32.2	B-site = 85.2
Residues in most favored regions (%)	93.4	91.8
Residues in additionally allowed regions (%)	6.6	8.2
PDB-ID	4LQ9	4LQ3

Values in parentheses are for the highest resolution shell: [a](2.15–2.04); [b](2.66–2.60).

[a] $R_{merge} = \Sigma|I-\langle I\rangle|/\Sigma I \times 100$, where I is intensity of a reflection and $\langle I\rangle$ is its average intensity.

[b] $R_{factor} = \Sigma||F_o|-|F_c||/\Sigma|F_o| \times 100$.

[c] R_{free} is calculated on 5% randomly selected reflections, for cross-validation.

2.6. Structure determination and refinement

The three-dimensional structures of hNV-RdRp in the complexes with NAF2 and PPNDS were solved by the Molecular Replacement method using the program MOLREP (Vagin and Teplyakov, 1997) and a search model based on the structure of the hNV-RdRp from strain Hu/NLV/Dresden174/1997/GE (PDB-id 2B43). The single molecule present in the crystal asymmetric unit was subjected to rigid-body refinement, and subsequently to constrained refined using REFMAC5 (Steiner et al., 2003). A random set comprising 5% of the data was omitted from refinement for R-free calculation. Manual rebuilding with COOT (Emsley et al., 2010); additional refinement with BUSTER (Smart et al., 2012) and REFMAC5, were subsequently performed, as needed. Refinement statistics as well as stereochemical quality assessment of the 3D structures are summarized in Table 2. Atomic coordinates and structure factors for hNV-RdRp in complex with NAF2 and PPNDS have been deposited with the PDB (Berman et al., 2000) with accession codes 4LQ9 and 4LQ3, respectively.

3. Results

3.1. In vitro inhibition of hNV-RdRp

In vitro RNA synthesis assays were performed using annealed poly(C)–oligo$(G)_{12}$ (62.5 nM final concentration) and GTP (100 μM final concentration), as polymerase substrates, and 255 nM RdRp, following procedures previously described (Mastrangelo et al., 2012). Under these experimental conditions, NAF2 inhibited hNV-RdRp activity with IC_{50} = 14 μM whereas PPNDS inhibited the enzyme with an IC_{50} value of about 0.45 μM (Table 1; Fig. S1). Furthermore, analyzing the dose–response curves for NAF2, it is evident that the number of bound inhibitor molecules is higher than 1 (Prinz, 2010). As described in the next paragraph, such value is in agreement with the crystal structure data, where we observed two ligand binding sites (see below).

We also analyzed the kinetic mechanism of hNV-RdRp inhibition by PPNDS (Fig. 2). The Lineweaver–Burk plots highlighted a non-competitive inhibition mechanism with respect to the poly(C)/oligo$(G)_{12}$ substrate, with a *Ki* value of 0.52 ± 0.05 μM, indicating that the inhibitor is able to bind to the free enzyme as well as to the enzyme–substrate complex.

In order to verify whether the selected compounds might induce some form of destabilization/denaturation of the enzyme, generally reflected by a variation of the protein T_m, we performed thermofluorimetric assays. The acquired data showed that hNV-RdRp displays the same T_m in the absence (T_m = 36.9 ± 0.5 °C) or in the presence of NAF2 (0.7 mM; T_m = 37.5 ± 0.4 °C). The thermofluorimetric signal recorded in the presence of PPNDS is markedly reduced when the inhibitor concentration is raised, since the red colored inhibitor molecule absorbs part of the incident radiation (in the 470–505 nm range). We were however able to test the effects on T_m at two PPNDS concentrations (5 and 50 μM), resulting in T_m values of 37.0 ± 0.5 and 41.0 ± 2.0, respectively (Fig. S2a and b). Despite the low fluorescence signal recorded in the presence of 50 μM PPNDS, the slight Tm increase observed would imply some protein stabilization induced by the bound inhibitor. All the thermofluorimetric results prove that the hNV-RdRp inhibition is not due to inhibitor-linked adverse effects on enzyme stability/denaturation.

3.2. Crystal structures of hNV-RdRp with NAF2

3.2.1. Inhibitor binding to the B-site

The analysis of NAF2 binding to the RdRp domain was addressed through X-ray crystallography. To this purpose,

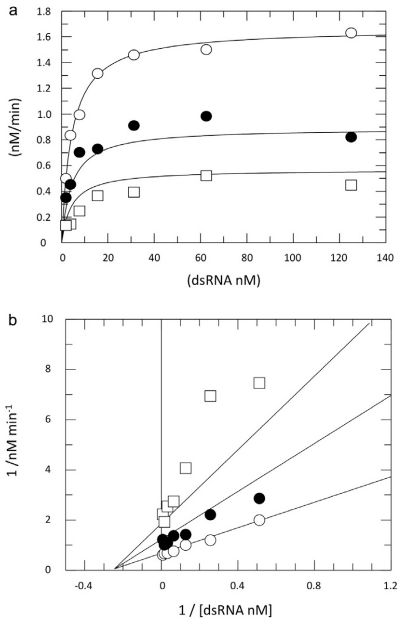

Fig. 2. (a) Reaction velocity plot as a function of the RNA concentration, ○ in absence of the inhibitor, ● in presence of 0.45 μM of PPNDS and □ in presence of 1 μM of PPNDS. (b) Lineweaver–Burk double reciprocal plot for the non competitive inhibition mechanism of hNV RdRp activity by PPNDS, relative to RNA substrate.

hNV-RdRp crystallization experiments were performed in presence of NAF2 (see Section 2for details). The hNV-RdRp crystals were soaked in 30 mM NAF2 before cryo-cooling, The crystal (belonging to the orthorhombic space group *I222*, with one molecule per asymmetric unit) diffracted to a maximum resolution of 2.04 Å, and the structure was refined to a final crystallographic R-factor of 17.0% and R-free of 22.3% (Table 2). The first refinement cycles showed residual electron density compatible with a NAF2 molecule located in a positively charged cleft within the thumb domain (Fig. 3a and b), built by an α-β-loop-α motif; inspection of the enzyme structure confirms that this site (hereafter, the B-site) is different from the binding site where suramin and NF023 inhibitors were located (hereafter, the A-site). In the B-site, the negative charges of NAF2 sulfonates are balanced by Arg419 and Arg436; the naphthalene ring is sandwiched between Gln414 and Gln439 (forming an intertwined hydrogen bond network together with Asn505), on one side, and Phe28 and Arg419, on the other (Fig. 3b). Additional polar interactions involve the side chains of Asn505 and Thr418 and the main chain nitrogen of Arg419. Inspection of the hNV-RdRp/NAF2 crystal structure in comparison to the enzyme 3D structure in the absence of inhibitors (pdb-id: 2B43, r.m.s.d. 0.70 Å, over 499 Cα pairs) shows that, upon NAF2 binding, the protein undergoes only slight structural rearrangements at a few residues, and at the last two C-terminal residues, Asn505 and Glu506, visible in the electron density.

3.2.2. Inhibitor binding to the A-site

Further inspection of difference Fourier maps revealed residual electron density compatible with one NAF2 molecule in the A-site (Fig. 3a and c), i.e. at a location very close to the site occupied by the naphthalene-sulfonate moiety of NF023/suramin, in the fingers domain (Fig. 3c; Mastrangelo et al., 2012). Lys171, Lys174, Lys180 and Arg182 stabilize the inhibitor negative charges; the sulfonate groups establish H-bonds with Gln66 and the main chain N atom of Lys171. Additionally, the naphthalene ring makes π-cation interactions with Lys174 and Arg182 (Fig. 3c).

3.3. Crystal structure of hNV-RdRp bound to PPNDS

In a previous virtual screening search targeting a wide region around the hNV-RdRp active site, we identified PPNDS, a compound hosting a naphthalene disulfonate moiety, among other potential NV-RdRp inhibitors (Mastrangelo et al. 2012). Analysis of the simulated structure showed that PPNDS would locate in a

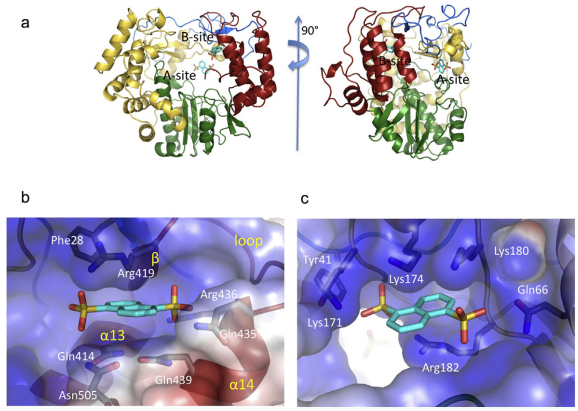

Fig. 3. (a) Crystal structure of hNV-RdRp bound to two NAF2 molecules in the A-site and B-site; the overall structure of hNV-RdRp in cartoon: N-terminal domain (blue), thumb (red), fingers (yellow) and palm (green). The picture on the right is rotated by 90 degree around the vertical axis. (b and c) Details of the hNV-RdRp/NAF2 interaction in the B-site (b) and A-site (c); transparent surface colored by electrostatic potential (program APBS2; (Baker et al., 2001)); amino acids involved in the interaction with NAF2 are labeled. Figures created using PyMol (http://www.pymol.org). (For interpretation of the references to color in this figure legend, the reader is referred to the web version of this article.)

region close to the B-site described above. Therefore, for the present study, PPNDS was selected as a commercially available compound potentially useful to further characterize structural features of the newly identified B-site. Notably, we succeeded in obtaining crystals of hNV-RdRp bound to PPNDS only after soaking the protein with the inhibitor in the presence of dsRNA and GTP (see Section 2.5 for details). This suggests that inhibitor binding to the protein requires local structural changes related to events in the catalytic cycle. The protein crystal structure was refined to a final crystallographic *R*-factor of 22.0%, and *R*-free of 28.5%, for the 2.6 Å resolution data set (Table 2). As predicted by the docking study, PPNDS binds only to the B-site (Fig. 4, Fig. S3a and b). The overall structure of the whole enzyme bound to PPNDS appears slightly more compact relative to that of the inhibitor-free protein (pdb-id 1SH0; r.m.s.d. 1.01 Å, over 484 Cα pairs (Ng et al., 2004)). Such overall effect is related to a small displacement of both the fingers and the thumb domains toward the active site, as in a closing hand, and is likely due to the interaction of the protein with dsRNA (Fig. 4a and b). In fact, the crystal structure shows residual electron density hosted between the fingers and thumb domains compatible with two or three RNA nucleotides, which have been only partially modeled in the refined structure, due to electron density ambiguities. The nucleotides are hosted in a positively charged region along the exit pathway of the newly formed RNA chain (Zamyatkin et al., 2008).

The PPNDS molecule can be schematically divided into two moieties, the naphthalene 6′-nitro-4′,8′-disulfonate and the pyridoxal-5′-phosphate, linked by the azo bond (Fig. 1b). The nitro group of the first moiety is tightly hosted in a hydrophobic cleft, between helices α13 and α14 of the thumb domain, lined with Leu406, Ile411 (α13), Leu443 (α14), Val504 (C-terminal) and with the aliphatic portion of the side chains of Ser 410 (α13), Gln414 (α13) and Glu446 (α14) (Fig. 4c, Fig. S3b). Both PPNDS sulfonate groups point toward the solvent; the 8′ sulfonate establishes hydrogen bonds with Gln414 and Gln439, while the 4′ sulfonate is H-bonded to Ser410 and salt bridges with Arg413 and Arg392 (Fig. 4c). The naphthalene ring is in van der Waals contacts with Gln414. The PPNDS pyridoxal-5′-phosphate group is elongated toward the fingers domain, stabilizing the conformation of the C-ter end of hNV-RdRp within the active site cavity (Fig. 4a and c). In fact, while in the inhibitor-free enzyme the C-ter is modeled in the electron density up to Glu506–Asp507, when PPNDS is present all the C-ter residues can be modeled (Glu510 is in van der Waals contact with the pyridoxal moiety, and H-bonded to its phosphate group). Interestingly, the PPNDS phosphate group points toward the active site region in the palm domain, which is rich in negatively charged amino acids, partially masked by Arg182, Arg392 and Mg^{2+}. Finally, the carbonyl group of the pyridoxal ring is H-bonded to Glu168. Relative to NAF2, the PPNDS molecule appears to be shifted toward the palm domain of about two α helical turns (~6–7 Å) along the direction of the antiparallel helices α13 and α14. Such PPNDS location may be dictated by the nitro group that cannot be properly hosted in the NAF2 cavity due to clash with Trp417 main chain (in the α13-β motif of the thumb domain). Notably, the location of PPNDS at a site different from the previously identified A-site is independently assessed by the close matching of the IC_{50} values obtained (as described above) for w.t. hNV-RdRp (Table 1) and for its Y41A mutant, where a key residue building the A-site is replaced by Ala (IC_{50} of about 500 ± 50 nM). In fact, such a mutation was previously shown to affect suramin and NF023 inhibitory effects on hNV-RdRp (Mastrangelo et al., 2012).

4. Discussion

In a previous work (Mastrangelo et al., 2012) we showed that suramin and NF023 binding site to mNV-RdRp, and to hNV-RdRp, as inferred by crystal structures and mutation analysis, is located along the access pathway of NTPs to the enzyme active center. Accordingly, such site is lined with positively charged residues whose conformational flexibility helps promoting the diffusion of NTPs toward the catalytic site. Such structural features are unlikely to make this inhibitor binding site an ideal target region for structure based drug optimization. We therefore decided to analyze the structural and inhibitory properties of fragments of the

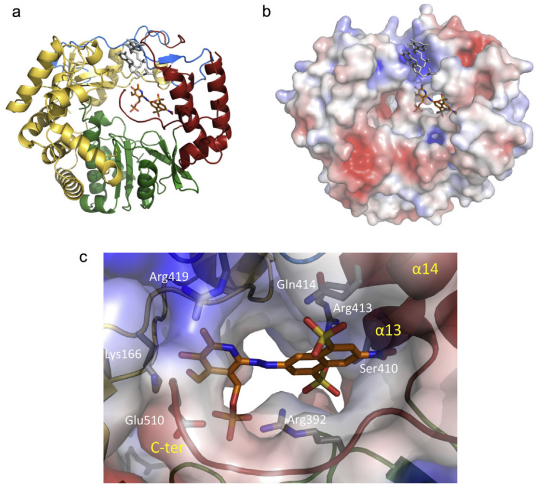

Fig. 4. (a) Crystal structure of hNV-RdRp bound to PPNDS in cartoon. PPNDS (orange carbon atoms) and a fragment of ssRNA, partially modeled into observed electron density (gray) are shown as sticks. (b) Same as (a) with protein surface colored by electrostatic potential. (c) Details of the local contacts between PPNDS and hNV-RdRp; amino acids involved in the interaction with PPNDS are labeled. (For interpretation of the references to color in this figure legend, the reader is referred to the web version of this article.)

identified inhibitors, focusing on their naphthalene-sulfonate moieties, thus selecting the NAF2 compound. Enzymatic assays showed that the selected fragment of the initial inhibitors still retains marginal inhibitory activity. More importantly, besides the site previously characterized in the suramin/NF023 complexes (here identified as the A-site), such reverse fragment screening experiments unraveled a novel, unexpected, binding site for NAF2, located in the RdRp thumb domain (B-site). Interestingly, the B-site is located in a position that is roughly structurally equivalent to the benzothiadiazine inhibitor binding site in the Hepatitis C Virus RdRp (Koch and Narjes, 2006; Pfefferkorn et al., 2005). NAF2 binding to two distinct sites is also suggested by analysis of the inhibition mechanism which shows a Hill coefficient higher than 1. In order to further characterize the B-site we selected PPNDS, a naphthalene sulfonate-based compound that is a potent and selective P2X1 receptor antagonist (Lambrecht et al., 2000). We demonstrated that PPNDS is able to inhibit the polymerase activity (Hill coefficient ~1, Fig. S1b) with a potency close to that observed for suramin or NF023. The crystal structure of the hNV-RdRp/PPNDS complex shows that the compound is anchored to the protein mostly through its naphthalene moiety. On the other hand, the improved inhibitory efficacy is likely dependent on PPNDS pyridoxal moiety that extends toward the enzyme active site. Such consideration is in keeping with the fact that: (i) NAF2 does not exert considerable inhibition, and (ii) PPNDS helps fixing the C-terminal end of the enzyme inside the active site, likely blocking the access of both the ssRNA template and the NTPs. The discovery of a new inhibitor binding site, and our analysis of the PPNDS binding mode to hNV-RdRp, provide new structural bases for modification of PPNDS and/or related compounds, in order to improve its efficacy and drug-likeness.

Acknowledgment

This work was funded by the FP7 HEALTH-2010 Collaborative Project SILVER (No. 260644).

Appendix A. Supplementary data

Supplementary data associated with this article can be found, in the online version, at http://dx.doi.org/10.1016/j.antiviral.2013.11.016.

References

Baker, N.A., Sept, D., Joseph, S., Holst, M.J., McCammon, J.A., 2001. Electrostatics of nanosystems: application to microtubules and the ribosome. Proc. Natl. Acad. Sci. USA 98, 10037–10041.

Beindl, W., Mitterauer, T., Hohenegger, M., Ijzerman, A.P., Nanoff, C., Freissmuth, M., 1996. Inhibition of receptor/G protein coupling by suramin analogues. Mol. Pharmacol. 50, 415–423.

Berman, H.M., Westbrook, J., Feng, Z., Gilliland, G., Bhat, T.N., Weissig, H., Shindyalov, I.N., Bourne, P.E., 2000. The protein data bank. Nucleic Acids Res. 28, 235–242.

Bok, K., Green, K.Y., 2012. Norovirus gastroenteritis in immunocompromised patients. N. Engl. J. Med. 367, 2126–2132.

Charlton, S.J., Brown, C.A., Weisman, G.A., Turner, J.T., Erb, L., Boarder, M.R., 1996. PPADS and suramin as antagonists at cloned P2Y- and P2U-purinoceptors. Br. J. Pharmacol. 118, 704–710.

Clarke, I.N., Lambden, P.R., 2000. Organization and expression of calicivirus genes. J. Infect. Dis. 181 (Suppl. 2), S309–316.

Emsley, P., Lohkamp, B., Scott, W.G., Cowtan, K., 2010. Features and development of Coot. Acta Crystallogr. Sect. D 66, 486–501.

Evans, P., 2006. Scaling and assessment of data quality. Acta Crystallogr. D: Biol. Crystallogr. 62, 72–82.

Fauquet, C.M., Fargette, D., 2005. International committee on taxonomy of viruses and the 3,142 unassigned species. Virol. J. 2, 64.

Fullerton, S.W., Blaschke, M., Coutard, B., Gebhardt, J., Gorbalenya, A., Canard, B., Tucker, P.A., Rohayem, J., 2007. Structural and functional characterization of sapovirus RNA-dependent RNA polymerase. J. Virol. 81, 1858–1871.

Green, K.Y., 2007. Caliciviridae: the noroviruses. In: Knipe, D.M., Howley, P.M. (Eds.), fifth 144 ed. Fields Virology, vol. 1. Lippincott Williams & Wilkins, a 145 Wolters Kluwer Business, Philadelphia, USA, pp. 41–51.

Green, K.Y., Ando, T., Balayan, M.S., Berke, T., Clarke, I.N., Estes, M.K., Matson, D.O., Nakata, S., Neill, J.D., Studdert, M.J., Thiel, H.J., 2000. Taxonomy of the *caliciviruses*. J. Infect. Dis. 181 (Suppl. 2), S322–330.

Kabsch, W., 2010. Xds. Acta Crystallogr. D: Biol. Crystallogr. 66, 125–132.

Klinger, M., Bofill-Cardona, E., Mayer, B., Nanoff, C., Freissmuth, M., Hohenegger, M., 2001. Suramin and the suramin analogue NF307 discriminate among calmodulin-binding sites. Biochem. J. 355, 827–833.

Koch, U., Narjes, F., 2006. Allosteric inhibition of the hepatitis C virus NS5B RNA dependent RNA polymerase. Infect. Disord. Drug Targets 6, 31–41.

Lambrecht, G., Rettinger, J., Baumert, H.G., Czeche, S., Damer, S., Ganso, M., Hildebrandt, C., Niebel, B., Spatz-Kumbel, G., Schmalzing, G., Mutschler, E., 2000. The novel pyridoxal-5′-phosphate derivative PPNDS potently antagonizes activation of P2X(1) receptors. Eur. J. Pharmacol. 387, R19–21.

Mastrangelo, E., Pezzullo, M., Tarantino, D., Petazzi, R., Germani, F., Kramer, D., Robel, I., Rohayem, J., Bolognesi, M., Milani, M., 2012. Structure-based inhibition of Norovirus RNA-dependent RNA polymerases. J. Mol. Biol. 419, 198–210.

Mayo, M.A., 2002. A summary of taxonomic changes recently approved by ICTV. Arch. Virol. 147, 1655–1663.

Ng, K.K., Pendas-Franco, N., Rojo, J., Boga, J.A., Machin, A., Alonso, J.M., Parra, F., 2004. Crystal structure of norwalk virus polymerase reveals the carboxyl terminus in the active site cleft. J. Biol. Chem. 279, 16638–16645.

Patel, M.M., Widdowson, M.A., Glass, R.I., Akazawa, K., Vinje, J., Parashar, U.D., 2008. Systematic literature review of role of noroviruses in sporadic gastroenteritis. Emerg. Infect. Dis. 14, 1224–1231.

Pfefferkorn, J.A., Greene, M.L., Nugent, R.A., Gross, R.J., Mitchell, M.A., Finzel, B.C., Harris, M.S., Wells, P.A., Shelly, J.A., Anstadt, R.A., Kilkuskie, R.E., Kopta, L.A., Schwende, F.J., 2005. Inhibitors of HCV NS5B polymerase. Part 1: Evaluation of the southern region of (2Z)-2-(benzoylamino)-3-(5-phenyl-2-furyl)acrylic acid. Bioorg. Med. Chem. Lett. 15, 2481–2486.

Prinz, H., 2010. Hill coefficients, dose–response curves and allosteric mechanisms. J. Chem. Biol. 3, 37–44.

Read, R., Sussman, J., Leslie, A.W., Powell, H., 2007. Processing Diffraction Data with Mosflm, Evolving Methods for Macromolecular Crystallography. Springer, Netherlands, pp. 41–51.

Rohayem, J., Bergmann, M., Gebhardt, J., Gould, E., Tucker, P., Mattevi, A., Unge, T., Hilgenfeld, R., Neyts, J., 2010. Antiviral strategies to control calicivirus infections. Antiviral Res. 87, 162–178.

Smart, O.S., Womack, T.O., Flensburg, C., Keller, P., Paciorek, W., Sharff, A., Vonrhein, C., Bricogne, G., 2012. Exploiting structure similarity in refinement: automated NCS and target-structure restraints in BUSTER. Acta Crystallogr. Sect. D 68, 368–380.

Steiner, R.A., Lebedev, A.A., Murshudov, G.N., 2003. Fisher's information in maximum-likelihood macromolecular crystallographic refinement. Acta Crystallogr. Sect. D 59, 2114–2124.

Vagin, A., Teplyakov, A., 1997. MOLREP: an automated program for molecular replacement. J. Appl. Crystallogr. 30, 1022–1025.

Zamyatkin, D.F., Parra, F., Alonso, J.M., Harki, D.A., Peterson, B.R., Grochulski, P., Ng, K.K., 2008. Structural insights into mechanisms of catalysis and inhibition in Norwalk virus polymerase. J. Biol. Chem. 283, 7705–7712.

FEBS Letters 588 (2014) 1720–1725

FEBS Letters

journal homepage: www.FEBSLetters.org

PPNDS inhibits murine Norovirus RNA-dependent RNA-polymerase mimicking two RNA stacking bases

Romina Croci [a,1], Delia Tarantino [a,1], Mario Milani [a,b], Margherita Pezzullo [a,b], Jacques Rohayem [c,d], Martino Bolognesi [a], Eloise Mastrangelo [a,b,*]

[a] Department of Biosciences, University of Milano, Via Celoria 26, I-20133 Milano, Italy
[b] CNR-IBF, Istituto di Biofisica, Via Celoria 26, I-20133 Milano, Italy
[c] Institute of Virology, Dresden University of Technology, Fiedlerstrasse 42, 01307 Dresden, Germany
[d] Riboxx GmbH, Pharmapark Radebeul, Meissner Strasse 191, 01445 Radebeul, Germany

ARTICLE INFO

Article history:
Received 19 December 2013
Revised 27 February 2014
Accepted 10 March 2014
Available online 18 March 2014

Edited by Christian Griesinger

Keywords:
Norovirus
RNA-dependent-RNA-polymerase
Antiviral discovery
In silico-docking
X-ray crystallography
PPNDS

ABSTRACT

Norovirus (NV) is a major cause of gastroenteritis worldwide. Antivirals against such important pathogens are on demand. Among the viral proteins that orchestrate viral replication, RNA-dependent-RNA-polymerase (RdRp) is a promising drug development target. From an in silico-docking search focused on the RdRp active site, we selected the compound PPNDS, which showed low micromolar IC_{50} *vs.* murine NV-RdRp in vitro. We report the crystal structure of the murine NV-RdRp/PPNDS complex showing that two molecules of the inhibitor bind in antiparallel stacking interaction, properly oriented to block exit of the newly synthesized RNA. Such inhibitor-binding mode mimics two stacked nucleotide-bases of the RdRp/ssRNA complex.

1. Introduction

The *Caliciviridae* family includes human and non-human pathogens, clustering so far in four accepted genera: Norovirus (NV), Sapovirus (SV), Lagovirus and Vesivirus [1–4]. Such viruses cause a broad spectrum of diseases, which may range from acute gastroenteritis in humans (NV and SV) to hemorrhagic disease in rabbits (rabbit hemorrhagic disease virus) and upper airway infection in cats (feline calicivirus) to lethal encephalitis in immune-deficient mice (caused by murine Norovirus, mNV) [5,6]. Currently no vaccines or specific antiviral agents are available to combat these pathogens, with the exception of a vaccine for feline NV [7]. Thus there is an urgent need for the discovery of broad-spectrum therapeutics for treating their related infections [8].

mNV is closely related to human NV (hNV), but contrary to hNV, it grows in culture and in a small animal model, thus providing a tractable model to study NV biology [9]. There are at least six NV genotypes, parts of which comprise subgenotypes; mNV belongs to genotype V. Thus, should an inhibitor prove active against mNV in cell cultures, it would likely be active also against hNV of various genotypes.

The NV genome, composed of 7.3–8.5 kb nucleotides, is organized in three open reading frames (ORF-1 to ORF-3). An additional ORF, ORF4, was discovered in the mNV genome in an alternative reading frame overlapping the VP1 coding region [10,11]. ORF1 is translated into a large polyprotein precursor cleaved, by the viral 3C-like proteases [12–14] into six non-structural proteins, among which the non-structural protein 7 (NS7) is endowed with RNA-dependent-RNA-polymerase (RdRp) activity [15]. Since human cells lack RdRps, this viral class of enzymes appears as one of the most promising targets for development of antivirals. In our previous work, through an in silico-docking search based on a virtual library of commercially available molecules, we identified and characterized suramin and the analogous compound NF023 as NV-RdRp inhibitors [16]. Since these two molecules display poor membrane

Abbreviations: hNV, human Norovirus; mNV, murine Norovirus; RdRp, RNA-dependent-RNA-polymerase; PDB, Protein Data Bank; PPNDS, Pyridoxal-5′-phosphate-6-(2′-naphthylazo-6′-nitro-4′,8′-disulfonate) tetrasodium salt

* Corresponding author at: CNR-IBF, University of Milano, Via Celoria 26, 20133 Milano, Italy. Fax: +39 02 50314895.
E-mail address: eloise.mastrangelo@unimi.it (E. Mastrangelo).

[1] These authors have contributed equally to this work.

http://dx.doi.org/10.1016/j.febslet.2014.03.021
0014-5793/

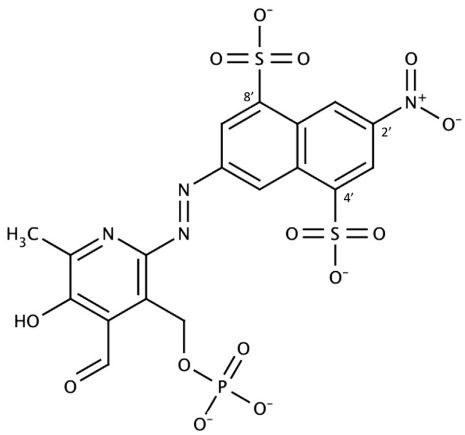

Fig. 1. Chemical structure of PPNDS.

permeability [17–19], we focused on Pyridoxal-5′-phosphate-6-(2′-naphthylazo-6′-nitro-4′,8′-disulfonate) tetrasodium salt (PPNDS), a different potential inhibitor identified by an in silico search that focused on a region around the active site of hNV RdRp. PPNDS, a specific P2X1 receptor antagonist [20], hosts a naphthalene disulfonate head (i.e. the Suramin moiety that strongly interacts with the enzyme [16]) and a pyridoxal phosphate group linked to the naphthalene head by an azo bond (Fig. 1). In the human (h) NV-RdRp/PPNDS complex structure, the compound was shown to bind in a region different from that occupied by suramin or by NF023 in their respective complexes [21]. Such a new site, named "B-site" in the hNV-RdRp [21], is located in the thumb domain, more specifically in a cleft along the exit path of the newly synthesized RNA.

Here we report the biochemical characterization, the in vitro enzymatic inhibition activity and the 3D-structure of mNV-RdRp in complex with PPNDS. Even though the 3D-structure showed the inhibitor bound to the B-site, confirming the relevance of this site for the inhibition of the enzyme, mNV-RdRp binds two PPNDS molecules; strikingly, their binding mode is reminiscent of two stacked RNA nucleotide bases. Additional differences between human and murine NV-RdRp/PPNDS structures have been observed and are here discussed, providing new structural bases for PPNDS modification aimed at improving its efficacy and drug-likeness.

2. Materials and methods

2.1. Chemicals

The compound PPNDS was purchased from Santa Cruz Biotechnology. The compound was dissolved at 100 mM in H_2O and stored at −20 °C.

2.2. Expression and purification of the mNV-RdRp

mNV-RdRp was expressed and purified as previously described [22]. The protein was dialyzed against 25 mM Tris/HCl pH 7.4, 1 mM *DTT*, 100 mM NaCl, 1 mM EDTA, and concentrated to 6 mg/ml.

2.3. mNV-RdRp inhibition assay

RdRp activity was assessed in vitro as described [16]. In brief, we followed the synthesis of double-stranded RNA from a single-stranded RNA polyC template (Sigma–Aldrich P4903) annealed with a G_{12} primer (62.5 nM final concentration) and 100 μM GTP, in a reaction mixture containing 20 mM Tris/HCl (pH 7.5), 1 mM DTT, 25 mM NaCl, 5 mM $MgCl_2$, 0,3 mM $MnCl_2$, 2 U RiboLock Ribonuclease inhibitor (Life technologies), PicoGreen Quantitation Reagent (Life technologies) (total volume of 200 μl). Before starting the reaction, 1 μl of the protein (final protein concentration of 715 nM) was incubated for 5 min with 1 μl of PPNDS (inhibitor concentration from 0 to 10 μM). The reactions were followed for 10 min at 30 °C measuring PicoGreen fluorescence (Varian, Cary Eclipse Fluorescence Spectrophotometer). The protein activity was evaluated subtracting the linear slope of the fluorescence from that of the assay mixture in the absence of the enzyme. The results of three independent experiments were averaged. Measurements of activity *vs.* inhibitor concentration were used to estimate the IC_{50} of each inhibitor using the program GraFit5 (Erithacus software) and reported in Fig. 1.

2.4. Biophysical characterization of the mNV-RdRp/PPNDS interaction

The fluorescent dye Sypro Orange (Sigma–Aldrich) was used to monitor protein unfolding. The unfolding process exposes hydrophobic regions of the protein under investigation, resulting in a fluorescence increase of the dye. Thermal shift assays of mNV-RdRp in the absence/presence of the inhibitor were run in a MiniOpticon Real Time PCR Detection System (Bio-Rad). Solutions of 4 μl of the mNV-RdRp (final protein concentration 33.6 μM) were mixed with 3.5 μl of Sypro Orange diluted 60×, 9.5 μl of its buffer and 1 μl of PPNDS (final concentration 50 μM). Distilled water was added in place of the inhibitor for the control samples. The sample plates were heated from 20 to 99 °C with a heating rate of 0.2 °C/min. Fluorescence intensities were measured within excitation/emission ranges of 470–505/540–700 nm.

2.5. Crystallization of the mNV-RdRp in presence of PPNDS

Microbatch crystallization experiments on mNV-RdRp were assembled using an Oryx-8 crystallization robot (Douglas

Table 1
X-ray data-collection and refinement statistics.

Protein	*mNV-RdRp/PPNDS*
PPNDS concentration [mM]	5 mM
Space group and wavelength [Å]	C2, 0.976
Unit-cell parameters (Å, °)	a = 119.7, b = 197.4, c = 109.6 β = 114.1°
Molecules in a.u.	3
Resolution (Å)	59.4–2.4
Mosaicity (°)	0.3
Unique reflections	90,345 (13,152)[a]
Completeness (%)	100 (100)
Redundancy	3.7 (3.8)
R_{merge}[†] (%)	14.6 (83.5)
Average I/σ (I)	6.4 (2.0)
R_{factor}[‡]/R_{free}[§] (%)	19.2/24.9
r.m.s. bonds (Å)	0.010
r.m.s. angles (°)	1.39
Average protein B factors (Å^2)	A = 41.3, B = 43.7 C = 49.4
Average ligand B factors (Å^2)	A1 = 69.7, B1 = 70.0, C1 = 64.0 A2 = 73.0, B2 = 71.4, C2 = 67.3
Residues in most favored regions (%)[b]	93.1
Residues in additionally allowed regions (%)[b]	6.7
PDB	4O4R

[a] Values in parentheses are for the highest resolution shell: (2.53–2.40).
[b] Parameters are referred to Ramachandran plot.
[†] $R_{merge} = \Sigma\ |I - (I)|/\Sigma\ I \times 100$, where I is intensity of a reflection and (I) is its average intensity.
[‡] $R_{factor} = \Sigma\ |F_o - F_c|/\Sigma\ |F_o| \times 100$.
[§] R_{free} is calculated on 5% randomly selected reflections, for cross-validation.

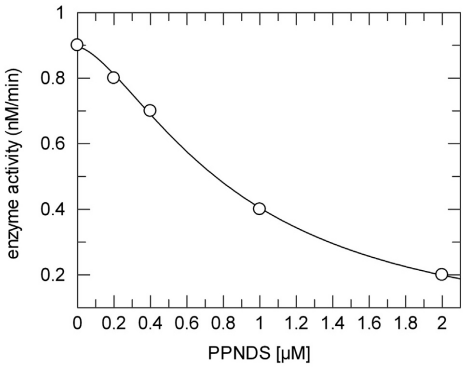

Fig. 2. Protein activity *vs.* PPNDS concentration. Continuous lines are the fits obtained using the four parameters equation described in Section 2.

Instruments). In a typical experiment 0.4 μl drops of 2:1:1 mixture of protein (10 mg/ml), reservoir solution and $MgCl_2$ (25 mM in the drop) were placed on a 96 well plate (Hampton Research), and covered by a mixture of 50% Paraffin oil and 50% Silicon oil. Prismatic crystals of approximately 150 × 80 × 30 μm^3 were obtained after 1 week at 20 °C, in 1.6 M $(NH_4)_2SO_4$, 12% glycerol, 100 mM TRIS/HCl pH 8.4. Crystals were soaked in a cryoprotectant solution (1.8 M $(NH_4)_2SO_4$, 100 mM TRIS/HCl pH 8.4, and 25% glycerol) with 5 mM of PPNDS, in the presence of 62.5 nM dsRNA (polyC-G_{12}) and 10 μM GTP for 36 h, then flash-cooled in liquid nitrogen. Crystals diffracted to a maximum resolution of 2.4 Å using synchrotron radiation on beam-line ID23-1 at the European Synchrotron Radiation Facility (ESRF-Grenoble, France). X-ray diffraction data were processed using MOSFLM [23], and intensities were merged using SCALA [24].

2.6. Structure determination and refinement

The mNV-RdRp/PPNDS crystal belongs to the monoclinic space group C2, with unit cell parameters a = 119.7 Å, b = 197.4 Å, c = 109.6 Å; β = 114.1°, with 3 molecules in the asymmetric unit (V_m = 3.31 $Å^3$ Da^{-1}, 62.9% solvent content [25]). The three-dimensional structure was solved by Molecular Replacement (MOLREP program) [26] using a search model based on the mNV-RdRp structure (PDB-id: 3UQS.pdb [16]). The three independent molecules in the crystal asymmetric unit (A, B and C) were subjected to rigid-body refinement, and subsequently refined using REFMAC5 [27]. A random set comprising 5% of the data was omitted from refinement for *R*-free calculation. Manual rebuilding and additional refinement (with BUSTER [28], REFMAC5 and COOT [29]) were subsequently performed, as needed. Data collection, refinement statistics as well as stereochemical quality of the models are summarized in Table 1.

3. Results

3.1. In vitro inhibition of mNV-RdRp

mNV-RdRp inhibition assays were performed monitoring the impairment of RNA synthesis as a function of inhibitor concentration. In vitro RNA synthesis was assayed using annealed polyC-G_{12} and GTP as polymerase substrates, as previously described [16]. Under such experimental conditions, PPNDS inhibited mNV-RdRp

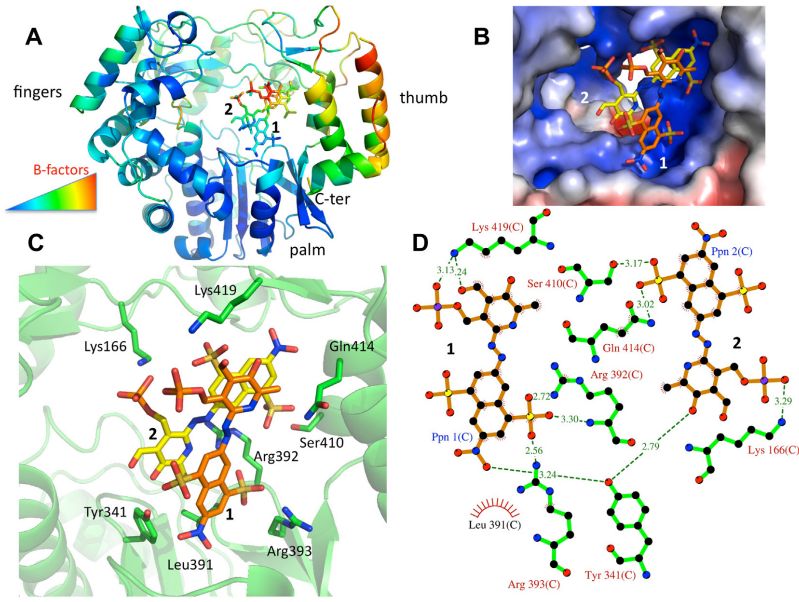

Fig. 3. The crystal structure of mNV-RdRp bound to two molecules of PPNDS. (A) In cartoon mNV-RdRp and in sticks the two PPNDS molecule colored using B-factors rainbow (low values in blue high values in red). (B) The inhibitors bound to the protein colored by electrostatic potential (from −7 kT/e red to +7 kT/e blue; APBS, [32]. (C) The main amino acids of mNV-RdRp (carbon in green sticks) interacting with PPNDS-1 (orange carbon sticks) and PPNDS-2 (yellow carbon sticks). (D) Schematic representation of the interactions between the two molecules of PPNDS (in orange) and mNV-RdRP (in green; LigPlot, [33]). Figure was created using PyMOL (http://www.pymol.org).

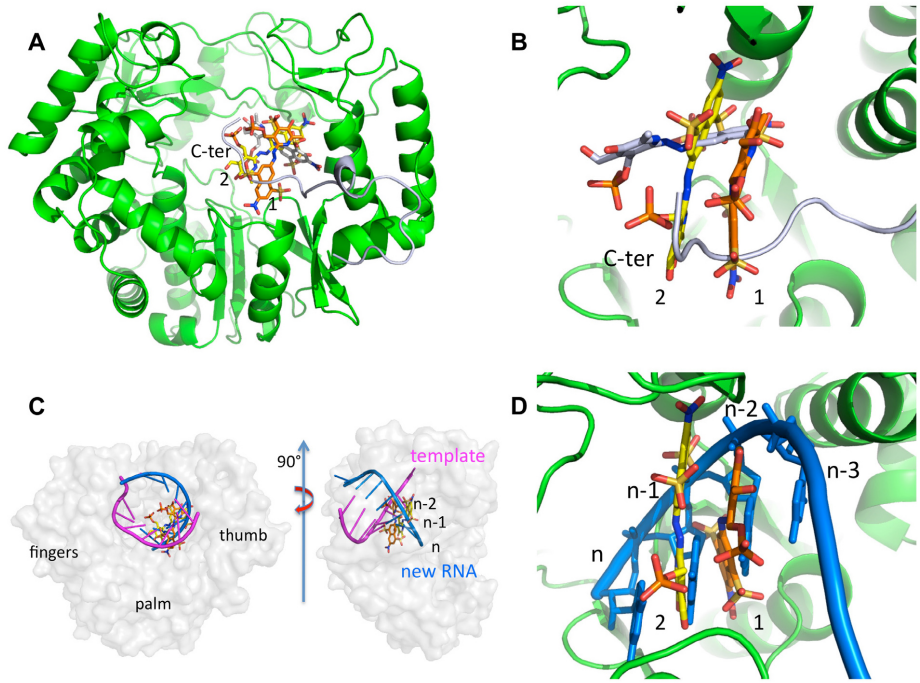

Fig. 4. Comparison of the binding mode of PPNDS in mNV- and hNV-RdRps and the binding of RNA to the polymerase. (A) The overall structure of mNV-RdRp (in green cartoon) with the two PPNDS molecules (orange and yellow carbon atoms) superimposed on the hNV-RdRp/PPNDS complex, for which PPNDS (gray carbon atoms) and the C-terminal end located into the protein active site (gray cartoon) are shown. (B) close up view as in (A) but with different orientation. (C) The overall structure of mNV-RdRp (gray surface; with the PPNDS molecules in orange and yellow carbon atoms) superimposed on the hNV-RdRp bound to dsRNA (pdb-ID: 3BSN [31]). (D) Close up view as in (C).

with an IC_{50} value of 0.88 ± 0.03 μM (Fig. 2), a value that is closely comparable with that of Suramin (0.30 ± 0.04 μM).

3.2. Thermofluorimetric assays

The specificity of the PPNDS inhibition was verified by excluding any off-target effects on the overall native protein fold, such as ligand-induced destabilization/aggregation/denaturation. To this aim, thermal denaturation analysis using Sypro-orange as fluorescent probe were performed. In fact, although the thermofluorimetric signal was markedly reduced in the presence of PPNDS, which absorbs the incident radiation in the 470–505 nm region, we were able to determine the mNV-RdRp melting temperature (T_m) that resulted to be essentially the same in the absence (T_m = 39.8 ± 0.2 °C) or in the presence (T_m = 39.8 ± 0.1 °C) of PPNDS (50 μM).

3.3. Crystal structure of mNV-RdRp bound to PPNDS

Details of the PPNDS binding mode to mNV-RdRp were addressed through X-ray crystallography. To this purpose, co-crystallization and soaking experiments of the purified mNV-RdRp in the presence of saturating amounts of PPNDS were systematically set up without significant results. Crystals of mNV-RdRp bound to PPNDS could be prepared only after soaking the enzyme crystals with 5 μM of the inhibitor in the presence of dsRNA and GTP i.e. mimicking the conditions met during the polymerase activity (see Section 2). The crystals thus obtained (belonging to the space group C2, with 3 molecules per asymmetric unit) diffracted to 2.4 Å, maximum resolution; the mNV-RdRp/PPNDS structure was solved by molecular replacement (model's pdb-id: 3UQS) and refined to final crystallographic *R*-factor/*R*-free values of 19.2/24.9%, (Table 1). Inspection of difference Fourier maps at various stages of the crystallographic refinement revealed strong residual electron density located between the thumb and palm domains, compatible with two PPNDS molecules that were accordingly modeled in antiparallel stacking orientation (Fig. 3A–D). The inhibitor molecule whose naphtalene disulfonate moiety is closer to the palm domain was named PPNDS-1, the other PPNDS-2 (Fig. 3A–D).

Inspection of the enzyme/inhibitor complex structure, compared to that of mNV-RdRp inhibitor-free structure (pdb-id: 3UQS [16]), shows only minor conformational changes in the protein backbone (r.m.s.d. 0.65 Å calculated over 469 C α airs). Most specifically, we observed a slight repositioning of the 390–393 β-turn, from Type I' to Type II' with flipping of Leu391 Ψ by ~170° (from 36° to −130°) to accommodate the 4′ sulfonate and the nitro group of PPNDS-1. Such main chain movement is accompanied by conformational changes in the side chains of Arg392, Arg393 and Tyr341, to accommodate both PPNDS molecules. As a whole, PPNDS-1 shows a lower average B-factor relative to PPNDS-2, and the two inhibitor-molecules appear to be more tightly linked to the protein in their respective moieties that are closer to the palm domain (Fig. 3A). In fact, PPNDS-1 naphtalene moiety is nicely hosted in a low-polarity site formed by Tyr341, Met219,

Met221 and Leu391, whereas the PPNDS-2 pyridoxal phosphate moiety, besides the stacking interaction with PPNDS-1, is H-bonded to Tyr341 and Lys166, and its azo group is in cation–π interaction with Arg392 (3.22 Å; Fig. 3D). Considering the inhibitors' portions that display higher mobility (as judged by B-factors), PPNDS-2 naphtalene moiety is close to the thumb domain, with the 4′ sulphonate interacting with Ser410, Arg413, and Gln414 (belonging to the helix α13), and the PPNDS-1 pyridoxal phosphate negative charge is balanced by Lys419.

4. Discussion

Two PPNDS molecules bind to mNV-RdRp nestled between the palm and thumb domains, in a site close to the 'B-site' already characterized for hNV-RdRp [21]. The two inhibitor molecules display an evident antiparallel stacking interaction, roughly aligned along the main alpha helices of the thumb domain (Fig. 3A), and adopt an orientation rotated by about 60° relative to that observed for the single PPNDS molecule bound to hNV-RdRp (Figs. 4A, B, and S1A). Such significant changes are likely related to the insertion of the C-terminal segment of the hNV-RdRp (aa. 490–506) [30,31] inside the enzyme active site region (both in the inhibitor-free and in the PPNDS bound structures), an event that translates into a direct interaction of some C-terminal amino acids with the bound inhibitor [21] (Fig. 4B). On the contrary, in mNV-RdRp the C-terminal segment is disordered beyond Gly488, as expected considering the overall higher B-factors displayed by the whole C-terminal thumb domain (Fig. 3A), thus leaving more room in the active site region for the incoming inhibitory molecules. Interestingly, in hNV-RdRp the C-terminal end of the protein occupies the site that in mNV-RdRp are taken by the less mobile portions of the inhibitors, i.e. pyridoxal phosphate in PPNDS-1, and naphtalene in PPNDS-2 (Fig. 4B).

It must be stressed that PPNDS-1 and PPNDS-2, in their antiparallel stacking interaction, are in a location close to the region that would be taken by the newly formed ssRNA chain, as inferred by superposition with the structure of hNV-RdRp bound to dsRNA (pdb-id 3BSN [31]; Figs. 4C, D and S1B). In particular, PPNDS-1 and PPNDS-2, after superimposition, fall on nucleotides n-2 and n-1, respectively (n being the nucleotide that will be linked to the incoming NTP; Fig. 4C and D). Notably, the inhibitor portions that are better linked to the enzyme, i.e. the naphthalene portion of PPNDS-1 and the pyridoxal group of PPNDS-2 (Fig. 3A), would take the place of the RNA bases, while the more mobile inhibitor parts would match the phosphodiester backbone (Fig. 3B), in the interaction with the flexible thumb domain of the protein (Fig. 3A). Thus, our structural results on mNV-RdRp show that PPNDS can display properties allowing it to mimic the stacking interaction of two linked bases in RNA as well as the phosphodiester bond linkage. As a perspective, such RNA-like property of the inhibitor might be improved by covalently linking the phosphate moieties of the two PPNDS molecules that are found in close contact in the X-ray structure here presented.

Acknowledgements

The work at University of Milano and CNR (Milano, Italy) and at Riboxx GmbH (Dresden Germany) was supported by the European Commission Seventh Framework Programme (FP7/2007-20013) through the SILVER project (Small inhibitor leads against emerging RNA viruses, grant agreement 260644).

Appendix A. Supplementary data

Supplementary data associated with this article can be found, in the online version, at http://dx.doi.org/10.1016/j.febslet.2014.03.021.

References

[1] Green, K.Y., Ando, T., Balayan, M.S., Berke, T., Clarke, I.N., Estes, M.K., Matson, D.O., Nakata, S., Neill, J.D., Studdert, M.J. and Thiel, H.J. (2000) Taxonomy of the caliciviruses. J. Infect. Dis. 181 (Suppl. 2), S322–S330.
[2] Mayo, M.A. (2002) A summary of taxonomic changes recently approved by ICTV. Arch. Virol. 147, 1655–1663.
[3] Fauquet, C.M. and Fargette, D. (2005) International Committee on Taxonomy of Viruses and the 3142 unassigned species. Virol. J. 2.
[4] Green, K.Y. (2007) Caliciviridae: the noroviruses. Fields Virol. 5, 949–979.
[5] Patel, M.M., Widdowson, M.-A., Glass, R.I., Akazawa, K., Vinjé, J. and Parashar, U.D. (2008) Systematic literature review of role of noroviruses in sporadic gastroenteritis. Emerg. Infect. Dis. 14, 1224–1231.
[6] Bok, K. and Green, K.Y. (2012) Norovirus gastroenteritis in immunocompromised patients. New Engl. J. Med. 367, 2126–2132.
[7] Huang, C., Hess, J., Gill, M. and Hustead, D. (2010) A dual-strain feline calicivirus vaccine stimulates broader cross-neutralization antibodies than a single-strain vaccine and lessens clinical signs in vaccinated cats when challenged with a homologous feline calicivirus strain associated with virulent systemic disease. J. Feline Med. Surg. 12, 129–137.
[8] Rohayem, J., Bergmann, M., Gebhardt, J., Gould, E., Tucker, P., Mattevi, A., Unge, T., Hilgenfeld, R. and Neyts, J. (2010) Antiviral strategies to control calicivirus infections. Antivir. Res. 87, 162–178.
[9] Wobus, C.E., Thackray, L.B. and Virgin, H.W. (2006) Murine norovirus: a model system to study norovirus biology and pathogenesis. J. Virol. 80, 5104–5112.
[10] Thackray, L.B., Wobus, C.E., Chachu, K.A., Liu, B., Alegre, E.R., Henderson, K.S., Kelley, S.T. and Virgin, H.W. (2007) Murine noroviruses comprising a single genogroup exhibit biological diversity despite limited sequence divergence. J. Virol. 81, 10460–10473.
[11] McFadden, N., Bailey, D., Carrara, G., Benson, A., Chaudhry, Y., Shortland, A., Heeney, J., Yarovinsky, F., Simmonds, P. and Macdonald, A. (2011) Norovirus regulation of the innate immune response and apoptosis occurs via the product of the alternative open reading frame 4. PLoS Pathog. 7.
[12] Blakeney, S.J., Cahill, A. and Reilly, P.A. (2003) Processing of Norwalk virus nonstructural proteins by a 3C-like cysteine proteinase. Virology 308, 216–224.
[13] Liu, B., Clarke, I.N. and Lambden, P.R. (1996) Polyprotein processing in Southampton virus: identification of 3C-like protease cleavage sites by in vitro mutagenesis. J. Virol. 70, 2605–2610.
[14] Sosnovtsev, S.V., Belliot, G., Chang, K.-O., Prikhodko, V.G., Thackray, L.B., Wobus, C.E., Karst, S.M., Virgin, H.W. and Green, K.Y. (2006) Cleavage map and proteolytic processing of the murine norovirus nonstructural polyprotein in infected cells. J. Virol. 80, 7816–7831.
[15] Clarke, I.N. and Lambden, P.R. (2000) Organization and expression of calicivirus genes. J. Infect. Dis. 181.
[16] Mastrangelo, E., Pezzullo, M., Tarantino, D., Petazzi, R., Germani, F., Kramer, D., Robel, I., Rohayem, J., Bolognesi, M. and Milani, M. (2012) Structure-based inhibition of Norovirus RNA-dependent RNA polymerases. J. Mol. Biol. 419, 198–210.
[17] Beindl, W., Mitterauer, T., Hohenegger, M., Ijzerman, A.P., Nanoff, C. and Freissmuth, M. (1996) Inhibition of receptor/G protein coupling by suramin analogues. Mol. Pharmacol. 50, 415–423.
[18] Charlton, S.J., Brown, C.A., Weisman, G.A., Turner, J.T., Erb, L. and Boarder, M.R. (1996) PPADS and suramin as antagonists at cloned P2Y-and P2U-purinoceptors. Br. J. Pharmacol. 118, 704–710.
[19] Klinger, M., Bofill-Cardona, E., Mayer, B., Nanoff, C., Freissmuth, M. and Hohenegger, M. (2001) Suramin and the suramin analogue NF307 discriminate among calmodulin-binding sites. Biochem. J. 355, 827–833.
[20] Lambrecht, G., Rettinger, J., Bäumert, H.G., Czeche, S., Damer, S., Ganso, M., Hildebrandt, C., Niebel, B., Spatz-Kümbel, G. and Schmalzing, G. (2000) The novel pyridoxal-5′-phosphate derivative PPNDS potently antagonizes activation of P2X(1) receptors. Eur. J. Pharmacol. 387.
[21] Tarantino, D., Pezzullo, M., Mastrangelo, E., Croci, R., Rohayem, J., Robel, I., Bolognesi, M. and Milani, M. (2013) Naphtalene-sulfonate inhibitors of human norovirus RNA-dependent RNA-polymerase. Antivir. Res. 102, 23–28.
[22] Fullerton, S.W.B., Blaschke, M., Coutard, B., Gebhardt, J., Gorbalenya, A., Canard, B., Tucker, P.A. and Rohayem, J. (2007) Structural and functional characterization of sapovirus RNA-dependent RNA polymerase. J. Virol. 81, 1858–1871.
[23] Leslie, A.G. and Powell, H.R. (2007) Processing diffraction data with MosflmEvolving Methods for Macromolecular Crystallography, pp. 41–51, Springer.
[24] Evans, P. (2006) Scaling and assessment of data quality. Acta Crystallogr. Sect. D: Biol. Crystallogr. 62, 72–82.
[25] Matthews, B.W. (1968) Solvent content of protein crystals. J. Mol. Biol. 33, 491–497.
[26] Vagin, A. and Teplyakov, A. (2010) Molecular replacement with MOLREP. Acta Crystallogr. Sect. D: Biol. Crystallogr. 66, 22–25.
[27] Steiner, R.A., Lebedev, A.A. and Murshudov, G.N. (2003) Fisher's information in maximum-likelihood macromolecular crystallographic refinement. Acta Crystallogr. Sect. D: Biol. Crystallogr. 59, 2114–2124.
[28] Smart, O.S., Womack, T.O., Flensburg, C., Keller, P., Paciorek, W., Sharff, A., Vonrhein, C. and Bricogne, G. (2012) Exploiting structure similarity in refinement: automated NCS and target-structure restraints in BUSTER. Acta Crystallogr. Sect. D: Biol. Crystallogr. 68, 368–380.

[29] Emsley, P., Lohkamp, B., Scott, W.G. and Cowtan, K. (2010) Features and development of Coot. Acta Crystallogr. Sect. D: Biol. Crystallogr. 66, 486–501.
[30] Ng, K.K.-S., Pendás-Franco, N., Rojo, J., Boga, J.A., Machín, À., Alonso, J.M.M. and Parra, F. (2004) Crystal structure of norwalk virus polymerase reveals the carboxyl terminus in the active site cleft. J. Biol. Chem. 279, 16638–16645.
[31] Zamyatkin, D.F., Parra, F., Alonso, J.M.M., Harki, D.A., Peterson, B.R., Grochulski, P. and Ng, K.K.-S. (2008) Structural insights into mechanisms of catalysis and inhibition in Norwalk virus polymerase. J. Biol. Chem. 283, 7705–7712.
[32] Baker, N.A., Sept, D., Joseph, S., Holst, M.J. and McCammon, J.A. (2001) Electrostatics of nanosystems: application to microtubules and the ribosome. Proc. Natl. Acad. Sci. 98, 10037–10041.
[33] Wallace, A.C., Laskowski, R.A. and Thornton, J.M. (1995) LIGPLOT: a program to generate schematic diagrams of protein–ligand interactions. Protein Eng. 8, 127–134.

Structural Bases of Norovirus RNA Dependent RNA Polymerase Inhibition by Novel Suramin-Related Compounds

Romina Croci[1☯], Margherita Pezzullo[1☯], Delia Tarantino[1], Mario Milani[1,2], Shwu-Chen Tsay[3], Radhakrishnan Sureshbabu[4], Yi-Jin Tsai[4], Eloise Mastrangelo[1,2], Jacques Rohayem[5,6], Martino Bolognesi[1]*, Jih Ru Hwu[3,4]*

1 Department of BioSciences, University of Milano, Milano, Italy, **2** Istituto di Biofisica,CNR IBF, Milano, Italy, **3** Department of Chemistry, National Central University, Jhongli, Taiwan, **4** Department of Chemistry and Frontier Research Center on Fundamental and Applied Sciences of Matters, National Tsing Hua University, Hsinchu, Taiwan, **5** Riboxx GmbH, Pharmapark Radebeul, Radebeul, Germany, **6** Institute of Virology, Dresden University of Technology, Dresden, Germany

Abstract

Noroviruses (NV) are +ssRNA viruses responsible for severe gastroenteritis; no effective vaccines/antivirals are currently available. We previously identified Suramin (**9**) as a potent inhibitor of NV-RNA dependent RNA polymerase (NV-RdRp). Despite significant *in vitro* activities *versus* several pharmacological targets, Suramin clinical use is hampered by pharmacokinetics/toxicity problems. To improve Suramin access to NV-RdRp *in vivo*, a Suramin-derivative, **8**, devoid of two sulphonate groups, was synthesized, achieving significant anti-human-NV-RdRp activity (IC_{50} = 28 nM); the compound inhibits also murine NV (mNV) RdRp. The synthesis process led to the isolation/characterization of lower molecular weight intermediates (**3–7**) hosting only one sulphonate head. The crystal structures of both hNV/mNV-RdRps in complex with **6**, were analyzed, providing new knowledge on the interactions that a small fragment can establish with NV-RdRps, and establishing a platform for structure-guided optimization of potency, selectivity and drugability.

Citation: Croci R, Pezzullo M, Tarantino D, Milani M, Tsay S-C, et al. (2014) Structural Bases of Norovirus RNA Dependent RNA Polymerase Inhibition by Novel Suramin-Related Compounds. PLoS ONE 9(3): e91765. doi:10.1371/journal.pone.0091765

Editor: Stephen J Polyak, University of Washington, United States of America

Received December 10, 2013; **Accepted** February 14, 2014; **Published** March 12, 2014

Funding: National Science Council (NSC 102-2923-I-008-001), Ministry of Education of the R.O.C., Taiwan (grants nos. 102N2011E1 and 102N2018E1), and National Central University (102G918). The work at University of Milano and CNR (Milano, Italy) and at Riboxx GmbH (Dresden Germany) was supported by the European Commission SILVER project, within the 7th Framework Program Cooperation Project Grant Agreement No. 2606444. The funders had no role in study design, data collection and analysis, decision to publish, or preparation of the manuscript.

Competing Interests: Co-author Dr J. Rohayem is an employee of the company Riboxx GmbH (Germany) and this function does not lead to conflicts of interest and does not alter our adherence to PLOS ONE policies on sharing data and materials.

* E-mail: martino.bolognesi@unimi.it (MB); jrhwu@mx.nthu.edu.tw (JH)

☯ These authors contributed equally to this work.

Introduction

Norovirus (formerly Norwalk-like virus, NV) is a genus of the *Caliciviridae* family that is a major causative agent of non-bacterial acute gastroenteritis in humans. Outbreaks commonly occur in settings such as hospitals, nursing homes, cruise ships, university dormitories, and military barracks. It is estimated that NV infection may account for up to 200,000 deaths per year in infants and young children of the developing countries [1], [2]. Currently, no vaccines [3], [4] or specific antiviral agents are available to combat NV; thus, there is an urgent and still unmet need for discovery and development of broad spectrum small-molecule therapeutics against this severe pathogen. Human NVs are fairly species-specific and do not appear to infect small animals, even if animal models are under development [5], [6], [7]. A widely used model system shedding light on NV pathogenesis and replication strategies is the murine model of NV infection, obtained by infecting mice with murine NVs (mNVs) [8]. The calicivirus genomes consist of a single stranded, positive-sense poly-adenylated RNA molecule that averages 7500 nucleotides in length. It is organized in either two or three open reading frames (ORF-1 to ORF-3), depending on the particular genus. ORF-1 is predicted to encode a single polyprotein that, after co-translational processing by the viral protease, results in the nonstructural proteins required for replication of the viral genome [9], [10] and their precursors [11]. Among these, nonstructural protein 7 [RNA-dependent RNA polymerase (RdRp) domain] plays a key role in genome replication, as well as in the synthesis and amplification of additional subgenomic RNA [12]. Notably, since RdRp is not present in mammalian cells, it appears as a suitable target for inhibition in the context of antiviral prophylaxis. Suramin (**9**, Fig. 1) is a polysulphonated naphthylurea, which has been used as the drug of choice for treatment of African trypanosomiasis and onchocerciasis since 1924 [13]. Different Suramin applications have been reported, including inhibition of reverse transcriptase [14], P2X and P2Y nucleotide receptor family antagonism [15], [16], and blocking actions on various growth factors [17]. Also, since Suramin hinders cell proliferation and migration, as well as the formation of new blood vessels, it has been tested for potential use as an anticancer agent [18]; moreover, Suramin was noted to induce hyperglycaemia [19], [20]. Several clinical trials based on Suramin and Suramin-like

compounds have nevertheless proven unsatisfactory, as *in vitro* results did not translate into the desired clinical response *in vivo*. Except for trypanosomiasis, in fact, all other trials did not reach the clinical level due to challenges related to Suramin pharmacokinetics and toxicity [20], [21], [22]. We previously identified Suramin as a potent inhibitor of hNV and mNV-RdRps, and solved the crystal structures of mNV RdRp in the absence/presence of Suramin, highlighting an inhibitor binding site located between the RdRp fingers and thumb domains. In particular, the cleft occupied by the inhibitor is lined with conserved amino acids, likely building the access route for the incoming NTP that will be linked to the nascent RNA chain. [23]. Due to the high potency of Suramin in enzymatic assays, its optimization into a more drug-like compound would not require enhancing its interaction with the therapeutic target (*e.g.* hNV-RdRp), rather it should improve the ability of Suramin to reach the therapeutic target *in vivo*. Suramin is a polar compound, with log *P* value lower than 0; thus, it is likely to traverse the epithelium slowly *via* paracellular channels. In addition, it should be recalled that Suramin's high molecular weight (1429 Da) might promote biliary excretion, reducing its overall systemic bioavailability [24], [25].

The crystal structure of mNV-RdRp in complex with Suramin showed that only two of the three sulphonate groups on the Suramin naphthalene rings establish ionic interactions with basic residues of the enzyme [23]. On the basis of such structural information we undertook the chemical synthesis and biochemical characterization of carbamide **8** (see Fig. 1), a Suramin derivative bearing only two sulphonate groups on each naphthalene ring, as a first optimization step. We then characterized **8**, together with lower molecular weight synthetic reaction intermediates, in enzymatic inhibition assays versus hNV and mNV RdRps. To further address the inhibitory mechanistic issues, and to gather new information for rational drug design, we then analyzed the crystal structures of both hNV and mNV-RdRps in their complexes with diamide **6**, one of the reaction intermediates hosting only one sulphonate head, showing a favorable log *P* value relative to Suramin.

Aiming to further develop anti-norovirus compounds, we report here the details of the synthetic steps to produce five inhibitors, the analysis of their hNV and mNV-RdRp inhibitory activities, together with the crystal structure analysis of hNV and mNV-RdRps in their complexes with **6**, a low molecular weight representative compound in this class.

Results

Syntheses and Spectral Characteristics of Carbamide 8

For examination of the effects resulting from the sulphonate group (in position 3) of compounds in the family of Suramin (**9**), a total synthesis of carbamide **8** was performed as shown in Fig. 1. The condensation of commercially available nitrobenzoyl chloride **1** with sodium naphthalene disulphonate **2** in water at pH 4.0 yielded nitroamide **3** in 81% yield. Reduction of the nitro group in compound **3** with hydrogen gas in the presence of Pd catalyst led to the corresponding aniline **4** in excellent yield; meanwhile, the two aryl groups remained intact. A repeat of the same type of condensation reaction by use of aniline **4** and benzoyl chloride **5** afforded the desired diamide **6**, which was further hydrogenated to give stable sodium salt of aniline **7**. Solubility of this compound was found very poor in most of organic solvents, including THF and DMSO. The carbonylation of aniline **7** with 1, 1′-carbonyldiimidazole (CDI) [26] in a mixture of water and toluene in different ratios at room temperature or under reflux conditions did not lead to the desired carbamide **8**. Instead, the starting materials remained intact. This problem was circumvented by use of triphosgene in a slight excess to react with aniline **7** at pH 3.0 in an aqueous Na_2CO_3 solution containing toluene. Accordingly, **8** was generated as a white powder in 83% yield.

The structures of sulphonates **3**–**8** were confirmed by their spectroscopic characteristics. For instance, the exact mass of carbamide **8** $(C_{51}H_{36}N_6Na_4O_{17}S_4+2\ Na)^{2+}$ was measured by the electrospray ionization (ESI) method as 635.0116, which is very close to its theoretical value of 635.0197. Its ^{13}C NMR spectrum displayed 26 peaks as expected; among which the peak with $\delta = 153.53$ was attributed to the carbamido carbon (*i.e.* NCON). Two peaks at $\delta = 165.81$ and 165.06 in the downfield region belonged to the two different amide carbons. Its ^1H NMR spectrum showed nine sets of peaks, which resonated between 9.09–7.37 ppm with singlet, doublet, and triplet. They were associated with the aromatic protons with the expected splitting pattern for carbamide **8**. Its IR spectrum exhibited strong absorptions at 1652 and 1634 cm^{-1}, which were attributed to the stretching vibration of an amido carbonyl group.

Physical and Biological Properties of Sodium Organosulfonates 3–8 and Suramin (9)

Bookser's method [27] was applied to obtain the water solubility of sodium organosulphonates **3**–**8** and Suramin (**9**) by use of HPLC with a UV detector (see Table 1). Furthermore, the "shake–flask method" [28] was applied to obtain their hydrophobicity by use of *n*-octanol and water. The apparent partition coefficient (*P*) shown in Table 1 is the ratio of the concentration in *n*-octanol to the total concentration (*i.e.*, ionized plus non-ionized) of the species in the aqueous phase, [29].

Enzymatic assays

hNV and mNV-RdRp inhibition assays were performed monitoring the impairment of RNA synthesis as a function of inhibitor concentration, as previously described [23]. Briefly, RdRp activity was assessed *in vitro* (measuring PicoGreen fluorescence) following the synthesis of double-stranded RNA from a single-stranded RNA poly(C) template annealed with a G_{12} primer. The assay can easily be adapted for any viral RNA polymerase [30]. Under our experimental conditions, **8** inhibited hNV-RdRp with the same IC_{50} value of Suramin (~30 nM), whereas **6** and other synthetic intermediates proved to be ~30–35-fold less potent (Table 2). All the low molecular weight compounds (**3**–**7**) are generally more potent inhibitors of mNV rather than of hNV-RdRp (Table 2).

Thermofluorimetric assays

In order to exclude that **8** and **6** inhibition might be linked to some form of RdRp destabilization/aggregation/denaturation, a process generally reflected by a variation of the protein melting temperature (T_m), we performed thermofluorimetric assays on free and inhibited NV-RdRps. All the acquired data showed that NV-RdRps displays similar melting temperatures in the absence (hNV/mNV-RdRp Tm = 41.5/39.6 ±0.2 °C), or in the presence of **6** (hNV/mNV-RdRp Tm = 41.2±0.2/39.4±0.3 °C), or of **8** (hNV/mNV-RdRp Tm = 41.4/39.8 ±0.2 °C), thus proving that enzyme inhibition is not caused by denaturation of the protein.

Crystal structures of NV-RdRps bound to 6

To shed light on the mechanisms of RdRp inhibition exerted by the organic sulphonate compounds described above, we undertook crystallographic analyses of both enzymes in their complexes with **6**. To address the crystal structures of the **6** adduct, hNV-RdRp

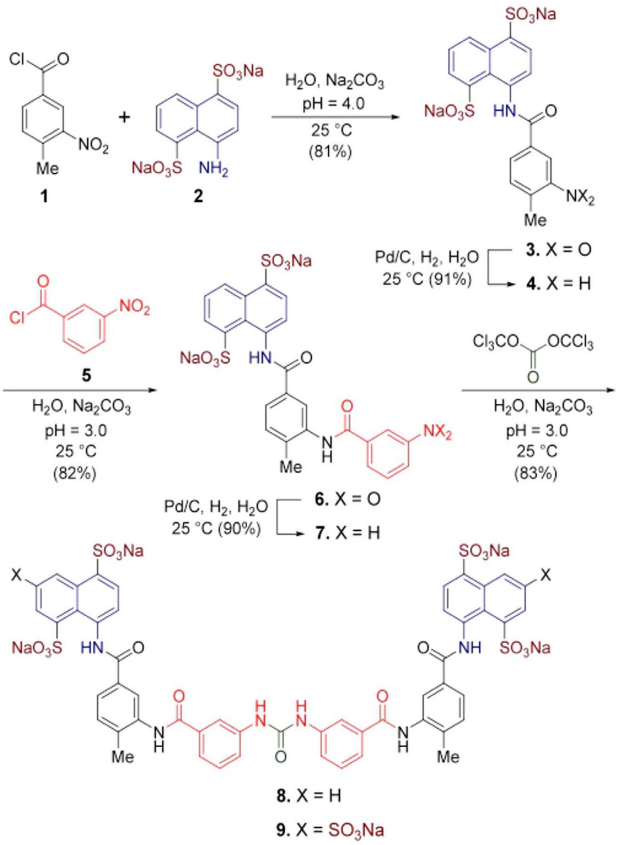

Figure 1. Suramin derivative 8 synthesis. Total synthesis of Suramin derivative **8** from commercially available starting materials. The Suramin molecule (**9**) is also shown for comparison.
doi:10.1371/journal.pone.0091765.g001

Table 1. Water solubility and hydrophobicity of organic sulphonates **3–8** and Suramin.

Compound	water solubility[a] (mg/ml)	hydrophobicity[b] log *P*
3	260	−2.19
4	339	−2.33
6	179	−1.64
7	249	−2.11
8	114	−1.61
Suramin (**9**)	138	−3.42

[a]The Bookser's method was applied.
[b]The shake–flask method was applied.
doi:10.1371/journal.pone.0091765.t001

Table 2. IC_{50} values of Suramin derivatives and Suramin (**9**) against mNV and hNV-RdRps.

	IC_{50} (nM)	
Compound	**mNVRdRp**	**hNVRdRp**
3	200±10	1280±70
4	160±7	1100±200
6	115±15	1000±90
7	160±6	1100±50
8	60±4	28±4
Suramin (**9**)	70±3	27±3

doi:10.1371/journal.pone.0091765.t002

Table 3. X-ray data-collection and refinement statistics for the hNV-RdRP/**6** complex.

Protein crystals	*hNV-RdRp/6*	*mNV-RdRp/6*
6 concentration (mM)	10	20
Resolution (Å)	71.80–2.02	64.96–2.30
Space group	I222	$P2_1$
Unit-cell parameters (Å, °)	$a=89.2$; $b=112.0$; $c=121.1$	$a=109.2$; $b=162.4$; $c=123.0$ $\beta=97.0°$
Molecules in a.u.	1	6
Mosaicity (°)	0.2	0.3
Unique reflections	39,356 (5,729)*	188,102 (27,425)*
Completeness (%)	98.8 (99.1)	99.9 (99.8)
Redundancy	3.1 (3.2)	3.2 (3.2)
Rmerge† (%)	8.4 (30.5)	9.8 (72.0)
Average I/σ (I)	8.4 (3.4)	7.7 (1.6)
R factor‡/Rfree§ (%)	16.4/20.9	19.1/25.4
r.m.s.d. bonds (Å)	0.011	0.010
r.m.s.d. angles (°)	1.48	1.33
Average protein *B* factors (Å^2)	28.2	A = 38.4, B = 39.9, C = 42.0, D = 42.9, E = 49.5, F = 58.4
Average ligand *B* factors (Å^2)	55.6	A = 78.2, B = 58.9, C = 70.2, D = 67.3, E = 85.5, F = 87.7
Residues in most favored regions (%)	95.0	92.9
Residues in additionally allowed regions (%)	5.0	7.1
PDB	4NRT	4NRU

*Values in parentheses are for the highest resolution shell: (2.13–2.02 Å for hNV RdRp/**6**, 2.42–2.30 Å for mNV RdRp/**6**).
†$R_{merge} = \Sigma |I-\langle I\rangle|/\Sigma I \times 100$, where I is intensity of a reflection and $\langle I\rangle$ is its average intensity.
‡$R_{factor} = \Sigma ||F_o|-|F_c||/\Sigma |F_o| \times 100$.
§R_{free} is calculated on 5% randomly selected reflections, for cross-validation.
doi:10.1371/journal.pone.0091765.t003

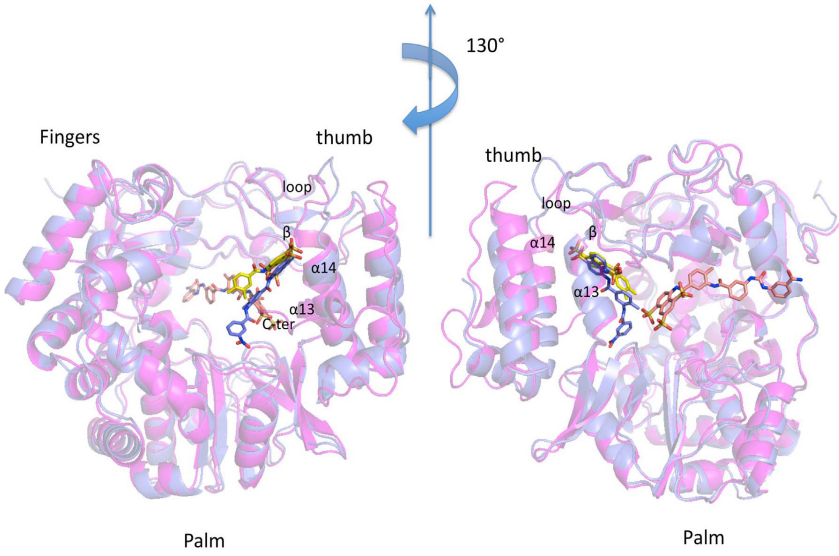

Figure 2. Superposition of hNV and mNV-RdRp/6 complex structures. Superposition of the crystal structures of hNV-RdRp in cartoon (magenta) bound to **6** (yellow carbon atoms) in sticks, onto mNV-RdRp in cartoon (blue), bound to **6** (carbon atoms in green) in sticks. The suramin position (in sticks orange carbons) is obtained from superposition of pdb-id 3UR0 (Mastrangelo et al., 2012) (Figures created using PyMol (http://www.pymol.org)).
doi:10.1371/journal.pone.0091765.g002

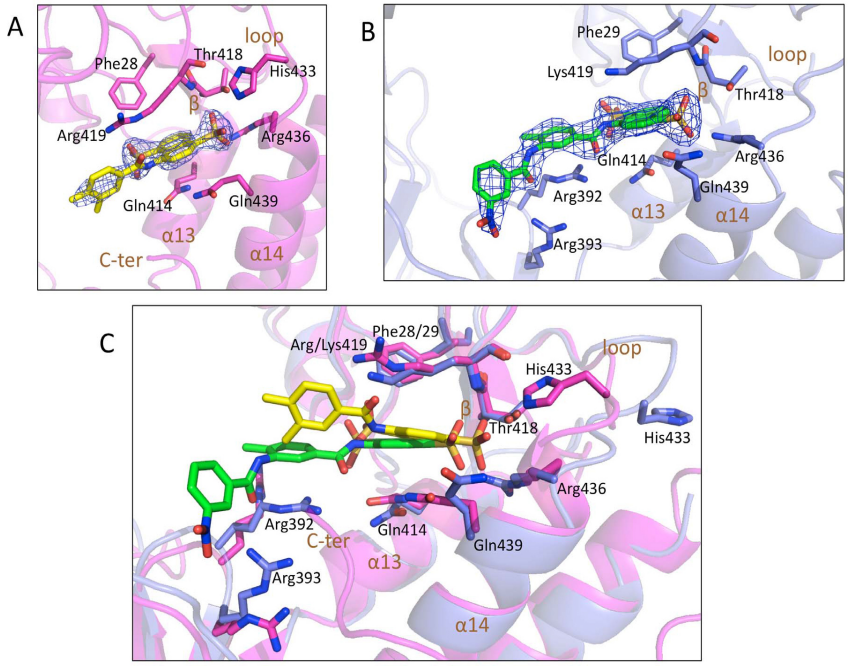

Figure 3. Interaction network of hNV and mNV-RdRp/6 complex. A) Fragment of **6** (carbon atoms in yellow) bound to hNV-RdRp in cartoon (magenta). All the amino acids involved in interaction with the inhibitor molecule are shown in sticks (carbon atoms in magenta). B) **6** (carbon atoms in green) bound to mNV-RdRp in cartoon (blue). All the amino acids (carbon atoms in blue) involved in interaction with the molecule are shown in sticks. 2Fo-Fc electron density contoured at 1 sigma in blue grid. C) Superposition of hNV-RdRp and mNV-RdRp, showing the structures of **6** (carbon atoms in yellow/green, respectively) bound to hNV-RdRp and to mNV-RdRp (cartoon in magenta/blue, respectively). The interacting amino acids are shown in sticks (magenta/blue carbon atoms, respectively).
doi:10.1371/journal.pone.0091765.g003

and mNV-RdRp crystals were soaked in stabilizing solutions of **6** at concentration of 10 or 20 mM (see Materials and Methods for details).

*hNV-RdRp/**6*** diffraction data were collected at 100 K at the ESRF beam line ID29 (Grenoble, France); the crystal structure was solved by molecular replacement (MR) and refined to final crystallographic R-factor/R-free values of 16.4/20.9%, at 2.02 Å resolution (Table 3). After the first refinement cycles residual electron density was visible in a positively charged cleft within the polymerase thumb domain, in a location different from the Suramin binding site [23] (Fig. 2). The naphthalene sulphonate head of **6,** the linked amido group and the phenyl methyl group were accordingly modeled in the new site formed by the α13-β-loop-α14 secondary structure elements (Fig. 2). However, density for the remaining part of the compound was not visible, as confirmed by an independent dataset collected after soaking hNV-RdRp crystals at 20 mM concentration of **6**. The naphthalene ring of **6** is sandwiched between the amido groups of Gln414/Gln439 on one side, and Phe28/Arg419, on the other. The negative charges of the two sulphonates are balanced by residues Arg419, Arg436, and likely (considering that the soaking took place at pH 6) by His433. In particular the sulphonate in position 1 is highly stabilized by an electrostatic interaction network involving the side chains of Thr418, His433, Arg436, and the main chain nitrogen of Arg419 (Fig. 3A). The unmodeled tail of **6** would be hosted in the polar central region of the enzyme which accommodates dsRNA during elongation, wide enough to allow conformational flexibility of the second half of the inhibitor, in keeping with the lack of an interpretable electron density signal.

*mNV-RdRp/**6*** diffraction data were collected at 100 K at the ESRF beam line ID29 (Grenoble, France); the crystal structure was solved by MR (2.3 Å resolution) and refined to final crystallographic R-factor/R-free values of 18.5/24.8% (see Materials and Methods and Table 3). Six mNV-RdRp molecules are hosted in the crystal asymmetric unit. Inspection of the refined model shows that the naphthalene disulphonate head of the inhibitor binds to the same RdRp location identified for hNV-RdRp (Fig. 2). In the murine protein compound **6** could be fully modeled in all the subunits of the crystal asymmetric unit (Fig. 3B).

Relative to the hNV/**6** binding mode described above, in mNV RdRp the naphthalene ring of the molecule is found slightly repositioned, showing a rotation of the naphthalene plane of about 20° toward the palm domain, and a translation away from the α14 helix (by 1.3 Å, Fig. 3C). The observed roto-translation of the ligand is related to the loss of the interaction with Gln439 and with His433, both pointing toward the solvent in mNV RdRp (Fig. 3C). Such shift of the ligand molecule promotes the stacking interaction of the toluene group of **6** with Arg392 guanidine moiety (H-

bonded to **6** carbonyl, and in electrostatic interaction with 2 sulphonates), which allows the stabilization of the entire inhibitor (Fig. 3B, C).

Discussion

For the successful synthesis of sodium sulfates **3**, **6** and **8**, it was crucial to maintain the pH values of the media throughout the entire processes at 4.0 for conversion of **2**→**3**, and at 3.0 for the **4**→**6** and **7**→**8** conversions. An aqueous Na_2CO_3 solution (2.0 M) was frequently added to the reaction mixtures; otherwise, the pH values would be reduced to ~1 during the course of the reactions. High care was taken during the coupling of aniline **7** with triphosgene, which may decompose to an insidious poison phosgene gas during the carbonylation reaction. Accordingly, control of its pH value and addition of a Na_2CO_3 solution were performed in a closed system by a syringe. Although phosgene can be used in the synthesis of urea by reacting with amines [24], two advantages are associated with triphosgene: *i*) being a solid, triphosgene is safer to handle than phosgene, which is a gas or a toluene solution; *ii*) a stoichiometric amount of triphosgene suffices for urea formation, which proceeded in a good yield. Solubility of chemical entities in water plays an important role in their development as a lead for new drugs [24] and is related to the structure–activity relationship. Poor water solubility of a compound may result in decreased oral absorption regardless of its good permeation rate across the intestinal mucosa into the circulation. The apparent partition coefficient (P), which is a useful parameter for understanding the behavior of drug molecules, was measured. Often it is used to predict the distribution of a drug compound in a biological system, the log P value being related to absorption, excretion, and penetration [31]. The measurement of the apparent partition coefficient provides a simple "*in vitro*" method to predict the behavior of a compound in the body and to select the most promising drug candidates from a large pool of ionizable compounds. Thus the log P of thousands of drugs and potential drugs has been measured over the years. Our results presented in Table 1 indicate that the water solubility fell into the range of 114–339 mg/ml for compounds **3**–**8**. Carbamide **8** containing four hydrophilic sulphonate groups was less water soluble than Suramin (114 versus 138 mg/ml), which contained six sulphonate groups. The new **8** also showed a better hydrophobicity than Suramin (log P –1.61 versus –3.42).

It is important to notice that in the DrugBank database (www.http://www.drugbank.ca/), containing 1442 drugs with measured log P between -9 and +10 (average value 2.0, standard deviation 2.2), only 2.1% of the molecules have log P values comprised between −4 and −3, while for 5.6% of the database this value ranges between −1 and −2.

Enzymatic inhibition assays performed on hNV and mNV-RdRps showed that **8** retains potent inhibition activity with IC_{50} values (*ca.* 30 nM for hNV-RdRp and *ca.* 60 nM for mNV) that are fully comparable with those of Suramin reported earlier [23]. Notably, the Suramin IC_{50} values previously reported were crosschecked in the present study, under the experimental conditions here reported, employing the same enzyme preparation used for assaying **6** and **8** inhibitions. The low nanomolar IC_{50} displayed by **8** is in keeping with its close structural relationship with Suramin. Moreover, the observation that **8** inhibitory potency *vs.* NV-RdRps was conserved (relative to Suramin) supports our structure-based hypothesis that the sulphonate group at position 3 of the naphthalene head (removed in **8**) is not involved in the RdRp recognition mechanism. Smaller Suramin-related compounds, isolated during the synthetic steps leading to **8**, were found to be less potent inhibitors, relative to Suramin (**9**) and **8** (Table 2). Nevertheless, the effects exerted to the targeted enzymes were sufficient to drive structural experiments. Since Suramin and **8** showed an almost identical IC_{50} value and close structural formulas, we focused on **6** whose smaller size may allow mapping new regions in the enzyme active site. In particular, **6** is a non-symmetric fragment of **8** hosting only one naphthalene disulphonate head. From a structural viewpoint, **6** can be seen as composed of two distinct parts: the naphthalene disulphonate acid head, which is involved in main interactions with the enzyme at the newly mapped binding site, and the tail region (composed of a toluene and a nitrobenzene ring linked by an amide group), which may provide additional interactions outside the main contact region. Inspection of the crystal structures showed that **6** binds to a site located in the polymerase thumb domain, more specifically in a cleft along the exit path for the newly synthesized RNA. This site doesn't match the previously identified Suramin binding site, but corresponds to the Pyridoxal-5′-phosphate-6-(2′-naphthylazo-6′-nitro-4′,8′-disulphonate; PPNDS) [32], [33] binding site [34](Tarantino *et al.* in press). Notably, PPNDS is also a molecule composed of two parts: the naphthalene disulphonate head and the pyridoxal phosphate group, linked by an azo bridge.

Our analysis on the NV-RdRp/**6** complex crystal structure shows that the sulphonate groups on the naphthalene sulphonic head interact with the RNA binding loop (residues 433–440). The crystal structures of hNV-RdRp/RNA complexes (3BSO and 3H5X) [35], [36] revealed significantly different locations in the RNA-binding loop relative to the free RdRp, showing specific RNA-induced conformational changes of this loop [37]. Binding of compound **6** might freeze the loop in hNV RdRp in the conformation found in the free enzyme hindering efficient RNA binding.

In the hNV-RdRp/**6** complex, the inhibitor electron density fades rapidly after the amido group linked to the naphthalene disulphonate moiety. The latter, in fact, is shifted toward His433 and tilted by steric hindrance with the Gln439/Gln414 "floor" (Fig. 3A,C), thus leaving the unmodeled part of **6** in an open enzyme region that fails to stabilize the ligand in one conformation. Thus, the lower inhibitory potency of **6** *vs.* hNV-RdRp may be linked to failure of establishing enzyme/inhibitor stabilizing interactions along the whole inhibitory molecule, which appears to remain mobile for about 50% of its scaffold.

On the contrary in the mNV-RdRp/**6** structure, the inhibitor could be completely modeled thanks to the different disposition of the naphthalene head due to the loss of the interaction with His433. The new interactions of **6** with Arg392 and Arg393 are in agreement with the higher potency of **6** *vs.* mNV-RdRp relative to hNV-RdRp. In contrast, **8** shows a slightly lower inhibitory effect on mNV relative to hNV-RdRp as observed for Suramin, probably because it binds to the same binding site of the latter inhibitor, achieving a different interaction network with the protein. The current crystal structure data, available only for the mNV-RdRp/Suramin complex (Mastrangelo *et al.*,2012) do not allow further comparisons.

The newly discovered NV-RdRP inhibitor binding site, mapped by **6** and by PPNDS, together with the different conformational behaviors displayed by **6** bound to hNV and mNV-RdRps, appear as two novel structural grounds to be exploited for the design and development of more potent/selective hNV-RdRp inhibitors.

Conclusions

This study presented the design and synthesis of a modified Suramin molecule (**8**), the crystal structure analyses of NV-RdRps

in complexes with a Suramin fragment (**6**), and the evaluation of inhibitory parameters for five related compounds targeting mNV and hNV-RdRps. A total synthesis of **8** from commercially available reagents was accomplished, which involved five steps with a 45% overall yield. In comparison with Suramin (**9**) bearing six hydrophilic sulphonate groups, the new and symmetric **8** contains four sulphonate groups, and exhibits the same potency as Suramin against NV-RdRps. However, its water solubility and log *P* value are more favorable compared to Suramin. In contrast, the tested reaction intermediates proved less effective in inhibiting NV polymerases.

Analysis of the crystal structures of hNV-RdRp/**6** complexes provided a mechanistic explanation of the decreased potency displayed by this compound. In fact, although the inhibitor naphthalene disulphonate 'head' is strongly bound to a specific pocket in the hNV-RdRp thumb domain, the rest of the molecule is hardly involved in enzyme/inhibitor interactions, negatively affecting **6** affinity for the polymerase active region. On the contrary, the higher inhibitory potency of **6** against mNV-RdRp correlates with a fully defined binding mode and interactions of the inhibitor to the RdRp active site. It may be noted that the related PPNDS NV-RdRp inhibitor, which displays a lower molecular weight and an overall more rigid structure, while adopting the same binding mode for the naphthalene disulphonate moiety, is involved in strong interactions with the enzyme in the naphthalene disulphonate substituent region, and displays low nM inhibitory potency [34] (Tarantino *et al.*, in press). The basic structural and functional knowledge here reported for Suramin fragments, and particularly for **6**, will guide further Suramin chemical modifications aimed at the identification of hNV-RdRp inhibitors potentially able to be developed as anti-Norovirus agents.

Materials and Methods

General Procedure

All reactions were carried out in oven-dried glassware (120 °C) under an atmosphere of nitrogen unless otherwise indicated. Acetone, diethylether, toluene, acetic acid, and methanol were purchased from Mallinckrodt Chemical Co. 4-Amino-1,5-naphthalenesulphonate acid monosodium salt and triphosgene were purchased from TCI Chemical Co. 4-Methyl-3-nitrobenzoyl chloride was purchased from Sigma–Aldrich Chemical Co. Pd/C (10%) was purchased from Alfa Aesar Chemical Co. 3-Nitrobenzoyl chloride was purchased from Across Organics Chemical Co. Analytical thin layer chromatography (TLC) was performed on precoated plates (silica gel 60 F–254), purchased from Merck Inc. High performance liquid chromatography (HPLC) was performed on two Waters 515 HPLC Pumps equipped with a Waters 2489 UV/Visible Detector and a Thermo 5 μm Hypersil ODS (250×4.6 mm D.I.). Purity of products **3**, **4**, **6**, **7**, and **8** was >98.0%, as checked by HPLC. Infrared (IR) spectra were measured on a Perkin–Elmer model spectrum one B spectrophotometer and Perkin–Elmer Spectrum 100 FT-IR Spectrometer. Absorption intensities are recorded by the following abbreviations: s, strong; m, medium; w, weak. Proton NMR spectra were obtained on a Varian Mercury-400 (400 MHz) spectrometer or a Bruker AV-400 (400 MHz) by use of DMSO-d_6 as solvent. Proton NMR chemical shifts are referenced to the DMSO-d_6 quintet (δ 2.49 ppm). Carbon-13 NMR spectra were obtained on a Varian Mercury-400 (100 MHz) spectrometer or a Bruker AV-400 (100 MHz) by use of DMSO-d_6 as solvent. Carbon-13 chemical shifts are referenced to the center of the DMSO-d_6 septet (δ 39.5 ppm). Multiplicities are recorded by the following abbreviations: s, singlet; d, doublet; t, triplet; q, quartet; m, multiplet; J, coupling constant (hertz). High-resolution mass spectra were obtained by means of a VARIAN-901 mass spectrometer.

4-(4-Methyl-3-nitrobenzamido)naphthalene-1,5-disulphonate Acid Disodium Salt (3)

4-Amino-1,5-naphthalenedisulphonate acid monosodium salt (**2**, 0.998 g, 3.07 mmol, 1.0 equiv) was dissolved in water (12 ml) and the pH was adjusted to 4.0 by addition of aqueous Na_2CO_3 solution (2.0 M). To this solution 4-methyl-3-nitrobenzoyl chloride (**1**, 0.863 g, 4.33 mmol, 1.4 equiv) in toluene (2.7 ml) was slowly added. Its pH value was maintained continuously at 4.0 by addition of aqueous Na_2CO_3 solution (2.0 M). After the reaction mixture was stirred at room temperature for 12 hours, the toluene layer was separated out and the pH value of the aqueous layer was adjusted to 2.0. The aqueous layer was washed with diethyl ether (4×10 ml) and then pH was adjusted to 7.0 by addition of aqueous Na_2CO_3 solution (2.0 M). The water was removed under vacuum at 45 °C to give a crude solid, which was then dissolved in boiling methanol followed by hot filtration. The residue was dried over P_2O_5 under vacuum to give **3** (1.27 g, 2.49 mmol) in 81% yield, as a pale yellow powder: ^{1}H NMR (DMSO-d_6, 400 MHz) δ 12.81 (s, 1 H, NH), 9.10 (d, J = 8.8 Hz, 1 H, ArH), 8.66 (s, 1 H, ArH), 8.38 (d, J = 8.0 Hz, 1 H, ArH), 8.29 (d, J = 8.0 Hz, 1 H, ArH), 8.03-8.02 (m, 2 H, ArH), 7.66 (d, J = 8.0 Hz, 1 H, ArH), 7.47 (t, J = 8.0 Hz, 1 H, ArH), 2.60 (s, 3 H, CH_3); ^{13}C NMR (DMSO-d_6, 100 MHz) δ 163.32 (C = O), 148.71, 141.65, 141.56, 135.61, 134.72, 133.70, 132.76, 132.32, 131.56, 130.83, 127.20, 124.46, 123.99, 123.54, 123.44, 122.51, 19.52; IR (KBr) 3359 (br, NH), 2918 (s), 1647 (m, C = O), 1547 (m), 1522 (m), 1346 (m), 1195 (s), 1044 (m) cm^{-1}; MS (ESI) m/z $(M+Na)^+$ 533, $(M+H)^+$ 511; HRMS (ESI) calc. for $(C_{18}H_{12}N_2Na_2O_9S_2+H)^+$: 510.9858, found 510.9845.

4-(3-Amino-4-methylbenzamido)naphthalene-1,5-disulphonate Acid Disodium Salt (4)

Nitro compound **3** (0.404 g, 0.792 mmol, 1.0 equiv) was dissolved in water (5.0 ml), to which 10% Pd/C (20.0 mg, 5.0% weight of **3**) was added. After the reaction mixture was stirred at room temperature for 12 hours under H_2 atmosphere (4.0 bar), the Pd/C was filtered off by use of celite pad. Water was removed under vacuum at 45 °C to give a crude solid, which was then dissolved in boiling methanol followed by hot filtration. The residue was dried over P_2O_5 under vacuum to give **4** (0.347 g, 0.722 mmol) in 91% yield, as a brown powder: ^{1}H NMR (DMSO-d_6, 400 MHz) δ 12.37 (s, 1 H, NH), 9.08 (d, J = 8.4 Hz, 1 H, ArH), 8.29 (d, J = 7.2 Hz, 1 H, ArH), 8.03 (d, J = 8.4 Hz, 1 H, ArH), 7.97 (d, J = 8.4 Hz, 1 H, ArH), 7.46 (t, J = 8.4 Hz, 1 H, ArH), 7.31–7.28 (m, 2 H, ArH), 7.01 (d, J = 7.6 Hz, 1 H, ArH), 5.06 (br, 2 H, NH_2), 2.12 (s, 3 H, CH_3); ^{13}C NMR (DMSO-d_6, 100 MHz) δ 166.25 (C = O), 146.14, 141.89, 140.74, 134.85, 134.14, 131.56, 130.61, 129.32, 126.85, 124.48, 124.33, 123.42, 123.31, 122.10, 115.94, 113.93, 17.44; IR (KBr) 3445 (br, NH), 2918 (w), 1652 (m, C = O), 1575 (s), 1546 (s), 1525 (s), 1414 (m), 1344 (m), 1193 (s), 1073 (w), 1044 (s), 847 (w) cm^{-1}; MS (ESI) m/z $(M+Na)^+$ 503, $(M+H)^+$ 481; HRMS (ESI) calcd for $(C_{18}H_{14}N_2Na_2O_7S_2+H)^+$: 481.0116, found 481.0115.

4-[4-Methyl-3-(3-nitrobenzamido)benzamido]naphthalene-1,5-disulsulphonate Acid Disodium Salt (6)

Aniline derivative **4** (0.197 g, 0.410 mmol, 1.0 equiv) was dissolved in water (3.0 ml) and the pH was adjusted to 3.0 by

addition of aqueous CH_3CO_2H solution. To this solution *m*-nitrobenzoyl chloride (**5**, 0.110 g, 0.593 mmol, 1.43 equiv) in toluene (0.60 ml) was slowly added. Its pH value was maintained again at 3.0 by addition of aqueous Na_2CO_3 solution (2.0 M). After the reaction mixture was stirred at room temperature for 12 hours, the toluene layer was separated out and the pH value of the aqueous layer was adjusted to 2.0. The aqueous layer was washed with diethyl ether (4×5 ml) and then pH was adjusted to 7.0 by addition of aqueous Na_2CO_3 solution (2.0 M). Water was removed under vacuum at 45 °C to give a crude solid, which was then dissolved in boiling methanol followed by hot filtration. The residue was dried over P_2O_5 under vacuum to give **6** (0.212 g, 0.337 mmol) in 82% yield as a yellow powder: ^{1}H NMR (DMSO-d_6, 400 MHz) δ 12.62 (s, 1 H, NH), 10.59 (s, 1 H, NH), 9.09 (d, J = 8.4 Hz, 1 H, ArH), 8.85 (s, 1 H, ArH), 8.50 (d, J = 8.0 Hz, 1 H, ArH), 8.45 (d, J = 8.4 Hz, 1 H, ArH), 8.29 (d, J = 7.2 Hz, 1 H, ArH), 8.05–7.99 (m, 4 H, ArH), 7.85 (t, J = 8.0 Hz, 1 H, ArH), 7.46 (t, J = 8.4 Hz, 1 H, ArH), 7.41 (d, J = 8.0 Hz, 1 H, ArH), 2.32 (s, 3 H, CH_3); ^{13}C NMR (DMSO-d_6, 100 MHz) δ 64.93 (C = O), 163.30 (C = O), 147.82, 141.74, 141.11, 137.40, 137.38, 135.77, 134.36, 134.17, 133.71, 131.56, 130.71, 130.24, 130.04, 127.01, 126.78, 126.17, 125.87, 124.49, 123.46, 123.42, 122.55, 122.36, 18.03; IR (KBr) 3467 (br, NH), 1657 (m, C = O), 1580 (s), 1531 (m), 1417 (m), 1227 (m), 1190 (m), 1040 (m), 835 (w) cm^{-1}; MS (ESI) m/z $(M+Na)^+$ 652, $(M+H)^+$ 630; HRMS (ESI) calcd for $(C_{25}H_{17}N_3Na_2O_{10}S_2+H)^+$: 630.0229, found 630.0223.

4-[3-(3-Aminobenzamido)-4-methylbenzamido]naphthalene-1,5-disulphonate Acid Disodium Salt (7)

Nitro compound **6** (0.103 g, 0.164 mmol, 1.0 equiv) was dissolved in water (2.0 ml), to which 10% Pd/C (5.0 mg, 5.0% weight of **6**) was added. After the reaction mixture was stirred at room temperature for 12 hours under H_2 atmosphere (4.0 bar), the Pd/C was filtered off by use of celite pad. Water was removed under vacuum at 45 °C to give a crude solid, which was then dissolved in boiling methanol followed by hot filtration. The residue was dried over P_2O_5 under vacuum to give **7** (89.1 mg, 0.148 mmol) in 90% yield, as a brown powder: ^{1}H NMR (DMSO-d_6, 400 MHz) δ 12.60 (s, 1 H, NH), 9.85 (s, 1 H, NH), 9.09 (d, J = 8.4 Hz, 1 H, ArH), 8.29 (d, J = 7.2 Hz, 1 H, ArH), 8.04–7.99 (m, 3 H, ArH), 7.96 (s, 1 H, ArH), 7.45 (t, J = 8.0 Hz, 1 H, ArH), 7.36 (d, J = 8.0 Hz, 1 H, ArH), 7.17 (s, 1 H, ArH), 7.14–7.13 (m, 2 H, ArH), 6.76–6.73 (m, 1 H, ArH), 5.30 (br, 2 H, NH_2), 2.31 (s, 3 H, CH_3); ^{13}C NMR (DMSO-d_6, 100 MHz) δ 166.18 (C = O), 165.13 (C = O), 148.81, 141.76, 141.03, 137.19, 136.52, 135.38, 134.48, 133.56, 131.58, 130.72, 129.86, 128.78, 127.04, 126.65, 125.30, 125.27, 124.55, 123.48, 122.38, 116.81, 114.78, 113.18, 18.03; IR (KBr) 3356 (br, NH), 3001 (w), 1575 (s), 1423 (m), 1335 (w), 1316 (w), 1223 (m), 1204 (m), 1190 (m), 1042 (m), 836 (w) cm^{-1}; MS (ESI) m/z $(M+Na)^+$ 622, $(M+H)^+$ 600; HRMS (ESI) calcd for $(C_{25}H_{19}N_3Na_2O_8S_2+H)^+$: 600.0487, found 600.0487.

4-4′-(Carbonylbis[imino-3,1-phenylenecarbonylimino(4-methyl-3,1-phenylene) carbonylimino])bis-1,5-naphthalenedisulphonate Acid Tetrasodium Salt (8)

Aniline derivative **7** (49.4 mg, 82.4 µmol, 2.0 equiv) was dissolved in water (2.0 ml) and the pH was adjusted to 3.0 by addition of aqueous Na_2CO_3 solution (2.0 M). To this solution triphosgene (33.0 mg, 0.111 mmol, 1.3 equiv) in toluene (0.50 ml) was slowly added. Its pH value was maintained again at 3.0 by addition of aqueous Na_2CO_3 solution (2.0 M). After the reaction mixture was stirred at room temperature for 12 hours, the toluene layer was discarded. Water was removed under vacuum at 45 °C to give a crude solid, which was then dissolved in boiling methanol followed by hot filtration. The residue was dried over P_2O_5 under vacuum to give **8** (42.4 mg, 34.0 µmol) in 83% yield as a white powder: ^{1}H NMR (DMSO-d_6, 400 MHz) δ 12.60 (s, 2 H, NH), 11.08 (s, 2 H, NH), 10.07 (s, 2 H, NH), 9.09 (d, J = 8.4 Hz, 2 H, ArH), 8.29 (d, J = 7.2 Hz, 2 H, ArH), 8.10 (s, 2 H, ArH), 8.057.98 (m, 8 H, ArH), 7.82 (d, 2 H, J = 8.8 Hz, ArH), 7.57 (d, J = 8.0 Hz, 2 H, ArH), 7.45 (t, J = 8.0 Hz, 2 H, ArH), 7.41–7.37 (m, 4 H, ArH), 2.32 (s, 6 H, 2×CH_3); ^{13}C NMR (DMSO-d_6, 100 MHz) δ 165.81 (C = O), 165.06 (C = O), 153.53 (C = O), 141.76, 141.10, 137.18, 136.43, 135.17, 134.42, 133.60, 131.57, 130.72, 129.89, 128.48, 127.01, 126.60, 125.32, 124.51, 123.47, 123.41, 122.36, 121.10, 120.19, 117.60, 114.19, 18.06; IR (KBr) 3355 (br, NH), 2919 (s), 2848 (m), 1652 (s, C = O), 1634 (s, C = O), 1574 (m), 1422 (m), 1318 (m), 1224 (w), 1191 (w), 1086 (w), 1039 (w), 828 (w) cm^{-1}; MS (ESI) m/z $(M+2\ Na)^{2+}$ 635; HRMS (ESI) calcd for $(C_{51}H_{36}N_6Na_4O_{17}S_4+2\ Na)^{2+}$: 635.0197, found 635.0116.

Water Solubility

A stock solution was prepared by dissolving a precisely weighed amount of Suramin derivatives in deionized water (1.0 ml). The UV absorption maximum of each compound was measured by dilution of the solution with deionized water as necessary. A saturated solution of each compound was then prepared by use of deionized water (1.0 ml) in the presence of an excess of Suramin derivatives for 1.0 hour. The obtained saturated solution was filtered to remove solid compound through a Millipore filter (0.45 µm) and was scanned by UV spectroscopy at the wavelength of the absorption maximum previously determined.

Partition Coefficient

The *n*-octanol/water partition coefficient of Suramin derivatives was determined by the shake-flask method. *n*-Octanol and pH 7.4 phosphate buffer were mutually saturated for 4.0 hours, and the phases were separated. A stock solution of each Suramin derivative was prepared using pH 7.4 phosphate buffer solution. Suramin derivatives were partitioned between *n*-octanol and pH 7.4 phosphate buffer. Then the phase mixtures were shaken for 1 hour at constant 25 °C. After separation, the absorbance of the phosphate buffer solutions (pH 7.4) was measured by UV spectrophotometry. Three replicates were performed for each compound. The *P* value corresponded to the quotient between *n*-octanol and buffer concentrations of the drug. The log *P* values were an average of three independent experiments.

Expression and purification of the hNV and mNV-RdRps

The NV-RdRps were expressed and purified as previously described [23], and stocked in 25 mM Tris/HCl pH 7.4, 1 mM DTT, 100 mM NaCl, 1 mM EDTA. Data and/or materials of NV-RdRps are available for sharing or collaboration following signing of a material transfer agreement with Riboxx GmbH (Germany).

In-vitro RdRp inhibition assays

RdRp assays were performed as previously described [23]. In brief poly(C) (MP Biomedicals) was used as template annealed with oligoG12 as primer (62.5 nM final concentration) and GTP (100 µM final concentration) as substrate, in a 200 µl reaction mixture containing 20 mM Tris/HCl pH 7.5, 25 mM NaCl, 5 mM $MgCl_2$, 0.3 mM $MnCl_2$, 1 mM DTT, PicoGreen Quantitation Reagent (Molecular Probes) diluted 1/200 20 U ml−1 RiboLock Ribonuclease Inhibitor (Fermentas). Reactions were

started by the addition of GTP following the fluorescence of samples in a fluorescence reader (Varian, Cary Eclipse Fluorescence Spectrophotometer).

Thermofluorometric characterization of the hNV-RdRp inhibitors interaction

Thermofluorimetric (Thermal shift) assays for the evaluation of the hNV-RdRp melting temperature (T_m) in the absence/presence of the inhibitors, were conducted in a MiniOpticon Real Time PCR Detection System (Bio-Rad), using the fluorescent dye Sypro Orange. Solutions of 4 µl of the NV-RdRp domain (final hNV-RdRp concentration 7 µM, final mNV-RdRp concentration 1.6 µM) were diluted in 9.5 µl of its buffer, and mixed with 3.5 µl of Sypro orange (Sigma) diluted 60×, and 1 µl of **6** or **8** (4 µM final concentration). In control samples the inhibitors were replaced by water. The sample plates were heated from 20 to 90°C with a heating rate of 0.2 °C/min. Fluorescence intensities were measured within excitation/emission ranges of 470–505 nm and 540–700 nm, respectively.

Crystallization of the NV-RdRps in presence of 6

Sitting drop crystallization experiments on hNV-RdRp (11 mg/ml) were prepared using an Oryx-8 crystallization robot (Douglas Instruments, East Garston, UK), from a 50% mixture of the protein with the reservoir solution (final drop volume 0.3 µl). Crystals were obtained after 4 weeks at 20°C, in 1.2 M Na citrate, 100 mM Na cacodylate pH 6.2, and NaCl 125 mM. Before X-ray data collection, crystals were soaked in a cryoprotectant solution (1.4 M Na citrate, 100 mM Na cacodylate pH 6.2, and 25% glycerol) with 10 mM **6**, in the presence of 62.5 nM dsRNA and 100 µM GTP for 36 hours, then flash-cooled in liquid nitrogen. The hNV-RdRp/**6** crystals diffracted to a maximum resolution of 2.02 Å at the ESRF Synchrotron (Grenoble, France) beam line ID29. X-ray diffraction data were indexed using MOSFLM [38], and intensities were merged using SCALA [39]. Microbatch crystallization experiments on mNV-RdRp were prepared using an Oryx-8 crystallization robot (Douglas Instruments, East Garston, UK), from a 2:1:1 mixture (drop volume 0.4 µl) of protein (10 mg/ml), precipitant, and 100 mM $MgCl_2$ (25 mM in the drop), covered by Al's oil (a mixture of 50% Paraffin oil and 50% Silicon oil). Prismatic crystals of approximately $150\times80\times30$ µm^3 were obtained after 1 week at 20°C, in 1.6 M $(NH_4)_2SO_4$, 12% glycerol, 100 mM TRIS-HCl pH 8.4. Before X-ray data collection, crystals were soaked in a cryoprotectant solution (1.8 M $(NH_4)_2SO_4$, 100 mM TRIS-HCl pH 8.4, and 25% glycerol) with 20 mM of **6**, in the presence of 62.5 nM of dsRNA and 100 µM of GTP for 36 hours, than flash-cooled in liquid nitrogen. dsRNA and GTP were added to the soaking solution as additives to increase chances to obtain ligand-protein complexes The mNV-RdRp/**6** crystals diffracted to a maximum resolution of 2.3 Å at the ESRF Synchrotron (Grenoble, France) beam line ID29. X-ray diffraction data were indexed using MOSFLM, and intensities were merged using SCALA [39].

Structure determination and refinement

The three-dimensional structures of hNV-RdRp and mNV-RdRp in the complexes with **6** were solved by the Molecular Replacement method using the program MOLREP [40] and as search models the 3D structures of the respective ligand-free RdRps (PDB-id 2B43 and id 3UQS, respectively). The crystal asymmetric unit molecule(s) were individually subjected to rigid-body refinement, and subsequently to restrained refinement using REFMAC5 [41]. A random set comprising 5% of the data was omitted from refinement for R-free calculation. Manual rebuilding with COOT [42] and additional refinement with BUSTER [43] and REFMAC5 were subsequently performed, as needed. Data collection, refinement statistics as well as stereochemical quality of the models are summarized in Table 3. Atomic coordinates and structure Factor files for hNV-RdRp/**6** and mNV-RdRp/**6** complexes have been deposited with the Protein Data Banks as entries 4NRT and 4NRU, respectively.

Acknowledgments

With respect to norovirus RNA dependent RNA polymerase used in this study, data and/or materials are available for sharing or collaboration following signing of a material transfer agreement with Riboxx GmbH (Germany).

Author Contributions

Conceived and designed the experiments: MM MP ST DT EM JR JH MB. Performed the experiments: RC MP DT RS JR YT. Analyzed the data: MM MP DT EM ST JH RC. Contributed reagents/materials/analysis tools: JH MB JR. Wrote the paper: RC MP DT MM ST EM MB.

References

1. Clarke IN, Lambden PR (1997) The molecular biology of caliciviruses. J Gen Virol 78 (Pt 2): 291–301.
2. Patel MM, Widdowson M-A, Glass RI, Akazawa K, Vinjé J, et al. (2008) Systematic literature review of role of noroviruses in sporadic gastroenteritis. Emerg Infect Dis 14: 1224–1231.
3. Atmar RL, Estes MK (2012) Norovirus vaccine development: next steps. Expert Rev vaccines 11: 1023–1025.
4. Bartsch SM, Lopman BA, Hall AJ, Parashar UD, Lee BY (2012) The potential economic value of a human norovirus vaccine for the United States. Vaccine 30: 7097–7104.
5. Cheetham S, Souza M, Meulia T, Grimes S, Han MG, et al. (2006) Pathogenesis of a genogroup II human norovirus in gnotobiotic pigs. J Virol 80: 10372–10381.
6. Souza M, Cheetham SM, Azevedo MSP, Costantini V, Saif LJ (2007) Cytokine and antibody responses in gnotobiotic pigs after infection with human norovirus genogroup II.4 (HS66 strain). J Virol 81: 9183–9192.
7. Bok K, Parra GI, Mitra T, Abente E, Shaver CK, et al. (2011) Chimpanzees as an animal model for human norovirus infection and vaccine development. Proc Natl Acad Sci United States Am 108: 325–330.
8. Karst SM (2010) Pathogenesis of noroviruses, emerging RNA viruses. Viruses 2: 748–781.
9. Clarke IN, Lambden PR (2000) Organization and expression of calicivirus genes. J Infect Dis 181.
10. Hansman GS, Matsubara N, Oka T, Ogawa S, Natori K, et al. (2005) Deletion analysis of the sapovirus VP1 gene for the assembly of virus-like particles. Arch Virol 150: 2529–2538.
11. Hansman GS, Jiang XJ, Green KY (2010) Caliciviruses: Molecular and Cellular Virology. Caister Academic Press.
12. Fullerton SWB, Blaschke M, Coutard B, Gebhardt J, Gorbalenya A, et al. (2007) Structural and functional characterization of sapovirus RNA-dependent RNA polymerase. J Virol 81: 1858–1871.
13. Hawking F (1978) Suramin: with special reference to onchocerciasis. Adv Pharmacol Chemother 15: 289–322.
14. Mitsuya H, Matsushita S, Yarchoan R, Broder S (1984) Protection of T cells against infectivity and cytopathic effect of HTLV-III in vitro. Princess Takamatsu Symp 15: 277–288.
15. Dunn PM, Blakeley AG (1988) Suramin: a reversible P2-purinoceptor antagonist in the mouse vas deferens. Br J Pharmacol 93: 243–245.
16. Kassack MU, Braun K, Ganso M, Ullmann H, Nickel P, et al. (2004) Structure-activity relationships of analogues of NF449 confirm NF449 as the most potent and selective known P2X1 receptor antagonist. Eur J Med Chem 39: 345–357.
17. Zamai M, Hariharan C, Pines D, Safran M, Yayon A, et al. (2002) Nature of Interaction between basic fibroblast growth factor and the antiangiogenic drug 7,7-(carbonyl-bis[imino-N-methyl-4,2-pyrrolecarbonylimino[N-methyl-4,2-pyrrole]-carbonylimino])-bis-(1,3-naphtalene disulfonate). II. Removal of polar interactions affects protein folding. Biophys J 82: 2652–2664.

18. Sola F, Farao M, Pesenti E, Marsiglio A, Mongelli N, et al. (1995) Antitumor activity of FCE 26644 a new growth-factor complexing molecule. Cancer Chemother Pharmacol 36: 217–222.
19. Jagielski AK, KryÂ>kiewicz E, BryÂ'a J (2006) Suramin-induced reciprocal changes in glucose and lactate synthesis in renal tubules contribute to its hyperglycaemic action. Eur J Pharmacol 537: 205–209.
20. Kaur M, Reed E, Sartor O, Dahut W, Figg WD (2002) Suramin's development: what did we learn? Investig new drugs 20: 209–219.
21. Lustberg MB, Pant S, Ruppert AS, Shen T, Wei Y, et al. (2012) Phase I/II trial of non-cytotoxic suramin in combination with weekly paclitaxel in metastatic breast cancer treated with prior taxanes. Cancer Chemother Pharmacol 70: 49–56.
22. Kaplan LD, Wolfe PR, Volberding PA, Feorino P, Levy JA, et al. (1987) Lack of response to suramin in patients with AIDS and AIDS-related complex. Am J Med 82: 615–620.
23. Mastrangelo E, Pezzullo M, Tarantino D, Petazzi R, Germani F, et al. (2012) Structure-based inhibition of Norovirus RNA-dependent RNA polymerases. J Mol Biol 419: 198–210.
24. Thomas G (n.d.) Medicinal chemistry. Chichester; Hoboken, NJ: John Wiley.
25. Camp D, Davis RA, Campitelli M, Ebdon J, Quinn RJ (2012) Drug-like properties: guiding principles for the design of natural product libraries. J Nat Prod 75: 72–81.
26. Padiya KJ, Gavade S, Kardile B, Tiwari M, Bajare S, et al. (2012) Unprecedented "In Water" imidazole carbonylation: paradigm shift for preparation of urea and carbamate. Org Lett 14: 2814–2817.
27. Bookser BC, Ugarkar BG, Matelich MC, Lemus RH, Allan M, et al. (2005) Adenosine kinase inhibitors. 6. Synthesis, water solubility, and antinociceptive activity of 5-phenyl-7-(5-deoxy-beta-D-ribofuranosyl)pyrrolo[2,3-d]pyrimidines substituted at C4 with glycinamides and related compounds. J Med Chem 48: 7808–7820.
28. Kraszni M, Bányai I, Noszál B (2003) Determination of conformer-specific partition coefficients in octanol/water systems. J Med Chem 46: 2241–2245.
29. Lee S, Cho K-H, Acree WE, No KT (2012) Development of surface-SFED models for polar solvents. J Chem Inf Model 52: 440–448.
30. Eltahla AA, Lackovic K, Marquis C, Eden J-S, White PA (2013) A fluorescence-based high-throughput screen to identify small compound inhibitors of the genotype 3a hepatitis C virus RNA polymerase. J Biomol Screen 18: 1027–1034.
31. Pinnen F, Cacciatore I, Cornacchia C, Sozio P, Iannitelli A, et al. (2007) Synthesis and study of L-dopa-glutathione codrugs as new anti-Parkinson agents with free radical scavenging properties. J Med Chem 50: 2506–2515.
32. Wood CR, Hennessey TM (2003) PPNDS is an agonist, not an antagonist, for the ATP receptor of Paramecium. J Exp Biol 206: 627–636.
33. Suzuki E, Kessler M, Montgomery K, Arai AC (2004) Divergent effects of the purinoceptor antagonists suramin and pyridoxal-5′-phosphate-6-(2′-naphthylazo-6′-nitro-4′,8′-disulfonate) (PPNDS) on alpha-amino-3-hydroxy-5-methyl-4-isoxazolepropionic acid (AMPA) receptors. Mol Pharmacol 66: 1738–1747.
34. Tarantino D, Pezzullo M, Mastrangelo E, Croci R, Rohayem J, et al. (2013) Naphtalene-sulfonate inhibitors of human norovirus RNA-dependent RNA-polymerase. Antivir Res.
35. Zamyatkin DF, Parra F, Alonso JMM, Harki DA, Peterson BR, et al. (2008) Structural insights into mechanisms of catalysis and inhibition in Norwalk virus polymerase. J Biol Chem 283: 7705–7712.
36. Zamyatkin DF, Parra F, MachÂ-n A, Grochulski P, Ng KK-S (2009) Binding of 2′-amino-2′-deoxycytidine-5′-triphosphate to norovirus polymerase induces rearrangement of the active site. J Mol Biol 390: 10–16.
37. Lee J-H, Alam I, Han KR, Cho S, Shin S, et al. (2011) Crystal structures of murine norovirus-1 RNA-dependent RNA polymerase. J Gen Virol 92: 1607–1616.
38. Leslie AG, Powell HR (2007) Processing diffraction data with Mosflm. Evolving methods for macromolecular crystallography. Springer. pp. 41–51.
39. Evans P (2006) Scaling and assessment of data quality. Acta Crystallogr D Biol Crystallogr 62: 72–82.
40. Vagin A, Teplyakov A (2010) Molecular replacement with MOLREP. Acta Crystallogr D Biol Crystallogr 66: 22–25.
41. Steiner RA, Lebedev AA, Murshudov GN (2003) Fisher's information in maximum-likelihood macromolecular crystallographic refinement. Acta Crystallogr D Biol Crystallogr 59: 2114–2124.
42. Emsley P, Lohkamp B, Scott WG, Cowtan K (2010) Features and development of Coot. Acta Crystallogr D Biol Crystallogr 66: 486–501.
43. Smart OS, Womack TO, Flensburg C, Keller P, Paciorek W, et al. (2012) Exploiting structure similarity in refinement: automated NCS and target-structure restraints in BUSTER. Acta Crystallogr D Biol Crystallogr 68: 368–380.

PART III

7. Introduction to another approach to find antivirals: *in vitro* cell-based assay

Over the past years, there has been a growing trend toward the use of cell-based assays, in particular for pharmaceutical research and drug development. Cell-based assays refer to the use of living cells as discovery tools. This includes a variety of assays that measure cell proliferation, toxicity, motility and morphology. Insights from such cellular assays have been shown to facilitate drug discovery, saving considerable time and cutting costs.

The cell-based assays applied to antiviral research offer a broad range of applications:

- To discover compounds with antiviral activity using cell-culture based assays for virus replication
- To validate activity of hit compounds delivered, and support the hit-to-lead optimization process
- To identify targets and unravel mechanisms of action of newly discovered antiviral inhibitors.

To test PPNDS on mNV and other compounds on Flaviviruses and Coronaviruses, I spent two months of my PhD at The Catholic University Leuven (KU, Leuven, Belgium) at the Department of Virology, in Prof. Johan Neyts' lab, a partner in the SILVER project.

7.1 Cell-base assays with PPNDS and PPNDS in liposomes

A liposome is a spherical vesicle whose membrane is composed of a phospholipid bilayer, which is used to deliver drugs or genetic materials into cells (Figure 27).

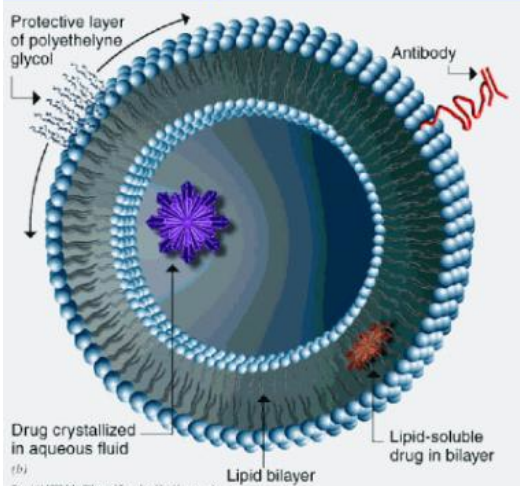

Fig 27. Schematic reconstruction of a liposome. Different types of liposomes, according to their specific use, can be designed. They can be composed of naturally-derived phospholipids with mixed lipid chains.

The liposome is a drug carrier system, which is particularly attractive when it is composed of natural phospholipids that are well tolerated and have minimal toxic side effects. The main objectives of using liposomes as drug delivery systems are to increase (formally) the solubility and the stability of drugs *in vivo*, to reduce toxicity, and to achieve drug targeting [84]. The association of drugs with liposomes has major effects on their pharmacokinetics: liposomes improve drug bioavailability and provide targeted drug delivery to the site of action [85]. Thus, liposomal formulations have resulted in increased therapeutic efficacy for a variety of substances in areas such as cancer [86], antimicrobial [87], and antiparasite therapy [88]; [89]; [90]; [91].

Prof. Nastruzzi from the University of Ferrara (Italy) prepared different compositions of liposomes with and without PPNDS. I tested the different liposome preparations adding them to RAW 264.7 cell cultures that

were uninfected or infected with mNV, and I analysed the results using the MTS assay (see *Cell-based assay Materials and Methods* paragraph) (Figure 28).

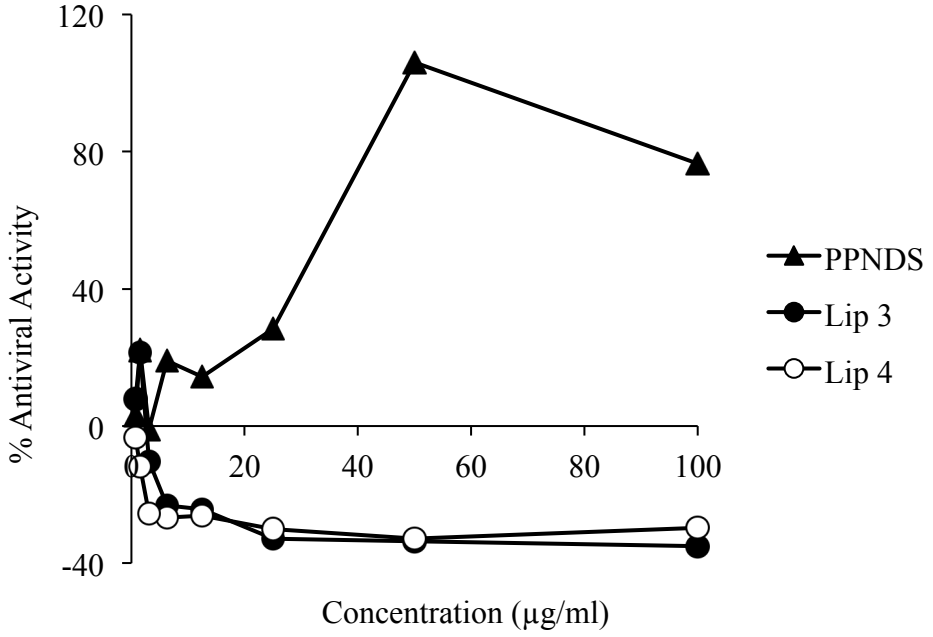

Fig 28. Antiviral activity (%) *vs* compound concentrations. PPNDS implies the free PPNDS compound; Lip 3 stands for PC 9 mM – DDAB 1 mM – PPNDS 0.1 mM; Lip 4 stays for PC 9 mM – DDAC 1 mM – PPNDS 0.1 mM (PC=phosphatidylcholine;DDAB=Dimethyldioctadecylammoniumbromide;DDAC=Dimethyldioctadecylammoniumchloride).

Lip 3, Lip 4 and PPNDS are not toxic (data not shown) on the RAW 264.7 cell line. However, PPNDS-liposome formulations seem to be not active. In contrast, free PPNDS is active with an EC_{50} of 43.7 µM. Following these preliminary results, other experiments are ongoing to further characterize the compound's activity. We hypothesise that PPNDS, as a charged molecule (like many sugars) might interfere with virus entry. This

could explain why free PPNDS is active. Contrary, PPNDS in liposomes cannot interfere with virus entry since it is not release in the medium.

The antiviral assays described above do not allow to assess whether the PPNDS target enzyme is indeed the polymerase domain. In order to determine which part of the replication cycle is blocked, a kinetic study (Time of Drug Addiction Study) should be performed.

7.2 Antivirals cell-based assays

In the context of my discovery searches for new antivirals, I tested several compounds and drugs from various libraries on different cell-lines (RAW 264.7, Vero118 and BHK) infected respectively by mNV, hCoV NL63 (human coronavirus) and YFV.

For each type of virus, I tested the compounds reported in Table 6:

Virus	Cell-line	Compounds
mNV CW1	RAW 264.7	ZC-Tri-G-Mc; ZC-Tri-G-2OH; ZC-Flex-G-Mc; ZC-Flex-G-2OH; HP0083; 2'-c-methylcytidine (2CMC).
mNV CW3	RAW 264.7	lopinavir; pyrimethamine; nifenazone; 2'-c-methylcytidine (2CMC).
YFV	BHK	ZC-Tri-G-Mc; ZC-Tri-G-2OH; ZC-Flex-G-Mc; ZC-Flex-G-2OH; HP0083; lopinavir; pyrimethamine; nifenazone; DZL-0165; DZL-0983; DZL-0988; DZL-0998; ribavirin; 2'-c-methylcytidine (2CMC).
hCoV NL63	Vero118	ZC-Tri-G-Mc; ZC-Tri-G-2OH; ZC-Flex-G-Mc; ZC-Flex-G-2OH; HP0083; lopinavir; pyrimethamine; nifenazone; ribavirin; 2'-c-methylcytidine (2CMC).

Table 6. The compounds tested on each cell lines infected by different viruses

ZCs- and HP0083 belong to a NIs library synthesized by a chemistry group from University of Maryland (Baltimore, MD, USA), while DZLs- are *in vitro* protease inhibitors, synthesized by a chemistry group from University of Lubeck (Lubeck, Germany).

Lopinavir is an antiretroviral drug belonging the protease inhibitor class. It is used against HIV infections as a fixed-dose combination with a different protease inhibitor, ritonavir. Lopinavir is highly bound by plasma proteins (98–99%).

Pyrimethamine is a medication used for protozoan infections. It is commonly used as an antimalarial drug (for both treatment and prevention of malaria), and is also used (combined with the sulfonamide antibiotic sulfadiazine) in the treatment of *Toxoplasma gondii* infections in immunocompromised patients, such as HIV-positive individuals. Pyrimethamine can increase ß-hexosaminidase activity, thus potentially slowing down the progression of Late-Onset Tay–Sachs disease.

Ribavirin is a guanosine (ribonucleic) analog used to stop viral RNA synthesis and viral mRNA capping, thus, it is a NI. It is a pro-drug, which when metabolized resembles purine RNA nucleotides. In this form it interferes with RNA metabolism required for viral replication. How it exactly affects viral replication is unknown; many mechanisms have been proposed, but none has been proven to date. Ribavirin is used primarily to treat hepatitis C and viral hemorrhagic fevers (which is an orphan indication in most countries). Ribavirin is the only known treatment for a variety of viral hemorrhagic fevers, including Lassa fever, Crimean-Congo hemorrhagic fever, Venezuelan hemorrhagic fever and Hantavirus infection, although data regarding these infections are scarce and the drug might be effective only in the early stages of the disease.

Nifenazone is a drug that has anti-inflammatory, analgesic, antipyretic, and platelet-inhibitory actions. Some experiment showed an anti-helicase activity against DENV.

2CMC is the first NI of the hepatitis C virus (HCV) NS5B polymerase reported. 2'-C-Methylcytidine, as its valyl ester pro-drug (NM283), was effective in reducing the viral load in patients infected with HCV. 2'-C-methylcytidine is a potent and selective inhibitor of the replication of foot-and-mouth disease virus. It is also known to inhibit NV RdRp and to have an effect against YFV [92]. In my experiments I have used 2CMC as positive control.

All the information of the above compounds was available through the http://pubchem.ncbi.nlm.nih.gov web site.

All the compounds, with the exception of ZC- and DZ- libraries that I cannot display for copyright reasons, are shown in Figure 29.

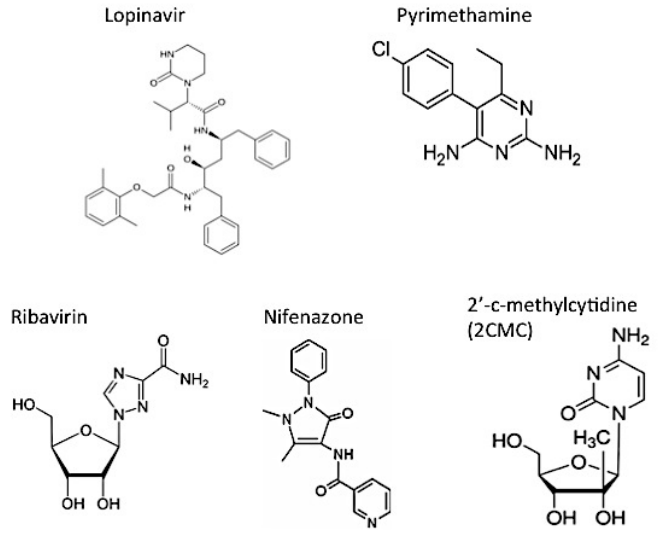

Fig 29. Chemical structures of compounds tested on mNV, hCoV and YFV.

To test the compounds I seeded the cells which adhered to the surface of the plate and the day after I added the viruses and different concentrations of the compounds. The analysis of the antiviral and cytotoxicity results has been done with MTS assay (spectrophotometric assay) for the mNV/RAW 264.7 cells, while for the other viruses/cell lines the assays were analyzed with the Methylene Blue test (see *Cell-based assay Materials and Methods* paragraph).

2CMC, HP0083 and Lopinavir showed the best inhibition capability *versus* hCoV NL63 with EC_{50} slightly over 10µM (Figure 30).

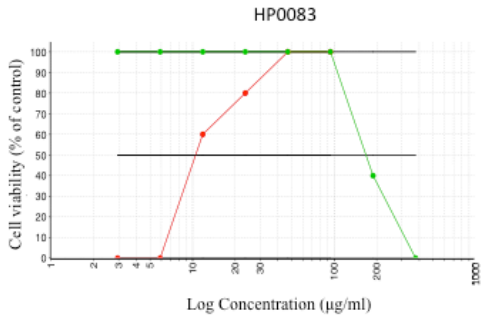

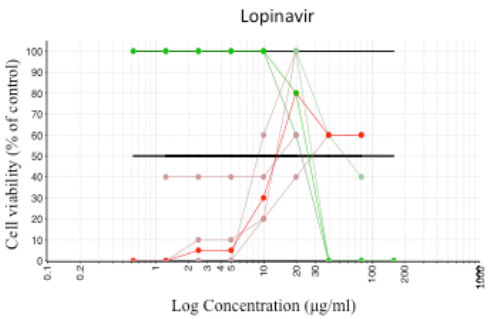

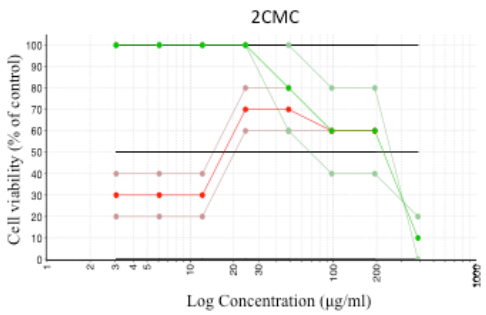

Compounds	EC_{50} (µM)	CC_{50} (µM)
2CMC	17.2	223
HP0083	10.5	168
Lopinavir	13.1	23.8

Fig 30. EC_{50} and CC_{50} values of 2CMC, HP0083 and Lopinavir on hCoV NS63 in Vero118 cells. Green lines refer to cytotoxicity and red lines to antiviral activity of the compounds, where 100% means all cells survive. The thin lines are single measures, while the bold lines are the averages. The concentration is shown on a logarithmic scale.

Lopinavir showed a low CC_{50} value (high cytotoxicity), therefore I focused on the compounds 2CMC and HP0083, quantifying the amount of viral RNA present in the cells, previously infected and treated with the two compounds, through RT-qPCR (Figure 31) (see *Cell-based assay Materials and Methods* paragraph). The cytotoxicity assay has been analyzed with the MTS assay.

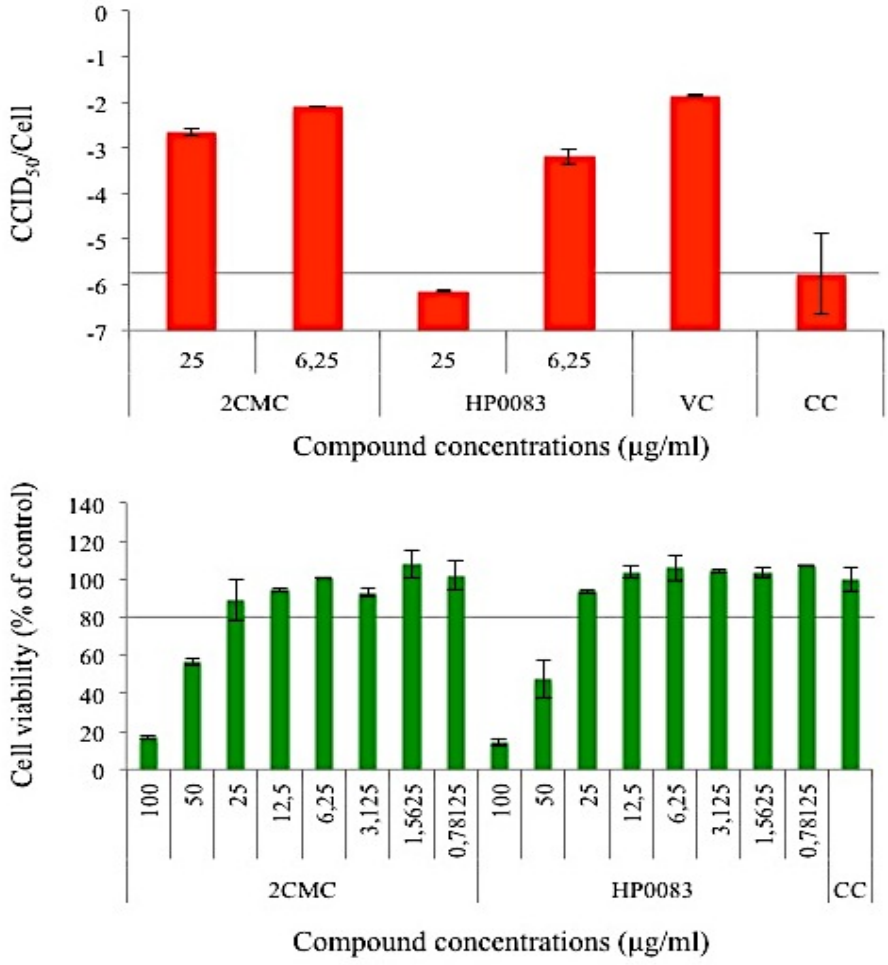

Fig 31. RT-qPCR counting the amount of viral RNA in Vero118 treated with 2CMC and HP0083 and infected by hCoV. The antiviral activity is expressed as the amount of RNA equivalent to the amount of RNA in a virus stock with the indicated titer (expressed in

CCID50/Cell; Cell Culture Infectious Dose 50%/Cell) while the cytotoxicity in % of cells viability.

The results confirm that HP0083 is a good inhibitory compound since it is not toxic up to 25µg/ml (a compound is considered not toxic if cell viability is over 80%). At 25µg/ml it inhibits the hCoV NL63; in fact, HP0083 treated cells and CC (cell control) show the same Cell Culture Infectious Doses ($CCID_{50}$). Future experiments have been planned to study the inhibition target and the mechanism of action of the selected compound.

8. Materials and Methods

8.1 Cell-based assay Materials and Methods

8.1.1 Cells and viruses

mNV (virus strain MNV-1.CW1/CW3) was propagated in RAW 264.7 cells (Figure 32a) grown in DMEM (Life Technologies) supplemented with 10% or 2% FBS, 2 mM L-glutamine, 20 mM HEPES, 0.075 g/L sodium bicarbonate, 1 mM sodium pyruvate, 100 U penicillin/mL and 100 µg/mL streptomycin at 37 °C in a humidified atmosphere of 5% CO_2.

YFV was propagated in Vero118 cells (Figure 32b) grown in IMDM (Life Technologies) supplemented with 10% or 1% FBS, 100 U penicillin/mL and 100 µg/mL streptomycin at 37 °C in a humidified atmosphere of 5% CO_2.

hCoV NL63 was propagated in BHK cells (Figure 32c) grown in DMEM (Life Technologies) supplemented with 10% or 2% FBS, 100 U penicillin/mL and 100 µg/mL streptomycin at 37 °C in a humidified atmosphere of 5% CO_2.

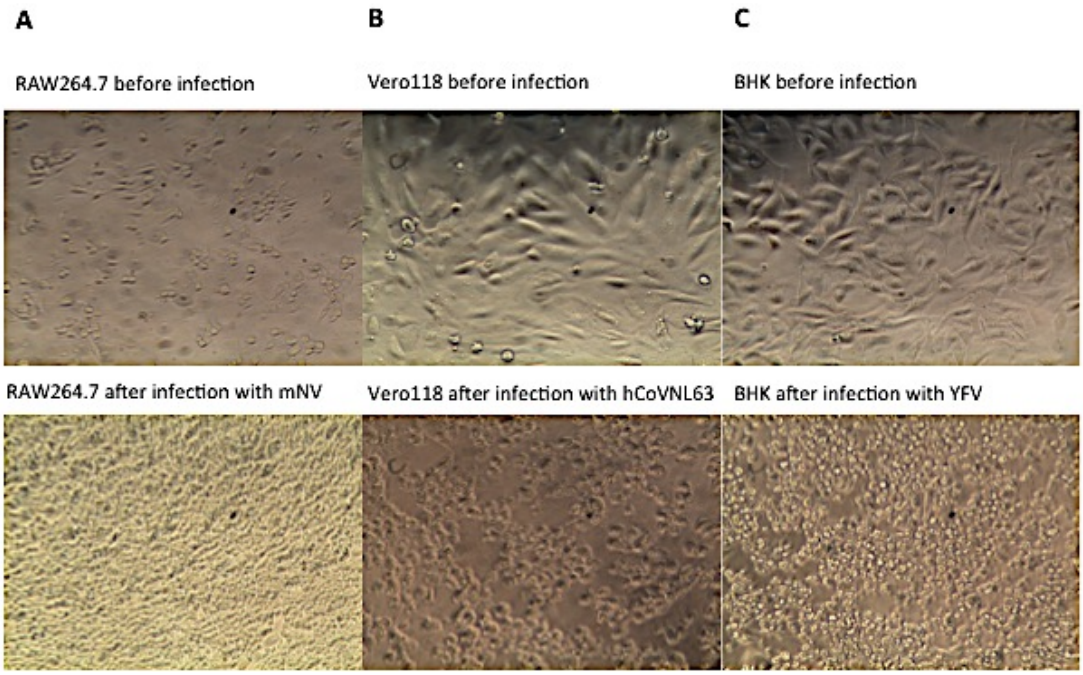

Fig 32. a) RAW264.7, b) Vero118 and c) BHK cells seeded in well before and after 3 days virus infection. Each cell-line is in a different medium.

8.1.2 Antiviral & cytotoxicity: MTS assay

The antiviral activities of different compounds were determined using an MTS [3-(4,5-dimethylthiazol-2-yl)-5-(3-carboxymethoxyphenyl)-2-(4- sulfophenyl)-2H-tetrazolium]-based CPE (Cytopathic effect; damage to host cells during virus invasion) reduction assay in the mNV/RAW 264.7 cell line. To this end, the cells were seeded (2 x 10^4 cells/well) in 96-well plates and infected with mNV at an MOI (Multiplicity of infection; number of virions that are added per cell during infection) of 0,001 in the presence (or absence) of a dilution series of compounds (0.781–100 µg/ml). Following 3/4 days of incubation, i.e. until complete CPE was observed in infected untreated cells, an MTS/Phenazine methosulphate (PMS) stock solution (2 mg/mL MTS (Promega) and 46 g/mL PMS (Sigma–Aldrich) in PBS at pH 6–6.5) was diluted 1/20 in MEM (Life Technologies). To each

well, 75 µl of MTS/PMS solution was added and the optical density (OD) was read at 498 nm 2 h later. The % CPE reduction was calculated as [(ODtreated)mNV - OD_{VC}]/[OD_{CC} - OD_{VC}]*100, where OD_{CC} represents the OD of the uninfected untreated cells, whereas OD_{VC} and (ODtreated)mNV represent the OD of infected untreated cells and virus-infected cells treated with a compound concentration, respectively. The EC_{50} is defined as the compound concentration that protected 50% of cells from virus-induced CPE.

Adverse effects of the molecule on the host cell (cytotoxicity) were also assessed by means of the MTS-method, by exposing uninfected cells seeded 5 x 10^3 cells/well to the same concentrations of compounds for 3 days. The % cell viability was calculated as (ODtreated/OD_{CC})*100, where OD_{CC} is the OD of uninfected untreated cells and ODtreated are uninfected cells treated with compound. The CC_{50} was defined as the compound concentration that reduces the number of viable cells by 50%. This MTS assay was also performed on Vero118 cell line.

8.1.3 Antiviral & cytotoxicity: Methylene Blue assay

The cells were seeded (2 x 10^4 cells/well) in 96-well plates and infected with viruses at an MOI of 0,02 for YFV or 0,00001 for hCoV NL63 in presence (or absence) of a dilution series of compounds (0.781-100 µg/ml). Following 3/4 days of incubation at 37°C (35°C for hCoV NL63) the culture medium in each well was removed. 200 µL Ethanol 70% is added to all wells and after one night ethanol is removed. The ethanol addiction permit cells fixation. 50 µL of filtered 1 % (w/v) Methylene Blue in PBS was added to each well. After 1 h, excess dye was removed. The cell layer, still stained with methylene blue, can be examined microscopically. I gave a

score to each well depending on the amount of methylene blue fixed (5= white, 0= blue) and analyzed the data with an home made program like Microsoft Excels.

The cytotoxicity test was carried out in the same way without infected cells.

8.1.4 RNA isolation and quantitative RT-PCR

The cells in the antivirals plates were seeded 2 x 10^4 cells/well in 96-well plates and infected with hCoV NL63 at an MOI of 0.1. After 2h of incubation at 35°C, I removed the supernatant, washed the plates with 100µL of DMEM 2% FBS and added several concentration of compounds (0.781-100µg/ml). Following 4 days of incubation at 35°C, the intracellular RNA was extracted from cells using the lysis buffer of Ambion® Cells-to-cDNA™ II Kit (Life Technologies): I removed the supernatant, washed the wells with PBS and added 50µl of lysis buffer. After 5 minutes at room temperature shaking the plate, I transferred the wells content in a new plate, holding it at 75°C for 15 minutes. I analyzed virus control (VC), cell control (CC) and two concentration conditions per compound. The qRT-PCR was performed in 10µL reaction mixture containing 8µL of SYBR® Green reaction mix (BIO RAD) (containing iTaq DNA polymerase, buffers, and ROX normalization dyes; iScript™ reverse transcriptase; nuclease-free water; primers from nucleocapside protein gene forward 5'-GTGGAAAACCTTTGGCATCAA-3' and reverse 3'-ACCTCGTTGGAAGCGTGTTC-5') and 2µL of template hCoV RNA. The master mix cycling conditions were: reverse transcription at 50 °C for 10 min, polymerase activation and DNA denaturation at 95 °C for 1 min, followed by 40 cycles of denaturation at 95 °C for 15s, annealing and

extension at 60 °C for 1 min (Roche lightCycler96w). I analysed the Ct (threshold cycle) values with Microsoft office excel. Ct is a relative measure of the concentration of viral RNA in the PCR reaction.

8.2 Flavivirus RdRp Materials and Methods

8.2.1 Expression and purification of the WNV and DENV RdRp

The WNV RdRp was expressed in Escherichia coli strain C41pLys, transformed with plasmid construct pDEST14 in which was cloned ns5 gene encoding a N-terminal His6 tag (aa 273-905). Cells were grown at 37°C to an OD_{600} 0.6, induced with 0.5mM isopropyl β-D-thiogalactopyranoside (IPTG) and further incubated for 16-18 h at 17°C. Cells were harvested by centrifugation. The cell pellet was resuspended in TrisHCl 50mM pH 8.00, 300mM NaCl, 10mM imidazole, 0.8mM DTT, DNase I (2 μg/ml), protease inhibitors tablet (Roche), and cells were lysed using a cells disruptor (Basic Z Bench top 0.75KW; Constant System). Any insoluble material was removed by centrifugation at 4°C and 18000 rpm for 60 min. The supernatant was filtered through a 0.44μm filter. The sample was applied to a 1-ml bed volume HiTrap nickel immobilized metal ion affinity chromatography column (G.E. Ealthcare) connected to a FPLC system (G.E. Healthcare). The protein was eluted in a stepwise manner with 50 mM Tris buffer, pH 8.0, containing 300 mM NaCl and 260 mM imidazole, 0.8mM DTT. Protein-containing fractions were then applied onto a preparative Superdex 200 gel filtration column pre-equilibrated in 50 mM Tris buffer, pH 9.0, with 300 mM NaCl, 5% glycerol and 1mM DTT. The polypeptide composition of the different fraction was monitored by Coomassie-stained sodium dodecyl sulfate-polyacrylamide gel electrophoresis analysis.

Protein was concentrated to 12 mg/ml using a 10-kDa molecular mass cut-off centrifugal concentrator (Millipore), divided into aliquots and stored at -80°C.

DENV-3 RdRp (aa272-900) was cloned into pET15b and expressed in BL21pLys. The cell pellet, diluted in a buffer (buffer A) containing 20 mM Na HEPES at pH 7.0, 300 mM NaCl, 5 mM imidazole and EDTA-free complete protease inhibitors (Roche), was lysed using a cells disruptor (Basic Z Bench top 0.75KW; Constant System). The lysate was clarified by centrifugation at 18000 rpm for 1 h at 4°C. The supernatant was purified by 1-ml bed volume HiTrap nickel immobilized metal ion affinity chromatography column (G.E. Ealthcare) connected to a FPLC system (G.E. Ealthcare) by wasching unbound protein with buffer A supplemeted with 40 mM imidazole. The RdRp was eluted in a stepwise manner with 22.5 mM imidazole. For removing the N-terminal His tag, 500 U of thrombin (Sigma) was added to the pooled fractions containing the RdRp; the mixture was dialyzed overnight against buffer A supplemented with 5 mM TCEP. The RdRp was further purified by size exclusion chromatography (Superdex 200) using the same buffer. The polypeptide composition of the different fraction was monitored by Coomassie-stained sodium dodecyl sulfate-polyacrylamide gel electrophoresis analysis. Protein was concentrated to 9 mg/ml using a 10kDa molecular mass cut-off centrifugal concentrator (Millipore), divided into aliquots and stored at -80°C.

8.2.2 Flavivirus RdRps inhibition assay.

RdRp activity was assessed *in vitro* as described [78]. In brief, we followed the synthesis of a double-stranded RNA from a single-stranded RNA poly(rC) template (Sigma-Aldrich P4903) annealed with a rG_{12} primer

(62.5 nM final concentration) and 100 μM GTP, in a reaction mixture containing 1) for DENV RdRp: 20 mM Tris/HCl (pH 7.5), 1 mM DTT, 25 mM NaCl, 5 mM $MgCl_2$, 0,3 mM $MnCl_2$, 2 U RiboLock Ribonuclease inhibitor (Life technologies), PicoGreen Quantitation Reagent (Life technologies) (total volume of 200μl); 2) for WNV RdRp: 50mM Hepes (pH 8.0), 10mM KCl, 5mM $MgCl_2$, 1mM DTT, 0,5 mM $MnCl_2$, 2 U RiboLock Ribonuclease inhibitor (Life technologies), PicoGreen Quantitation Reagent (Life technologies) (total volume of 200μl). Before starting the reaction, 1μl of the protein (final protein concentration of 620 nM DENV RdRp and 750 nM WNV RdRp) was added to the mixture together with increasing concentrations (from 0 to 30μM) of the inhibitor compounds, previously dissolved in 100% DMSO. The reactions were followed for 10 min at 30°C measuring PicoGreen fluorescence (Varian, Cary Eclipse Fluorescence Spectrophotometer). The protein activity was evaluated subtracting the linear slope of the fluorescence from that of the assay mixture in the absence of the enzyme. The results of three independent experiments were averaged. Measurements of activity *vs.* inhibitor concentration were used to estimate the IC_{50} of each inhibitor using the program GraFit5 (Erithacus software)

8.2.3 Biophysical characterization of the RdRps/HeE1-2Tyr interaction

The fluorescent dye Sypro Orange (Sigma) was used to monitor protein unfolding. The unfolding process exposes hydrophobic regions of the protein under investigation, resulting in a fluorescence increase of the dye. Thermal shift assays of RdRps in the absence/presence of the inhibitor were run in a MiniOpticon Real Time PCR Detection System (Bio-Rad). Solutions of 6.4μl and 3.13μl of respectively Dengue and West Nile RdRp

domains (final protein concentration Dengue RdRp 26.7μM, West Nile RdRp 27.39μM) were mixed with 3.5μl of Sypro Orange diluted 60×, 7.1μl of its buffer and 1μl of HeE1-2Tyr (final concentration 8μM). DMSO was added in place of the inhibitor for the control samples. The sample plates were heated from 20 to 99°C with a heating rate of 0.2°C/min. Fluorescence intensities were measured within excitation/emission ranges of 470-505/540-700nm.

8.2.4 Crystallization of the WNV RdRp and soaking with HeE1-2SO2/HeE1-2Tyr.

Microbatch crystallization experiments on WNV RdRp were assembled using an Oryx-8 crystallization robot (Douglas Instruments, East Garston, UK). In details 0.5 μl drops of 1:1 mixture of protein (12 mg/ml initial concentration) and reservoir solution were placed on a 96 well plate (Hampton Research), and covered with a mixture of 50% Paraffin oil and 50% Silicon oil. Prismatic crystals were obtained after 2 weeks at 4°C, in 300mM $MgCl_2$, 200mM NaCl, 2% Polyethilenglycol 6000, 5% Polyethilenglycol 1000, 100 mM TrisHCl pH 7.0. Crystals were soaked in a cryoprotectant solution (300mM $MgCl_2$, 400mM NaCl, 6% Polyethilenglycol 6000, 5% Polyethilenglycol 1000, 100mM TrisHCl pH 7.0 and 25% glycerol) with 5mM of HeE1-2SO2 or 15mM of HeE1-2Tyr for 36 hours, then flash-cooled in liquid nitrogen. Crystals diffracted to a maximum resolution of 2.7 Å/4.2 Å respectively, using synchrotron radiation on beam-line ID29-1 at the European Synchrotron Radiation Facility (ESRF-Grenoble, France). X-ray diffraction data were processed using MOSFLM [93], and intensities were merged using SCALA [94].

8.2.5 Structures determination and refinement.

Both WNV RdRp/HeE1-2SO2 and WNV RdRp/ HeE1-2Tyr crystals belong to the space group I222, with unit cell parameters a= 74.57 Å, b= 104.3 Å, c= 190.87 Å, with 1 molecule in the asymmetric unit. The 3D structures were solved by Molecular Replacement (MOLREP program) [95] using a search model based on the WNV RdRp structure (PDB: 2HFZ [19]). The molecule in the crystal asymmetric unit was subjected to rigid-body refinement, and subsequently refined using REFMAC5 [96]. A random set comprising 5% of the data was omitted from refinement for R-free calculation. Manual rebuilding and additional refinement (with BUSTER [97], REFMAC5 and COOT [98]) were subsequently performed, as needed.